# Excitation-Secretion Coupling in Health and Disease

By

Mazdak Bradberry

A dissertation submitted in partial fulfillment of
the requirements for the degree of

Doctor of Philosophy

(Cell and Molecular Biology)

at the

UNIVERSITY OF WISCONSIN-MADISON

2021

Date of final oral examination: 4/1/2021

The dissertation is approved by the following members of the Final Oral Committee:
Edwin R. Chapman, Professor, Neuroscience
Meyer B. Jackson, Professor, Neuroscience
Robert A. Pearce, Professor, Anesthesiology
Raunak Sinha, Assistant Professor, Neuroscience

**Abstract**

This thesis focuses on the biology of synaptic vesicles (SVs) and their $Ca^{2+}$-dependent fusion with the plasma membrane, which underlies rapid synaptic transmission. The primary $Ca^{2+}$ sensor for synaptic vesicle (SV) fusion is a protein called synaptotagmin-1 (syt1), which is anchored in the SV membrane and contains two folded regions, or domains, that concurrently bind $Ca^{2+}$ and membranes to trigger synaptic vesicle fusion. Chapter 2 comprises a biochemical comparison of syt1 and another $Ca^{2+}$ sensing protein for SV fusion, Doc2β. Chapter 3 comprises a combined clinical, biophysical, and physiologic study of how mutations in syt1 cause profound intellectual disability. Using mutations discovered in human patients, this study demonstrates a reduction in the $Ca^{2+}$ sensitivity of syt1 and a resulting deficit in excitation-secretion coupling to be responsible for syt1-associated neurodevelopmental disorder. This study also demonstrates the potential for an already-approved medication, 4-aminopyridine (4-AP), in the treatment of this disorder. Chapters 4 and 5 of this thesis describe new tools and their application to related topics in synaptic vesicle biology and excitation-secretion coupling. Chapter 4 describes a new approach for combined measurement of glutamate release and presynaptic $Ca^{2+}$ entry, along with its application to study the synaptic vesicle protein SV2A. The results in Chapter 4 demonstrate that SV2A acts downstream of presynaptic $Ca^{2+}$ entry to support synaptic exocytosis. In Chapter 5, an improved method is described for the rapid isolation of synaptic vesicles from brain tissue. This method, 1D4-IP, uses readily-available antibodies and other reagents and allows for the isolation of synaptic vesicles 10-fold purer than with classical techniques in $1/10^{th}$ the amount of time. This method was applied to the long-standing question of whether about synaptic vesicles contain adenine nucleotides such as ATP.

**Acknowledgments**

This work, and the great joy I've had carrying it out, would have been impossible without the concentrated efforts of my family, teachers, and colleagues.

My parents, Dr. Charles Bradberry and Dr. Bita Moghaddam, have been loving and supportive throughout my life. Both academic neuroscientists, they raised me in a home where curiosity was nurtured, and they made significant material sacrifices for my education. In particular, I am grateful to my father for teaching me to build useful objects with my hands, and to my mother for teaching me to work hard while always trying to think outside the box. My younger sister, Anahita Bradberry, is a talented artist whose aesthetic sense has guided me every time I plot a dataset or assemble a figure.

More than anyone else, my teachers instilled in me a deep appreciation for the invisible beauty of the microscopic world. In 6$^{th}$ grade, at the Foote School in New Haven, Conn., Lynne Valentine introduced me to the inner workings of the eukaryotic cell. In 9$^{th}$ grade, at Fox Chapel Area High School, Greg Schubert introduced me to the central dogma and the beautifully interconnected chemical nature of biological processes. I also owe my formal introduction to neuroscience to Mr. Schubert, who invited me to participate in the local Brain Bee event hosted by the Society for Neuroscience. The required reading for this event, a packet called Brain Facts, opened my eyes to the depth of neurobiology and was foundational to my development as a neuroscientist. Later, as a chemistry major at Northwestern, I had the privilege of learning bio-organic chemistry from Dr. Richard Silverman, structural biology from Dr. Vinzenz Unger, and fluorescence spectroscopy and analytical chemistry from Dr. Fred Northrup – which helped to solidify my biochemical intuition and develop a love for both fluorescence and analytical methods.

I am deeply indebted to my scientific mentors for their efforts and their willingness to take me on as a student. Dr. David Goldman and Dr. Kornel Schuebel, my mentors during my first laboratory experience at the NIH as a summer intern in 2010, taught me to think critically as a scientist and strongly encouraged me to continue my scientific pursuits. (Family matters here, too – Dr. Goldman is a longtime colleague and friend of my parents, and I applied to work in his lab only because my mother suggested it.) Dr. Peter Penzes, in whose lab I worked as a college sophomore, included me in the project-planning process and helped build my confidence as an independent scientist. Dr. Tom O'Halloran and his chemistry Ph.D. students Patrick Hankins and Elden Swindell furthered this trend, and I am particularly grateful for Patrick and Elden's patient teaching. I first learned to make liposomes from them – a skill that often came into use during my Ph.D. work.

At UW-Madison, I have been grateful for the mentorship and support of many individuals. Students in the MD/PhD program and my medical school classmates have been fantastic friends and co-conspirators. The members of my thesis committee have been generous with their time; I am particularly grateful to Dr. Meyer Jackson, Dr. Bob Pearce, and Dr. Baron Chanda for their technical help with electrophysiology and optical measurements. Dr. Anna Huttenlocher, who also served on my committee, has been a strong mentor and physician-scientist role model. Dr. Martha Vestling, in the Chemistry Department mass spectrometry lab, has been a great colleague and resource in my development as an analytical chemist.

I must also acknowledge the efforts of the many individuals who have worked hard to make science easier for the community at large. This includes those who generated and maintain open-source software such as Micro-Manager, as well as the many unnamed posters on forums and other websites on whose expertise I have relied throughout my Ph.D.

My colleagues in the Chapman lab have directly supported my work in ways too numerous to count. In particular, Chantelle Evans, who mentored me during my rotation in the summer of 2014, helped provide me with a foundation for the work done in Chapter 1 of this thesis. Dr. Huan Bao was an invaluable resource as I learned protein purification and biochemistry. Dr. Nick Courtney helped me learn electrophysiology and statistical analysis, and I am indebted to Nick for teaching me how to put together a scientific paper. I am deeply grateful to have as a colleague Dr. Jason Vevea, who has been a stellar teacher of microscopy and cell and molecular biology, a joy to work with, and a great friend.

In addition to Huan Bao and Xiaochu Lou, who co-authored the material in Chapter 2 of this thesis, I am indebted to my co-authors of the material in chapter 3: Dr. Bryan Sutton and his graduate student Matt Dominguez, who carried out the crystallography work; Dr. Nick Courtney, who carried out the electrophysiology shown in Fig. 2; Sydney Lofquist, who carried out the experiments shown in Fig. S5; and Dr. Andrew Knox, who helped with evaluating and writing up the cases of syt1-associated neurodevelopmental disorder described in that manuscript.

This brings me to Dr. Ed Chapman, my Ph.D. advisor and the one most directly responsible for supporting this work. Thanks to Ed's efforts, the Chapman Lab is an extraordinarily well-resourced environment, and the ready availability of instruments and reagents have been essential in my development as a scientist. Ed is continually engaged with his trainees' projects, and his interest helps ensure a healthy, vibrant intellectual environment. His guidance during the early phases of the Ph.D., and his willingness to support my independent studies in the later phases of the Ph.D., have been critical to my success. The fun that we have in the lab has also supported a great friendship between us. At the end of my Ph.D. studies, I find myself filled with gratitude and excitement, and I could not have imagined a better scientific and personal match for a thesis advisor.

## Table of Contents

**Abbreviation List**

ATP, adenosine-5'-triphosphate
$[Ca^{2+}]_i$, cytoplasmic calcium
$[Ca^{2+}]_e$. extracellular calcium
Doc2, double C2-domain containing protein
HPLC, high-performance liquid chromatography
NBD, N-(7-nitrobenz-2-oxa-1,3-diazol-4-yl)ethylenediamine
PC, phosphatidylcholine
PE, phosphatidylethanolamine
$PIP_2$, phosphatidylinositol(4,5)-bisphosphate
PS, phosphatidylserine
PPR, paired-pulse ratio
SNARE, soluble n-ethylmaleimide sensitive factor attachment protein receptor
SV2, synaptic vesicle glycoprotein 2
SV, synaptic vesicle
syt1, synaptotagmin

## Chapter 1: Background

Animals, particularly higher-order species such as mammals, employ a complex set of systems to sense, move, grow, and procreate in their environments. Coordination among muscular appendages, digestive organs, and sensory organs relies upon systems for rapid communication of biochemical information. Moreover, decoding of the environment and the expression of behavior requires some internal representation of external stimuli. For optimal function, the systems underlying information representation and transfer should update as frequently as possible, and the underlying biological processes should therefore occur as rapidly as possible.

In most animals, systems of nerve cells, or *neurons*, carry out organismal coordination and internal representation. These systems may be tenable in their entirety, as with the well-catalogued nervous system of the nematode *C. elegans*, or may be formidably complex, as with the brain of a primate. In all cases, neurons employ systems for rapid communication to downstream cells, whether those cells are also neurons or part of some other specialized tissue. As the rate-limiting cellular elements of animal behavior, neuronal signaling systems have evolved under pressure to get faster. This thesis focuses on two categories of fast neuronal signaling: *within* the neuron, and *from* the neuron *to* other cells.

Within the neuron, electrical processes allow for the maintenance of a voltage across the cell membrane. This may be envisioned as a battery with its positive and negative contacts on opposite sides of the membrane. In neurons, proteins in the cell membrane allow for short "spikes" of voltage across the cell membrane, termed *action potentials*, that may be envisioned as a brief reversal of the battery's orientation. The properties of the cell membrane, along with the rapid responses of the proteins controlling transmembrane voltage, permit action potentials to travel very quickly along the length of the neuron. In general, this process is termed *excitation*, and the membrane-embedded proteins that control transmembrane voltage are termed *ion channels*. The ion channels enabling the action potential are permeable primarily to sodium ($Na^+$) or potassium ($K^+$), but not both. These channels are *voltage-gated*, i.e., respond to changes in the transmembrane voltage. Both $Na^+$ and $K^+$ channels open in response to a

voltage spike in their membrane, but the two channels serve opposite purposes. Open $Na^+$ channels *depolarize* the membrane (i.e., flip the battery) to initiate or propagate the spike, while open $K^+$ channels *repolarize* the membrane (i.e., return the battery to its original orientation) to end the spike. To this end, $K^+$ channels open slightly more slowly than $Na^+$ channels, such that the spike can rise before it falls. A key property of the membrane enabling this process is its impermeability to ions in the absence of ion channels, which permits the process to be controlled largely by the properties of the channels themselves. In most mammalian neurons, the entire spike occurs very rapidly, rising and falling within a millisecond or a fraction thereof.

Once the action potential reaches the nerve terminal, a substantially different process occurs to transmit information to the receiving cell. At most nerve terminals, such as those between neurons in the brain or between neurons and muscles at the neuromuscular junction, the neuron closely abuts the receiving cell in a configuration called a *synapse*. At the synapse, the membrane of the presynaptic cell lies only a few nanometers away from the membrane of the postsynaptic cell, in which are embedded proteins called *receptors* that are poised to detect the chemical signals released from the presynaptic cell. These chemical signals comprise *neurotransmitters*, and signaling from presynaptic to postsynaptic cell is termed *synaptic transmission*.

To afford tight temporal control of synaptic transmission, neurons store neurotransmitter in membrane-enclosed packets within the nerve terminal. These packets, called *synaptic vesicles* (SVs), have membranes containing *transporters*, or pumps, that fill the vesicles with neurotransmitter molecules. Because these neurotransmitter molecules are also ions, they are largely unable to move across membranes on their own, and they are stored in large quantities in the vesicles. When the action potential arrives at the nerve terminal, the key step in neurotransmission occurs via *exocytosis*: the fusion of the synaptic vesicle membrane with the outer membrane of the nerve terminal, which creates a pore through which neurotransmitter can escape from the vesicle into the synaptic cleft to activate postsynaptic receptors. This event, which is a form of secretion, occurs very rapidly, and the process that links action potential to neurotransmitter release is termed *excitation-secretion coupling*.

The most important molecule in excitation-secretion coupling is $Ca^{2+}$. In general, cells use $Ca^{2+}$ as a switch by tightly controlling how much is available in various parts of the cell. While $Ca^{2+}$ is plentiful in the extracellular space and within organelles, cells contain numerous transporters that remove $Ca^{2+}$ from the main intracellular space, also known as the *cytoplasm*. The concentration of $Ca^{2+}$ ($[Ca^{2+}]$) within organelles reaches around 100-500 μM, and in most extracellular fluid $[Ca^{2+}]$ is 1-2 mM, but in cytoplasm $[Ca^{2+}]$ is kept to about 10-100 nM – over 1,000 times lower than in the organelles, and over 10,000 times lower than in the extracellular fluid. Like neurotransmitters, $Na^{+}$, and $K^{+}$, $Ca^{2+}$ is an ion, and so it is effectively regulated by transporters and channels embedded in the membrane. The presynaptic membrane contains voltage-gated $Ca^{2+}$ channels that, when activated by the arriving action potential, flood the cytoplasm of the nerve terminal with $Ca^{2+}$. At the same time, transporters act to remove $Ca^{2+}$ from the cytoplasm, so the cytoplasmic $Ca^{2+}$ concentration ($[Ca^{2+}]_i$) rapidly returns to resting levels. While $[Ca^{2+}]_i$ peaks rapidly, within 1-2 ms, the decay of this signal is slower – taking tens of ms or more. Importantly, at the nanometer scale within the nerve terminal, $[Ca^{2+}]$ varies greatly over space and time, with the highest values found closest to the open $Ca^{2+}$ channels themselves. After the channels have closed, $[Ca^{2+}]$ rapidly reaches an equilibrium such that it is uniform throughout the nerve terminal.

This thesis focuses, in part, on the proteins upon which $Ca^{2+}$ acts in order to trigger membrane fusion. The primary $Ca^{2+}$ sensor for SV fusion is a protein called synaptotagmin-1 (syt1), which is anchored in the synaptic vesicle membrane and contains two folded regions, or *domains*, that concurrently bind $Ca^{2+}$ and membranes. Within fractions of a millisecond, $Ca^{2+}$ ions bind syt1 and membranes to trigger SV fusion and neurotransmitter release. Other, similar sensors, including a family of proteins called Doc2, are related to syt1 but act more slowly and are specialized for $Ca^{2+}$ concentrations closer to the cell's resting condition. Chapter 2 comprises a biochemical comparison of syt1 and a common Doc2 protein, Doc2β. In this chapter, the effect of membrane composition on $Ca^{2+}$-dependent and $Ca^{2+}$-independent membrane binding by these two proteins is established. Surprisingly, our results indicate that these proteins can not only bind to, but also partially insert into, membranes in the absence of $Ca^{2+}$, a finding that raises the possibility of $Ca^{2+}$-independent exocytosis.

Chapter 3 comprises a combined clinical, biophysical, and physiologic study of how mutations in syt1 cause profound intellectual disability. Using mutations discovered in human patients, this study demonstrates a reduction in the $Ca^{2+}$ sensitivity of syt1 and a resulting deficit in excitation-secretion coupling to be responsible for syt1-associated neurodevelopmental disorder. This study also demonstrates the potential for an already-approved medication, 4-aminopyridine (4-AP), in the treatment of this disorder. 4-AP acts to block K+ channels, which slow action potential repolarization and thus lengthen the time that voltage-gated $Ca^{2+}$ channels are open, increasing $[Ca^{2+}]_i$ and compensating for defective syt1. As a result, at least one patient with syt1-associated neurodevelopmental disorder has received 4-AP.

Chapters 4 and 5 of this thesis describe new tools and their application to related topics in synaptic vesicle biology and excitation-secretion coupling. Chapter 4 describes a new approach for combined measurement of glutamate release and presynaptic $Ca^{2+}$ entry, along with its application to study a synaptic vesicle protein called SV2A. This protein, whose sequence suggests a function as a transporter, is a binding partner of syt1 and is required for normal brain development. Moreover, SV2A is a major drug target, as it has been unequivocally established as the binding site for the antiepileptic medications levetiracetam (Keppra) and brivaracetam (Briviact). SV2A is also under intense study as a positron emission tomography (PET) imaging agent for the measurement of synaptic density in human patients (Holmes et al., 2019). However, while biochemical studies suggest that SV2A may bind to and transport the sugar galactose (Madeo et al., 2014; Wibowo et al., 2014), its function – and its physiologic relevance – in neurons is unknown. The results in Chapter 4 demonstrate that SV2A acts downstream of presynaptic $Ca^{2+}$ entry to support synaptic exocytosis.

In Chapter 5, an improved method is described for the rapid isolation of synaptic vesicles from brain tissue. This method, 1D4-IP, uses readily-available antibodies and other reagents and allows for the isolation of synaptic vesicles 10-fold purer than with classical techniques in $1/10^{th}$ the amount of time. This method was applied to the long-standing question of whether about synaptic vesicles contain adenine nucleotides such as ATP.

Finally, Chapter 6 describes future directions for this work, which involve the application of SV isolation methods and analysis to the study of the SV2A KO phenotype. While the work in these chapters covers several topics, the biology of the synaptic vesicle and its $Ca^{2+}$-dependent membrane fusion are unifying themes throughout.

## Chapter 2: $PIP_2$ drives $Ca^{2+}$-independent membrane penetration by the tandem C2 domain proteins synaptotagmin-1 and Doc2β


### Summary

Exocytosis mediates the release of neurotransmitters and hormones from neurons and neuroendocrine cells. Tandem C2 domain proteins in the synaptotagmin (Syt) and double C2 domain (Doc2) families regulate exocytotic membrane fusion via direct interactions with $Ca^{2+}$ and phospholipid bilayers. Syt1 is a fast-acting, low-affinity $Ca^{2+}$ sensor that penetrates membranes upon binding $Ca^{2+}$ to trigger synchronous vesicle fusion. The closely related Doc2β is a slow-acting, high-affinity $Ca^{2+}$ sensor that triggers spontaneous and asynchronous vesicle fusion, but whether it also penetrates membranes is unknown. Both syt1 and Doc2β bind the dynamically regulated plasma membrane lipid phosphatidylinositol(4,5)-bisphosphate ($PIP_2$), but it is unclear whether $PIP_2$ serves only as a membrane contact or enables specialized membrane-binding modes by these $Ca^{2+}$ sensors. Furthermore, it has been shown that $PIP_2$ uncaging can trigger rapid, syt1-dependent exocytosis in the absence of $Ca^{2+}$ influx, suggesting that current models for the action of these $Ca^{2+}$ sensors are incomplete. Here, using a series of steady-state and time-resolved fluorescence measurements, we show that Doc2β, like syt1, penetrates membranes in a $Ca^{2+}$-dependent manner. Unexpectedly, we observed that $PIP_2$ can drive membrane penetration by both syt1 and Doc2β in the absence of $Ca^{2+}$, providing a plausible mechanism for $Ca^{2+}$-independent, $PIP_2$-dependent exocytosis. Quantitative measurements of penetration depth revealed that, in the presence of $Ca^{2+}$, $PIP_2$ drives Doc2β, but not syt1, substantially deeper into the membrane, defining a biophysical regulatory mechanism specific to this high-affinity $Ca^{2+}$ sensor. Our results provide evidence of a novel role for $PIP_2$ in regulating, and under some circumstances triggering, exocytosis.


### Introduction

Exocytosis, a fundamental physiologic process, relies on the fusion of cellular membranes. In many cases, membrane fusion is mediated by soluble N-ethylmaleimide sensitive factor receptor proteins (SNAREs), along with accessory proteins that integrate signals near the fusion site (Edwin R Chapman,

2008; Sudhof and Rothman, 2009). At neuronal synapses, a critical signal for exocytosis is $Ca^{2+}$ (B Katz and Miledi, 1967), which acts upon tandem C2 domain proteins in the synaptotagmin (syt) (Bhalla et al., 2008; Brose et al., 1992a; Geppert et al., 1994; Hui et al., 2005; Littleton et al., 1993) and Doc2 (Groffen et al., 2010; Orita et al., 1995) families to trigger SNARE-catalyzed fusion of vesicular and plasma membranes (Groffen et al., 2010; Tucker et al., 2004).

Syt1 is a primary $Ca^{2+}$ sensor for fast, synchronous neurotransmitter release (Geppert et al., 1994; Littleton et al., 1993). It is activated by relatively large increases ($\geq$ 1 μM) in cytoplasmic $Ca^{2+}$ ($[Ca]_i$) which trigger the rapid insertion of side chains from each C2-domain into lipid bilayers containing anionic phospholipids (J Bai et al., 2004; Chapman and Davis, 1998). It has been rigorously established that penetration of lipid bilayers by syt1 accelerates SNARE-catalyzed fusion *in vitro* and in cultured neurons (Bai et al., 2016a; Evans et al., 2015a; Wang et al., 2005). Doc2β, a closely-related protein that lacks a transmembrane domain but contains a munc13-interacting domain at its N-terminus (Orita et al., 1997), regulates asynchronous (Yao et al., 2011) and spontaneous (Courtney et al., 2018a; Groffen et al., 2010) neurotransmitter release from neurons, synaptic augmentation (Xue et al., 2018), vesicle priming in chromaffin cells (Houy et al., 2017; Pinheiro et al., 2013) and insulin secretion from β cells (Li et al., 2014). In comparison to syt1, however, Doc2β-membrane interactions occur with slower kinetics and a much higher sensitivity for $[Ca^{2+}]$ (20-100 nM) (Courtney et al., 2018a; Groffen et al., 2010, 2006). Thus, while both syt1 and Doc2β are $Ca^{2+}$ sensors for exocytosis, their divergent functional paradigms invite a closer comparison to establish common mechanistic principles for $Ca^{2+}$-sensitive tandem C2 domain proteins. For example, while syt1 must penetrate membranes to stimulate membrane fusion, it has not been established whether—and if so, how—Doc2β penetrates membranes.

Alongside proteins and $Ca^{2+}$, phospholipid headgroups play key biophysical roles in $Ca^{2+}$-triggered exocytosis. Of particular note is phosphatidylinositol(4,5)-bisphosphate ($PIP_2$), a dynamically-regulated (Micheva et al., 2001a) poly-anionic phospholipid important for exocytosis in chromaffin cells (Eberhard et al., 1990a), PC12 cells (Hay et al., 1995), and neurons (Di Paolo et al., 2004). $PIP_2$ is localized to the plasma membrane and interacts with key components of the vesicular release machinery including

SNARE proteins (James et al., 2008; van den Bogaart et al., 2011), calcium-activated protein for secretion (CAPS) (Grishanin et al., 2004), syt1 (J Bai et al., 2004; Tucker et al., 2003; Van den Bogaart et al., 2012), and Doc2β (Courtney et al., 2018a; Groffen et al., 2010; Michaeli et al., 2017). In the case of syt1, binding to $PIP_2$ under resting conditions "steers" the C2 domains of this protein—and thus its $Ca^{2+}$-dependent membrane-penetration activity—toward the plasma membrane to trigger release (J Bai et al., 2004). $PIP_2$ has also been shown to enhance the $Ca^{2+}$ sensitivity of lipid binding by syt1 cooperatively with phosphatidylserine (PS) (Pérez-Lara et al., 2016; Van den Bogaart et al., 2012), the major anionic phospholipid of cytoplasmic face of the plasma membrane. Similarly, Doc2β binds $PIP_2$-containing membranes in both the presence and absence of $Ca^{2+}$, and $PIP_2$ is required to localize Doc2β to the plasma membrane (Courtney et al., 2018a; Groffen et al., 2010; Michaeli et al., 2017). Because depletion of $PIP_2$ substantially reduces spontaneous neurotransmitter release in cultured neurons (Di Paolo et al., 2004), this form of neurotransmission may depend on $PIP_2$ binding by Doc2β, but this interaction has not been studied in detail.

According to current models of tandem C2-domain protein function, $Ca^{2+}$ is required for membrane penetration and thus the triggering of exocytosis. However, recent findings have challenged this model by demonstrating that rapid uncaging of $PIP_2$ can trigger syt1-dependent exocytosis without a measurable change in $[Ca^{2+}]_i$ (Walter et al., 2017). Given the apparent requirement of $Ca^{2+}$ for membrane penetration by syt1, how could a stepwise increase in available $PIP_2$ evoke exocytosis?

In the present study, we first demonstrate that, like syt1, Doc2β penetrates lipid bilayers upon binding $Ca^{2+}$. We report the unexpected finding that, in membranes containing PS, $PIP_2$ drives $Ca^{2+}$-independent membrane penetration by both syt1 and Doc2β. This interaction stimulates $Ca^{2+}$-independent fusion mediated by syt1 *in vitro*. Moreover, in the presence of $Ca^{2+}$, $PIP_2$ significantly increases the membrane penetration depth of Doc2β, but not syt1, thus providing a mechanism by which $PIP_2$ may selectively drive spontaneous release. Our results define key biophysical differences between syt1 and Doc2β and provide a potential molecular mechanism by which $PIP_2$ can directly trigger exocytosis in the absence of increases in $[Ca^{2+}]_i$.

## Results

### *Doc2β penetrates and aggregates membranes in a manner analogous to syt1*

We first sought to determine whether the tandem C2 domains of Doc2β share key biochemical properties with those of syt1 (**Figure 1A**). We thus purified the tandem C2 domains ("C2AB") of both proteins and used a series of assays to define their $Ca^{2+}$-dependent and -independent interactions with lipid bilayers. To assess whether the $Ca^{2+}$-binding loops of Doc2β C2AB penetrate membranes in a manner analogous to syt1, residues at the tips of loops 1 and 3 in each C2 domain of Doc2β (H158 and F222 in C2A, A298 and G361 in C2B) were individually mutated to cysteine and labeled with the environmentally sensitive probe N-(7-nitrobenz-2-oxa-1,3-diazol-4-yl)ethylenediamine (NBD) (**Fig. 1B**). Membrane insertion was monitored via fluorescence emission changes after adding liposomes and $Ca^{2+}$ to NBD-labeled protein. Emission spectra from NBD probes at all four $Ca^{2+}$-binding loops underwent hypsochromic shifts and substantial intensity increases when both $Ca^{2+}$ and PS-containing liposomes were present. $Ca^{2+}$ triggered these fluorescence changes only in the presence of membranes, suggesting that each probe inserts into the bilayer in response to $Ca^{2+}$ (**Fig. 1C** and **Appendix – figure S1**). To confirm a direct interaction between these probes and the acyl chains in the bilayer, we used liposomes containing a membrane-embedded nitroxide (doxyl) spin label on an acyl chain of PC; this moiety quenches fluorescence largely by direct collision with excited-state fluorophores (London and Chattopadhyay, 1987). NBD fluorescence, in each loop, was efficiently quenched by a spin label at the 12-position of the acyl chain (12-doxyl PC, 15 mol %) (**Fig. 1C)**, directly demonstrating that all four $Ca^{2+}$-binding loops of Doc2β insert into the hydrophobic region of the bilayer.

Aggregation of PS-containing liposomes is also a characteristic property of syt1 C2AB *in vitro* (Hui et al., 2011). This activity has not been described for Doc2β, a soluble protein whose function may also rely on its ability to juxtapose membranes. To assay for aggregation activity, Doc2β C2AB was mixed with liposomes and $Ca^{2+}$, and the turbidity of the mixture was monitored by absorbance at 400 nm. As with syt1 C2AB, Doc2β C2AB rapidly and reversibly aggregated liposomes that harbored PS (**Appendix**

**– fig. S2A**). Moreover, this aggregation activity was strongly enhanced when copies of Doc2β C2AB were bound to separate liposomes and thus available to interact in *trans* (**Appendix – fig. S2B,C**). This behavior, which was also observed for syt1 (Hui et al., 2011) (**Appendix – fig. S2**), suggests a common mechanism of aggregation in which C2AB molecules, bound to liposomes via their $Ca^{2+}$-binding loops, subsequently interact with other liposome-bound C2AB molecules.

***$PIP_2$ triggers $Ca^{2+}$-independent membrane penetration by Doc2β and syt1***

We next focused on the role of $PIP_2$ in driving specific modes of membrane-binding by syt1 and Doc2β. Because previous studies of membrane penetration by syt1 were performed using non-physiologic mixtures of phospholipids (Bai et al., 2016a; J Bai et al., 2004; Hui et al., 2006), we assayed the membrane penetration activity of syt1 and Doc2β in the presence of model plasma membranes that included 15 mol % PS and 1 mol % $PIP_2$, a composition that reflects the $PIP_2$ content of neuronal and neuroendocrine cell plasma membranes (James et al., 2008; Wenk et al., 2003). Indo-1 was used to verify that $[Ca^{2+}]_{free}$ remained very low, i.e., ≤10 nM, upon addition of PS:$PIP_2$ lipids **(Fig. S3)**. Surprisingly, under these conditions, we observed not only $Ca^{2+}$-independent binding but also $Ca^{2+}$-independent penetration of the bilayer by both proteins (**Fig. 2A,C**). In each case this activity, at 1 mol % $PIP_2$, was limited to the $Ca^{2+}$ binding loops of the C2B domain. Inclusion of 12-doxyl-PC in the liposomes resulted in quenching of NBD fluorescence, confirming a direct interaction of C2B, loop 3 with the interior of the membrane in the case of each protein (**Fig. 2A,C**). Syt1 and Doc2β C2AB diverged in terms of the behavior of C2B, loop 1, which failed to penetrate in the case of syt1 but engaged in shallow penetration in the case of Doc2β (**Fig. 2A,C**). PS and $PIP_2$ were both required for $Ca^{2+}$-independent penetration of membranes by both syt1 and Doc2β (**Fig. 2B,D**). Previous studies of membrane penetration by syt1 included liposomes containing either PS or $PIP_2$, but not both, thus explaining why this novel interaction was not previously observed (Bai et al., 2016a; J Bai et al., 2004; Hui et al., 2006).

These data suggest that syt1 and Doc2β contain at least partially distinct binding sites for PS and $PIP_2$ that, when occupied simultaneously, drive $Ca^{2+}$-independent insertion of C2B into the bilayer. To confirm

that these findings hold true for full-length syt1, we formulated nanodiscs containing the full-length, labeled protein (ND-syt1) (**Fig. 3A**). As in the case for C2AB, ND-syt1 underwent $Ca^{2+}$-independent penetration of membranes containing PS and $PIP_2$, but not PS alone (**Fig. 3B**) This result is of particular significance because, in chromaffin cells, optical uncaging of $PIP_2$ drives a small, syt1-dependent exocytotic burst even in the absence of measurable changes in $Ca^{2+}$ levels (Walter et al., 2017) (see Discussion).

***$PIP_2$ exhibits differential effects on Doc2β and syt1***

Our penetration experiments (**Fig. 2**) also revealed striking, lipid-dependent differences between syt1 and Doc2β in the presence of $Ca^{2+}$. In particular, Doc2β C2A loop 3 demonstrated a unique increase in fluorescence only when both PS and $PIP_2$ were present (**Fig. 2B**). In contrast, we observed no such changes in the analogous position in syt1, which displayed equivalent $Ca^{2+}$-dependent NBD fluorescent increases upon binding PS-bearing liposomes whether or not $PIP_2$ was included (**Fig. 2D**). We explored this issue further by examining the impact of PS and $PIP_2$ on the disassembly kinetics of $Ca^{2+}$ sensor-lipid complexes. In this assay, pre-assembled C2AB-$Ca^{2+}$-liposome complexes were rapidly mixed with EGTA to remove free [$Ca^{2+}$] while FRET was monitored between protein and liposomes using a stopped-flow rapid mixing instrument (**Fig. 4**). The inclusion of 1 mol % $PIP_2$ in PS-bearing liposomes had no effect on the disassembly kinetics of syt1 complexes (mean ± SEM: PS, 73.7 ± 10.0 $s^{-1}$; PS:$PIP_2$, 79.1 ± 7.8 $s^{-1}$, $p > 0.5$, Welch's *t*-test) (**Fig. 4B**). In striking contrast, $PIP_2$ slowed the disassembly of Doc2 complexes nearly ten-fold (PS, 4.90 ± 0.21 $s^{-1}$; PS:$PIP_2$, 0.49 ± 0.03 $s^{-1}$, $p = 0.0002$, Welch's *t*-test) (**Fig. 4C**). In combination with data from NBD-labeled penetration assays (**Fig. 2**), these findings further support a specific role for $PIP_2$ in stabilizing the $Ca^{2+}$-dependent activated state of Doc2β.

***Quantitative analysis of membrane penetration activity***

Our initial NBD fluorescence results (**Figs. 1, 2**) motivated a more quantitative comparison of membrane penetration by syt1 and Doc2β. We thus used the parallax method of London and colleagues

(Abrams and London, 1993; London and Chattopadhyay, 1987) to determine the insertion depth of NBD on each loop of syt1 and Doc2β, in the presence and absence of $Ca^{2+}$ and $PIP_2$. We used doxyl-PC labeled at either the 5- or 12-positions of the acyl chain, as well as on the choline headgroup (HG-doxyl, **Fig. 5A**, also known as TEMPO-PC). Quenching efficiencies in the presence of $Ca^{2+}$ are shown in **Fig. 5C,D** while quenching efficiencies in the absence of $Ca^{2+}$ are shown in **Appendix – fig. S7**. Increased quenching by deeper doxyls and decreased quenching by shallower doxyls indicate deeper insertion of the NBD probe. By comparing the quenching efficiencies of spin labels at various points on the alkyl chains, we quantitatively estimated the depth to which the NBD labels penetrate the membrane. For this analysis, we improved on previous implementations of the parallax analysis by using published molecular dynamics simulations of doxyl-PC quenchers (Kyrychenko and Ladokhin, 2013) to determine the uncertainty in the measured penetration depth for each probe (see Methods). Calculated depth parameters are shown in **Table 1** and represented visually in **Fig. 7**.

In the presence of $Ca^{2+}$, $PIP_2$ exerted strikingly different effects on membrane penetration by Doc2β versus syt1 (**Fig. 5, Fig 7**). While $PIP_2$ drove all four loops of both syt1 and Doc2β deeper into the bilayer, this effect was far more pronounced for Doc2β. In particular, loop 3 of Doc2β C2A penetrated, on average, 3.7 Å deeper into the bilayer in the presence of $PIP_2$. In contrast, $PIP_2$ increased the average penetration depth of the loops of syt1 by, at most, 1 Å. Remarkably, Doc2β C2A penetrates only shallowly into PS-bearing membranes lacking $PIP_2$, but penetrates approximately as deeply as syt1 if $PIP_2$ is present (**Fig. 5C, Fig. 7**). Syt1, by contrast, penetrates PS-bearing membranes to nearly its full extent even in the absence of $PIP_2$ (**Fig. 5D, Fig. 7**) These results provide direct evidence that $PIP_2$ substantially deepens $Ca^{2+}$-dependent membrane penetration by Doc2, but has relatively subtle effects on syt1. Our findings define a mechanistic divergence between syt1 and Doc2β and a biophysical mechanism by which Doc2β acts specifically as a $PIP_2$-dependent $Ca^{2+}$ sensor.

***Elevation of $PIP_2$ drives additional membrane penetration to stimulate membrane fusion***

Physiologic [$PIP_2$] in the plasma membrane is approximately 1 mol % but can reach >5 mol % at sites of vesicle docking and fusion (James et al., 2008; Wenk et al., 2003). Even at 1% $PIP_2$, we noted some doxyl quenching of NBD probes on the C2A domains of syt1 and Doc2β, suggesting that further increases in $PIP_2$ might drive additional membrane penetration by these sensors (**Appendix – fig. S7**). To assess how elevating [$PIP_2$] might drive alternative membrane-penetration modes by syt1 and Doc2β, we measured emission from NBD-labeled syt1 and Doc2β C2AB in the presence of liposomes containing increasing mol % $PIP_2$ (**Fig. 6A, B**). We observed significant, dose-dependent increases in NBD emission intensity for labels on C2A in both Doc2β and syt1 as $PIP_2$ was increased from 1 mol % to 5 mol %. In the case of Doc2β, elevation of [$PIP_2$] drove penetration by all four loops, with this effect approaching saturation at 5% $PIP_2$ (Fig. 5A). In the case of syt1, increasing [$PIP_2$] drove penetration by C2A, loop 3, demonstrating that elevation of [$PIP_2$] can trigger activation of both C2 domains of this protein (**Fig. 6B**). These results support a specific role for $PIP_2$ in activating both Doc2β and syt1 at physiologically relevant concentrations (illustrated in **Fig. 7**). Moreover, these findings suggest a mechanism by which syt1, under certain circumstances, may be partially activated by $PIP_2$ to trigger $Ca^{2+}$-independent vesicle fusion (Walter et al., 2017).

Because $PIP_2$-dependent, $Ca^{2+}$-independent penetration by syt1 was less extensive than that of Doc2β, we sought to determine whether this novel penetration activity can enhance vesicle fusion in the absence of $Ca^{2+}$. We thus performed *in vitro* fusion assays using v-SNARE vesicles containing syb2 and full-length syt1 with t-SNARE vesicles containing syntaxin-1A:SNAP-25B heterodimer and increasing amounts of $PIP_2$ (**Fig. 6C-F**). In both lipid and content mixing assays, elevation of [$PIP_2$] enhanced fusion of v- and t-SNARE vesicles prior to the addition of $Ca^{2+}$, consistent with the capacity of $PIP_2$ to drive $Ca^{2+}$-independent activation of syt1 (Walter et al., 2017). Increasing $PIP_2$ likewise enhanced membrane fusion after the addition of $Ca^{2+}$, consistent with published findings using *in vitro* fusion assays (Wang et al., 2011a) and $PIP_2$ uncaging in chromaffin cells (Walter et al., 2017).

**Discussion**

Taken together, our results demonstrate key similarities and unanticipated differences between syt1 and Doc2, tandem C2 domain $Ca^{2+}$ sensors specialized for distinct physiologic functions. Our results reveal that, like syt1, Doc2β aggregates and penetrates membranes containing anionic phospholipids in response to $Ca^{2+}$ (**Fig. 1, Appendix – fig. S2**). This activity, which likely results in a $Ca^{2+}$-dependent deformation of the membrane due to the space occupied by the tips of the $Ca^{2+}$-binding loops (Hui et al., 2009a; Martens et al., 2007), thus appears to be a core feature of tandem C2 domain $Ca^{2+}$ sensors. Given that Doc2β is not anchored to vesicles by a transmembrane domain and that vesicular membranes contain anionic phospholipids, it is possible that this aggregation activity may, in part, underlie the ability of this protein to promote membrane fusion.

Our findings establish a new role for $PIP_2$ in exocytosis by showing that $PIP_2$ directly stimulates penetration of the target membrane by syt1 and Doc2β. While $PIP_2$ has been understood as a key factor in defining exocytotic sites and priming vesicles for release, our work defines an additional downstream function, i.e., direct activation of $Ca^{2+}$ sensors that trigger SNARE-catalyzed membrane fusion. Critically, while $Ca^{2+}$ stimulates membrane penetration, we show that it is not strictly required for this activity when $PIP_2$ is present (**Fig. 2**, **Fig. 3, Fig. 6, Fig. 7**). To our knowledge, this is the first evidence that a C2 domain can penetrate (and thus presumably deform (Hui et al., 2009a; Martens et al., 2007)) a membrane without an elevation in $[Ca^{2+}]_i$. Thus, a rapid increase in $[PIP_2]$, e.g. via optical uncaging of caged $PIP_2$ as performed by Walter et al (2017), might trigger syt1-dependent release via two non-exclusive mechanisms: recruitment of additional $Ca^{2+}$ sensors that penetrate the plasma membrane, or by driving deeper penetration by $Ca^{2+}$ sensors that are already present at release sites (**Fig. 6, Fig.7**). Furthermore, because $[PIP_2]$ can reach > 5 mol % at release sites (James et al., 2008) and the plasma membrane contains ~10-15 mol % PS (Cotman et al., 1969), it is likely that the docked and/or primed configurations of syt1 and Doc2β involve some degree of insertion into the plasma membrane. However, while the $PIP_2$ uncaging technique of Walter et al. (2017) provides useful mechanistic insights, we note that we are not aware of studies showing such rapid upregulation of $PIP_2$ at exocytotic sites in endogenous systems.

Strikingly, the $Ca^{2+}$-independent penetration activity of Doc2β reached near-saturation at 5 mol % $PIP_2$, a dose-response that is well-tuned to the physiologic range of $PIP_2$ levels at sites of fusion. We also note that, while $Ca^{2+}$ plays key roles in physiologic exocytosis, multiple studies have demonstrated varying degrees of residual exocytosis after dramatically reducing $[Ca^{2+}]_i$ (Kochubey and Schneggenburger, 2011a; Vyleta and Smith, 2011). Because $[Ca^{2+}]_i$ increases leads to activation of phospholipase C and the cleavage of plasma membrane $PIP_2$, the Doc2β-$PIP_2$ interactions defined here may serve to maintain baseline spontaneous fusion rates during quiescent periods. Additionally, cAMP- and GTP-dependent signaling pathways have been shown to potentiate exocytosis in an apparently $Ca^{2+}$-independent fashion (Hille et al., 1999). Further studies, in which cellular ATP, $PIP_2$, and $Ca^{2+}$ are all carefully controlled, may more quantitatively define the role of $PIP_2$ in driving $Ca^{2+}$-independent exocytosis in live cells.

This work lends key support to the physiologic relevance of $PIP_2$ as a crucial biophysical regulatory factor for Doc2β (**Figs. 4-7)**. Syt1, by contrast, appears to rely on $PIP_2$ for pre-adsorption onto the plasma membrane (J Bai et al., 2004), rather than full membrane penetration *per se*. Our results correspond well to those reported by Pérez-Lara et al. (Pérez-Lara et al., 2016), who found that $PIP_2$ did not substantially enhance the penetration depth of syt1 in the presence of PS. The divergence between syt1 and Doc2β is readily reconciled with the specialized functions of these proteins. Doc2β operates at near resting $[Ca^{2+}]$ on slow timescales and is thus well-poised to respond to the dynamic (but relatively slow) regulation of $PIP_2$ levels at release sites. Syt1, on the other hand, must respond in microseconds to transient $Ca^{2+}$ elevations. Additional lipid requirements for full penetration by syt1 might come at a kinetic cost that would impair its capacity for triggering rapid membrane fusion. Our stopped-flow data (**Fig. 4**) support this interpretation, demonstrating that $PIP_2$ robustly stabilizes the active state of Doc2β but not syt1. The findings reported here provide an example of how two highly homologous protein sequences (the tandem C2 domains of syt1 and Doc2β) can retain core mechanistic principles while evolving highly specialized, lipid-dependent regulatory mechanisms. Other tandem-C2 domain $Ca^{2+}$ sensors may be tuned to respond to other lipid headgroups, acyl chain compositions, regulatory proteins, or even small molecules. These

regulatory functions, and how they influence the corresponding physiologic processes, remain the focus of ongoing and future studies.

**Methods**

***Protein purification*** Constructs encoding syt1 C2AB (aa 140-421) and Doc2β C2AB (aa 126-412) were expressed as N-terminal GST fusion proteins (pGEX4T-1 vector, GE) in *E. Coli*, purified via glutathione-Sepharose affinity chromatography, and cleaved with thrombin in reconstitution buffer (100 mM KCl, 25 mM HEPES-NaOH pH 7.4) plus 5% glycerol. Full-length synaptobrevin-2 was likewise expressed as a GST fusion protein, purified, and cleaved in a similar buffer containing 400 mM KCl and 1% n-octyl-D-glucopyranoside (OG). Full-length syt1 in the pTrcHis vector (Invitrogen) and full-length syntaxin-1A:SNAP-25B heterodimer in the pRSF Duet vector (EMD) were expressed as N-terminal $his_6$ fusion tags, purified via nickel-NTA-Sepharose affinity chromatography, and eluted in elution buffer (500 mM imidazole, 400 mM KCl, 25 mM HEPES-NaOH, pH 7.4, 1% OG). DTT (2 mM) was added to syx1a:SNAP-25B heterodimer and full-length syt1 to prevent aggregation. Membrane scaffolding protein MSP1E3D1(Denisov et al., 2004) was likewise purified by $Ni^{2+}$-NTA-Sepharose chromatography and eluted in elution buffer without detergent. For full-length syt1, endogenous cysteines were substituted with alanines, and the protein was expressed as an N-terminal $his_6$-SUMO fusion construct in pET28. Purified protein was subjected to on-bead labeling (see below) and eluted in elution buffer containing 0.05% n-β-dodecylmaltoside (Gold Biotechnology). Imidazole and residual free dye were removed by ultrafiltration, and the N-terminal tag was cleaved off with recombinant SENP2 protease followed by removal with $Ni^{2+}$-NTA-Sepharose resin. During purification, all lysates were treated with DNAse and RNAse, and beads bearing each Doc2β or syt1 construct were washed extensively with 1 M NaCl, 1 mM $Mg^{2+}$ to remove any bound nucleic acid contaminants.

***Protein mutagenesis and labeling*** Native cysteines (C277 in Syt1; C145, C217, C249, C290, C337, C387 in Doc2β) were removed and replaced with alanines, and exogenous cysteines were introduced at the indicated positions using site-directed mutagenesis. All mutagenesis was confirmed by Sanger

sequencing. For labeling, protein was diluted to 10 μM in 600 μl of reconstitution buffer plus 5% glycerol containing 100 μM TCEP. Iodoacetamidyl-NBD-amide (Thermo, 2 mM in DMSO) was added dropwise to this solution for a final dye:protein ratio of 10:1 (mol:mol) and the labeling reaction allowed to proceed for 2 hours at room temperature with rotation. The reaction was then quenched with DTT and the free dye removed by desalting on a column (PD MidiTrap, GE) equilibrated in reconstitution buffer plus 5% glycerol. Protein concentrations and labeling stoichiometry were determined by UV-vis absorption spectroscopy using an empirically determined extinction coefficient for NBD. Labeling efficiency ranged from 0.8-1.2 dye molecules per protein. Full-length syt1 was labeled during purification by incubating protein-bearing $Ni^{2+}$-NTA-Sepharose resin in 1 ml containing 10% DMSO and 0.5 mg iodoacetamidyl-NBD amide overnight at 4 ºC with rotation. Beads were washed extensively prior to elution.

***Liposome preparation*** Liposomes were prepared from POPC, POPS, POPE, brain $PIP_2$, and cholesterol (all from Avanti Polar Lipids) stored individually as chloroform stocks, except for brain $PIP_2$ (stored in 20:9:1 $CHCl_3$:MeOH:$H_2O$). Unless noted otherwise, liposomes contained 30% POPC, 15% POPS, 20% POPE, and 35% cholesterol (all % mol/mol). For membrane-embedded quenching studies, 15% 5-doxyl, 12-doxyl, or headgroup-doxyl-PC replaced POPC in equimolar quantity. In liposomes lacking PS, this lipid was replaced the same mole fraction of POPC. For stopped-flow rapid mixing experiments, 5% dansyl-PE replaced an equimolar amount of POPE. For liposome formulation, lipids were combined and 2-3 drops of methanol were added. The solvent was evaporated under a stream of nitrogen, and the films were dried under vacuum for at least 2 hr. Films were rehydrated in reconstitution buffer at a final concentration of 5 or 10 mM [lipid] and extruded 29 times through a single 100-nm polycarbonate filter (Whatman).

***Proteoliposome reconstitution for aggregation assays*** Proteoliposomes were formed using 15% PS, 30% PE, 55% PC, all mol %. Lipids in chloroform stocks were combined, dried under vacuum, rehydrated in reconstitution buffer, and subjected to five freeze-thaw cycles. Protein-free unilamellar vesicles were prepared from this mixture by extrusion through a 50-nm polycarbonate filter (Whatman). Syntaxin1a-SNAP-25B heterodimer (for t-SNARE–bearing liposomes) or synaptobrevin 2 (for v-

SNARE–bearing liposomes) were mixed with protein-free vesicles at a protein/lipid molar ratio of 1:200 with ~0.8 wt% octylglucoside in the buffer at 4 °C for 15 min. The mixture was diluted two times with reconstitution buffer, and this diluted mixture was then dialyzed against 2 L reconstitution buffer with 5 g of Bio-beads SM2 (Biorad) at 4 °C overnight. For aggregation studies, protein-free liposomes (pf-) were prepared in the same fashion but with the protein omitted.

***Nanodisc reconstitution*** POPC (100 nmol), MSP1E3D1 (10 nmol), and full-length labeled syt1 (2 nmol) were combined in reconstitution buffer containing 5% glycerol and 0.05% DDM. Bio-beads SM2 (Bio-Rad) were added (80 µl of a ~95% slurry in reconstitution buffer) and the mixture incubated overnight with rotation to remove DDM and permit nanodisc self-assembly.

***Aggregation assays*** C2AB (1 µM) and liposomes (113 µM lipid) were combined in 100 µl reconstitution buffer containing 200 µM EGTA, and absorbance at 400 nm was monitored in a spectrophotometer (Eppendorf) at room temperature. $Ca^{2+}$ was added at indicated points for a total of 1 mM free $Ca^{2+}$. EGTA was subsequently added for a final concentration of 2 mM [EGTA]. Independent experiments were defined as replicates performed with a unique combination of separately-prepared batches of protein and lipid.

***Stopped-flow rapid mixing*** C2AB (4 µM), liposomes (1 mM lipid), and $CaCl_2$ (250 µM for syt1, 40 µM for Doc2β) were combined in reconstitution buffer. This mixture was loaded into one syringe of an SX-18.MV stopped-flow spectrometer (Applied Photophysics) at room temperature (23 ºC) and rapidly mixed with an equal volume of 2 mM EGTA in the same buffer. Samples were allowed to equilibrate in the spectrometer for 5 min prior to mixing. Excitation at 285 nm was provided via xenon arc lamp and monochromator (Applied Photophysics), and emission was monitored via photomultiplier tube through a 470-nm long-pass filter (KV470, Schott). Single-exponential decays were fitted using Applied Photophysics Pro-Data SX software prior to normalization, with the first 2 ms of each trace omitted from analysis to account for instrument dead time. Independent experiments were defined as replicates performed with a unique combination of separately-prepared batches of protein and lipid.

***Penetration assays*** NBD-C2AB (0.25 μM) or ND-syt1 (0.15 μM syt1), liposomes (117 μM total lipid) and $Ca^{2+}$ (250 μM $[Ca]_{free}$) were combined in 600 μl of reconstitution buffer containing 500 μM EGTA. Spectra ($\lambda_{ex}$ = 390 nm; $\lambda_{em}$ = 470-630 nm) were acquired at room temperature (23 ºC) in a quartz cuvette using a QM-1 fluorimeter (Photon Technology International) after the addition of each component. In all cases, protein was added first, followed by liposomes and finally $CaCl_2$. $CaCl_2$ was added for a total $[Ca^{2+}]$ of 750 μM, of which 500 μM was chelated by EGTA, leaving a $[Ca^{2+}]_{free}$ of 250 μM. A buffer blank was subtracted from all traces. For quantification, traces were integrated by taking the average background-subtracted fluorescence intensity between 510 nm and 610 nm. Averaged traces were normalized to the background-subtracted, integrated signals from labeled C2AB prior to the addition of lipids or $Ca^{2+}$ for each replicate. Independent experiments were defined as replicates performed with a unique combination of separately-prepared batches of protein and lipid. Example spectra for penetration assays are shown in the **Appendix**.

***Depth calculations*** Measurements of bilayer penetration depths were performed according to the parallax method of London et al (Abrams and London, 1993; London and Chattopadhyay, 1987), with slight modifications used to estimate distribution widths for each probe location. This method relies on (1) a hard-sphere approximation of quenching by nitroxide radicals and (2) the relative quenching efficiencies of two quenchers at known depths in the bilayer to estimate the position of a fluorescent probe. The final equation used to derive penetration depths is (equation 1):

$$z_{cF} = L_{c1} + \left(\frac{1}{-\pi C}\ln\frac{F_1}{F_2} - {L_{21}}^2\right)/(2L_{21})$$

where $Z_{cF}$ is the distance of probe from the bilayer center, $L_{c1}$ is the distance from the bilayer center to the shallow quencher, $L_{21}$ is the difference in depth between the two quenchers, $F_1$ is the relative fluorescence intensity of the shallow quencher, $F_2$ is the relative fluorescence intensity of the deeper quencher, and $C$ is the concentration of quencher in molecules per square angstrom, assuming 20 mol %

quencher and an area of 70 square angstroms per lipid molecule. Both $F_1$ and $F_2$ are expressed as a fraction of the NBD-C2AB emission intensity obtained in the absence of doxyl-PC quencher. For values corresponding to the positions of quenchers in the bilayer, we used the results of the recent molecular dynamics simulations (Kyrychenko and Ladokhin, 2013), as these data matched previous experimental results well and also provided estimated distribution widths for the location of doxyl-PC quenchers in the bilayer. The half-widths of these distributions were propagated as errors across all mathematical operations in equation 1 to estimate half-widths for the location of each probe. Errors in $F_1$ and $F_2$ were also propagated, though the errors in these measurements were small compared to the errors corresponding to the quencher distribution widths. Distances from bilayer center were calculated using two pairs of doxyls (5- and 12-doxyl, and headgroup- and 12-doxyl). We note that the deviation in measured depth between the two pairs of doxyls used tended to increase with more deeply-located NBD probes. These deviations were < 2 angstroms in almost all cases, however, and we speculate that they occurred due to depth-dependent changes in the mobility of the NBD fluorophore and/or deviation from the hard-sphere approximation for quenching by nitroxide radicals. The average calculated depth of each NBD labeled probe using this method was shallow enough (minimum 8.6 angstroms from bilayer center) that quenching by 12-doxyl PC from the opposite leaflet of the bilayer was ignored in our calculations.

***Lipid mixing assays*** For preparation of v-SNARE liposomes, full-length syt1 and full-length synaptobrevin-2 were diluted in elution buffer and added to dried lipid films (15% PS, 7% PE, 20% Chol, 55% PC, 1.5% NBD-PE, 1.5% rhodamine-PE, all %mol/mol) at 1:2000 protein:lipid ratio, incubated for 40 minutes on ice, and dialyzed extensively against reconstitution buffer containing 1 g/L Bio-beads SM2 (Bio-Rad). The dialyzed liposome suspension was then purified by buffer exchange into reconstitution buffer using a PD-10 column (GE). T-SNARE liposomes were prepared similarly by adding t-SNARE heterodimer in elution buffer to lipid films of the same composition (1:2000 protein:lipid ratio) but without NBD-PE or rhodamine-PE and with 0, 1, 3, or 5% $PIP_2$ substituted for an equimolar amount of PC. For lipid mixing assays, v-SNARE liposomes (0.5 μM) were mixed with t-SNARE liposomes (5 μM) in 100 μl reconstitution buffer. Fluorescence (460 nm ex/520 nm em) was monitored in a plate reader

(BioTek) while incubating the reaction at 37 ºC, with $Ca^{2+}$ (500 μM) added at the indicated time point. Independent experiments were defined as replicates performed with a unique combination of separately-prepared batches of protein and lipid.

***Content mixing assays*** v-SNARE liposomes for content mixing assays were prepared as for lipid mixing assays but without NBD-PE or rhodamine-PE. t-SNARE liposomes containing $PIP_2$ and sulforhodamine B were prepared as above but with 10 mM sulforhodamine B (Acros Organics) in the elution buffer containing t-SNAREs. For content mixing assays, v-SNARE liposomes (5 μM) were mixed with t-SNARE liposomes (1 μM) in 100 μl reconstitution buffer. Fluorescence (530 nm ex/590 nm em) was monitored in a plate reader (BioTek) while incubating the reaction at 37 ºC, with $Ca^{2+}$ (500 μM) added at the indicated time point. $Ca^{2+}$ was added earlier in these experiments than in lipid-mixing experiments because longer incubations yielded content mixing that was almost entirely $Ca^{2+}$-independent in the presence of $PIP_2$. Incubation of dye-containing t-SNARE vesicles in the absence of v-SNARE vesicles did not result in dequenching (data not shown), indicating that this phenomenon was not due to leakage of dye from these vesicles. Independent experiments were defined as replicates performed with a unique combination of separately-prepared batches of protein and lipid.

***Indo-1 measurements*** Indo-1 (0.33 μM) was added to 600 uL reconstitution buffer containing 500 μM EGTA, followed by PS:$PIP_2$ liposomes (0.117 μM) and $Ca^{2+}$ (250 μM) with spectra taken ($\lambda_{ex}$ = 332 nm) after each addition. $[Ca^{2+}]_{free}$ was estimated by comparison with reference spectra (Grynkiewicz et al., 1985).

**Tables and Figures**

| **Membrane penetration parameters for Doc2β C2AB** | | | | | | | | | |
|---|---|---|---|---|---|---|---|---|---|
| | **C2A*(1)** | | **C2A*(3)** | | **C2B*(1)** | | **C2B*(3)** | | **EGTA: C2B*(3)** |
| | PS | PS:PIP2 | PS | PS:PIP2 | PS | PS:PIP2 | PS | PS:PIP2 | PS:PIP2 |
| $z_{HG-12}$, Å: | 13.6 ± 8.4 | 12.8 ± 8.4 | 14.2 ± 8.5 | 12.2 ± 8.4 | 13.2 ± 8.4 | 12.1 ± 8.4 | 12.6 ± 8.4 | 11.5 ± 8.4 | 13.8 ± 8.4 |
| $z_{5-12}$, Å: | 12.8 ± 8.3 | 10.5 ± 7.6 | 14.6 ± 9.3 | 9.0 ± 7.5 | 11.5 ± 7.8 | 9.6 ± 7.5 | 10.2 ± 7.5 | 8.6 ± 7.5 | 14.4 ± 7.5 |
| $\Delta z_{(av),\ PS-PIP2}$, Å: | 1.6 | | 3.7 | | 1.5 | | 1.3 | | - |

| **Membrane penetration parameters for Syt1 C2AB** | | | | | | | | | |
|---|---|---|---|---|---|---|---|---|---|
| | **C2A*(1)** | | **C2A*(3)** | | **C2B*(1)** | | **C2B*(3)** | | **EGTA: C2B*(3)** |
| | PS | PS:PIP2 | PS | PS:PIP2 | PS | PS:PIP2 | PS | PS:PIP2 | PS:PIP2 |
| $z_{HG-12}$, Å | 12.9 ± 8.4 | 12.9 ± 8.4 | 12.5 ± 8.4 | 11.9 ± 8.4 | 13.4 ± 8.4 | 13.0 ± 8.4 | 12.4 ± 8.4 | 12.1 ± 8.4 | 13.9 ± 8.4 |
| $z_{5-12}$, Å | 10.8 ± 7.6 | 10.4 ± 7.5 | 10.2 ± 7.5 | 8.9 ± 7.5 | 11.6 ± 7.8 | 10.8 ± 7.6 | 9.3 ± 7.5 | 8.9 ± 7.5 | 12.9 ± 8.3 |
| $\Delta z_{(av),\ PS-PIP2}$, Å | 0.2 | | 0.9 | | 0.6 | | 0.4 | | - |

**Table 1. Calculated depth parameters from doxyl quenching experiments.** Membrane insertion depth was calculated by measuring the relative quenching efficiencies of doxyl spin labels located at different positions on the lipid acyl chains according to the methods described by Chatthopadhyay and London (1987). Values of *z* indicate distance from the center of the bilayer, in Angstroms, and subscripts denote the doxyl pair used to calculate this distance. Each value represents the calculated average distance of the NBD label from the center of the bilayer. Errors represent half-widths of the calculated depth distributions based on molecular dynamics simulations of doxyl quenchers by Kyrychenko et al. (2013). See Methods for details on calculations and error propagation.

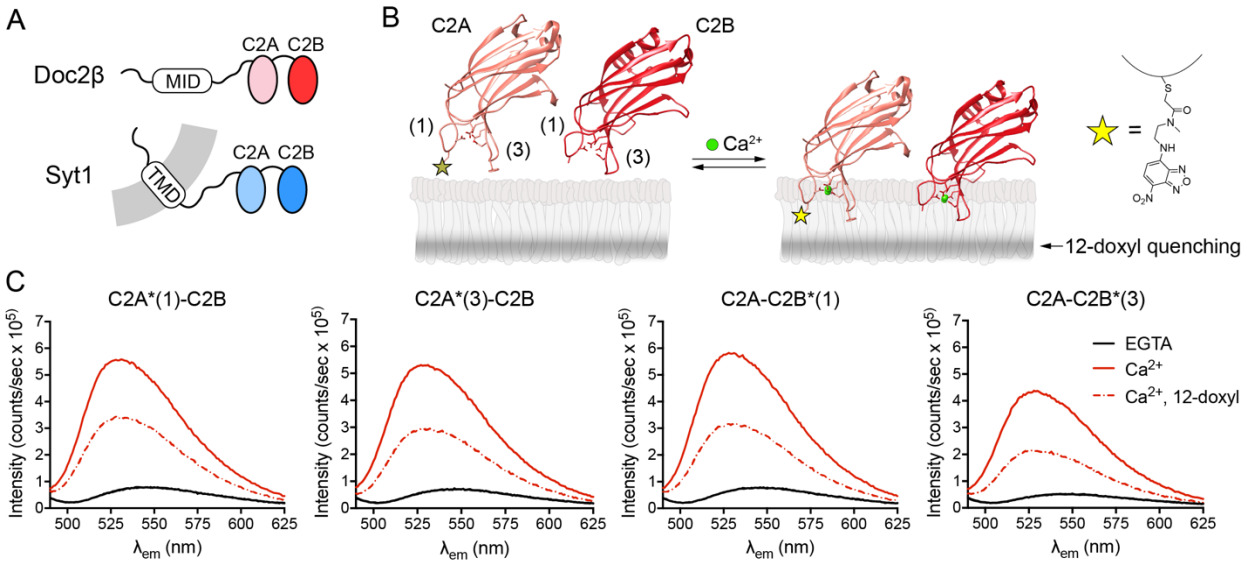


**Figure 1. Doc2β penetrates membranes in response to $Ca^{2+}$.** (A) Schematic diagrams of syt1 and Doc2β. MID, munc13-interacting domain; TMD, transmembrane domain. (B) Model illustrating the putative membrane penetration activity of Doc2, where the distal tip of $Ca^{2+}$-binding loop 1 was mutated to cysteine and labeled with the fluorescent dye NBD, shown at right. The shaded stripe in the bilayer leaflet depicts the approximate distribution of the quenching nitroxide on 12-doxyl-PC. Ribbon diagrams, C2A (PDB 4LCV) and C2B (PDB 4LDC) of Doc2β from Giladi et al. (2013)(Giladi et al., 2013). (C) NBD emission spectra from each of the four $Ca^{2+}$-binding loops of Doc2β C2AB. Graph titles indicate the C2 domain and loop labeled (e.g., C2A*(1)-C2B corresponds to loop 1 of C2A, while C2A*(3)-C2B corresponds to loop 3 of C2A). Labeled C2AB was combined with liposomes (15% PS, 30% PC, 20% PE, 35% cholesterol) in 500 μM EGTA, after which $Ca^{2+}$ was added (250 $\mu$M free [$Ca^{2+}$]). $Ca^{2+}$ triggered an intensity increase and blue shift in the emission spectra at all four labeling sites, suggesting burial of the probe into the bilayer. Membrane insertion was confirmed with the use of liposomes containing 15% 12-doxyl PC, which efficiently quenched the fluorescence at each labeled site. Spectra are representative of data from at least 4 independent trials.

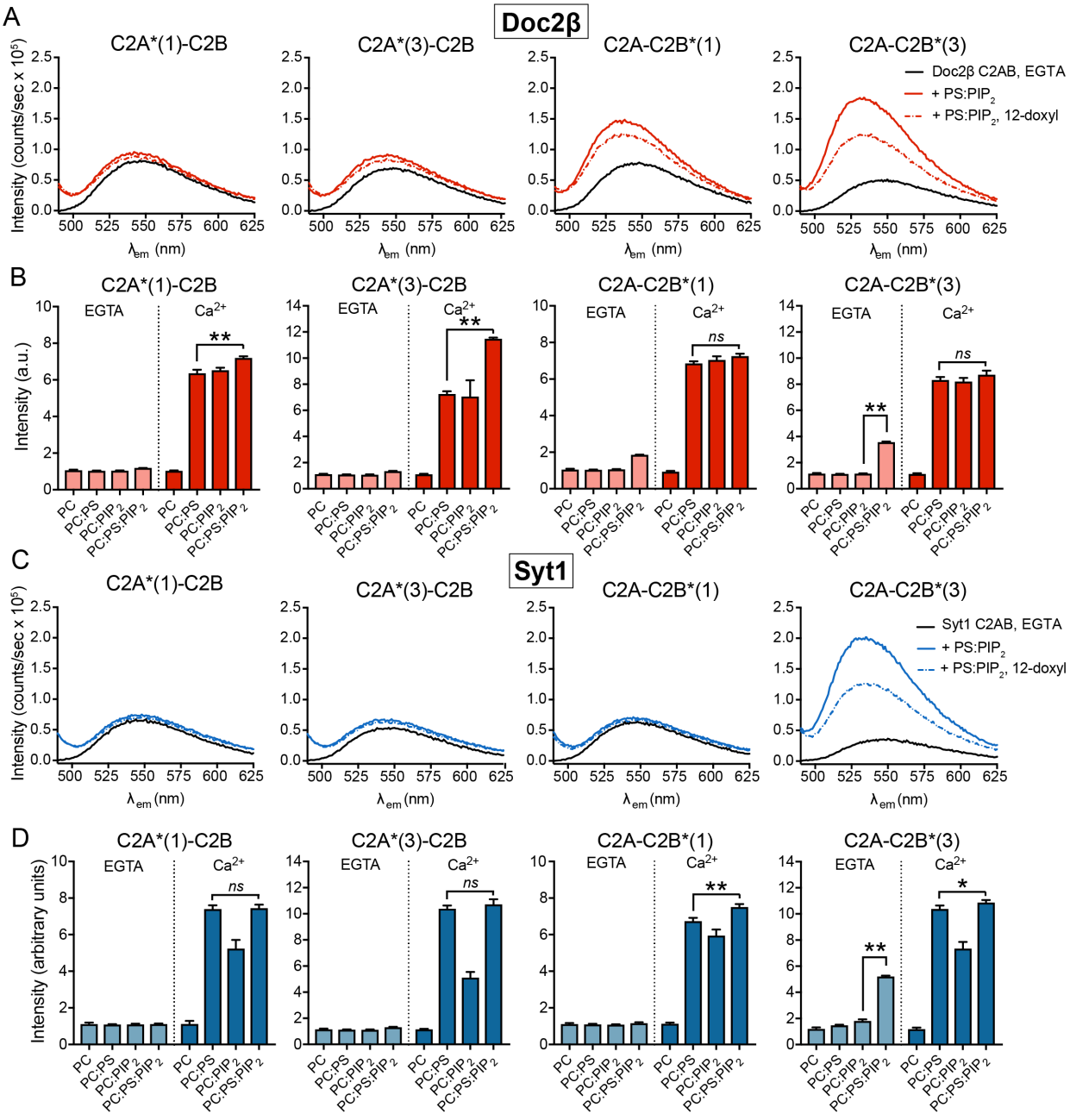


**Figure 2. PS and $PIP_2$ synergistically drive $Ca^{2+}$-independent membrane penetration by syt1 and Doc2β but exert different effects on each protein.** (A) Emission spectra of NBD labeled Doc2β C2AB before and after the addition of liposomes containing 15 mol % PS and 1 mol % $PIP_2$ in 500 μM EGTA (≤10 nM $[Ca]_{free}$). Under these conditions, loops 1 and 3 of C2B demonstrate robust increases in emission intensity. Emission from loop 3 is efficiently quenched by 12-doxyl PC, indicating $Ca^{2+}$-independent insertion into the bilayer. Spectra are representative of data from at least 4 independent trials. (B) NBD-labeled Doc2β C2AB was combined with the indicated liposomes and the NBD emission intensity was measured before and after the addition of $Ca^{2+}$. For each replicate, emission intensity was normalized to the signal from NBD-labeled protein prior to liposome addition. For Doc2β, PS and $PIP_2$ each support $Ca^{2+}$-dependent penetration activity. However, when combined, PS and $PIP_2$ drove a marked $Ca^{2+}$-dependent increase in the emission from C2A, loop 3. Both PS and $PIP_2$ were required for $Ca^{2+}$-

independent penetration by loops 1 and 3 of C2B (arrows). (C,D) Same as above, but using syt1 C2AB. In contrast to Doc2β C2AB, PS drives penetration of syt1 C2A more efficiently than $PIP_2$ in the presence of $Ca^{2+}$. The combination of $PIP_2$ and PS did not drive any additional NBD signal increases in C2A but marginally increased NBD signals in C2B. As with Doc2β, both $PIP_2$ and PS were required for robust $Ca^{2+}$-independent penetration by Syt1 C2B, loop 3 (arrow). Error bars, SEMs of 4 independent trials; *, $p < 0.05$; **, $p < 0.005$; ns, $p > 0.5$; all by Welch's *t*-test.

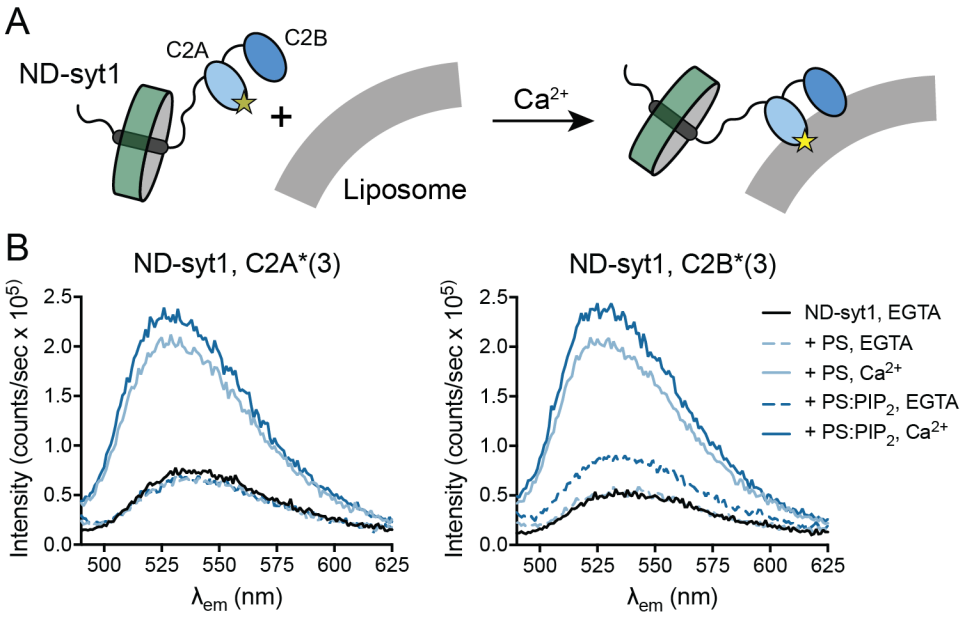


**Figure 3. Membrane penetration by full-length syt1 reconstituted into nanodiscs.** (A) Experimental scheme. Full-length syt1 was purified, labeled with NBD on loop 3 of C2A or loop 3 of C2B, and reconstituted into 13-nm diameter nanodiscs comprising membrane scaffolding protein and POPC (ND-syt1). ND-syt1 was combined with liposomes containing acidic phospholipids in EGTA (500 μM) followed by the addition of $Ca^{2+}$ to assay $Ca^{2+}$-independent and $Ca^{2+}$-dependent membrane penetration activity. (B) Representative spectra for penetration experiments with ND-syt1. As with syt1 C2AB, $Ca^{2+}$ and acidic phospholipids caused an increase and blue shift in NBD fluorescence. Likewise, in the presence of both PS and $PIP_2$, $Ca^{2+}$-independent penetration by C2B, but not C2A, was observed. Spectra are representative of results from 4 independent trials.

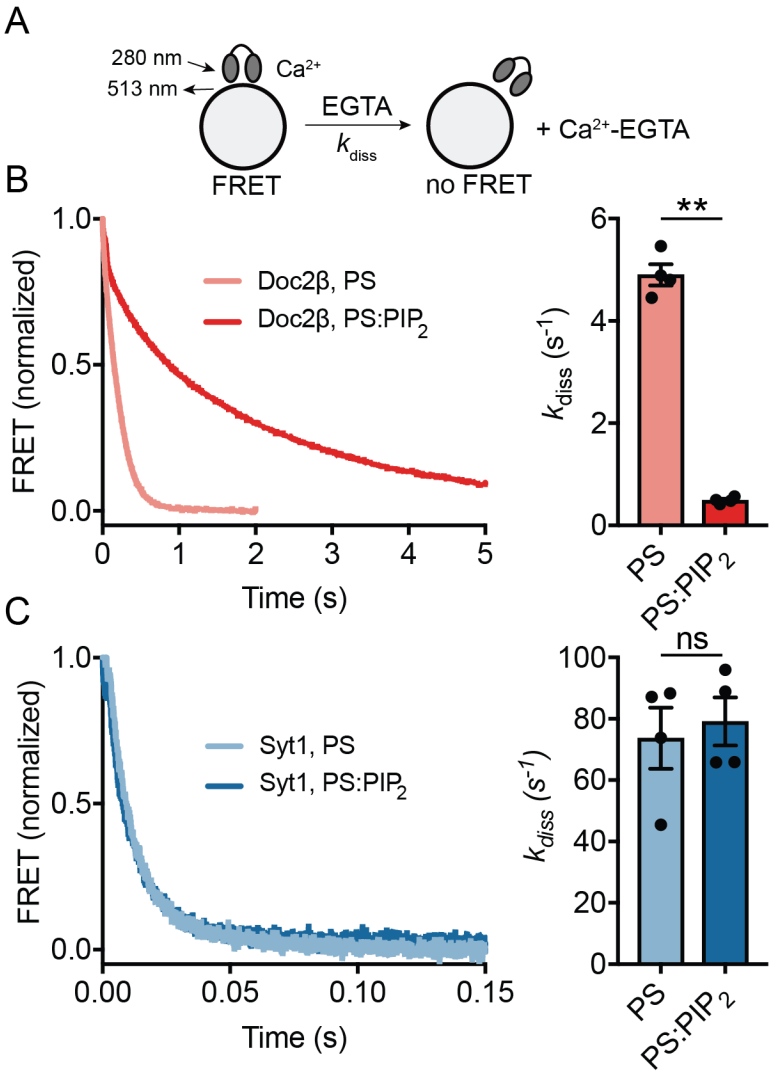


**Figure 4. $PIP_2$ slows the disassembly kinetics of C2AB-$Ca^{2+}$-liposome complexes containing Doc2β but not syt1.** (A) Schematic of disassembly assay. C2AB-$Ca^{2+}$-liposome complexes were pre-assembled and then rapidly mixed with EGTA while monitoring FRET between tryptophan residues in C2AB and dansyl-PE acceptors on the liposomes. (B) Representative traces (left) and rate constants derived from single-exponential fits (right) for disassembly of Doc2β-$Ca^{2+}$-membrane complexes. The inclusion of 1 mol % $PIP_2$ in liposomes containing 15% PS slowed the observed rates of disassembly by approximately ten-fold. (C) As above, but for syt1 C2AB. In contrast to the case of Doc2β, membrane complex disassembly rates for syt1 were unchanged with the inclusion of 1 mol % $PIP_2$. Error bars, SEMs of 4 independent trials; **, $p < 0.005$; ns, $p > 0.5$; both by Welch's *t*-test.

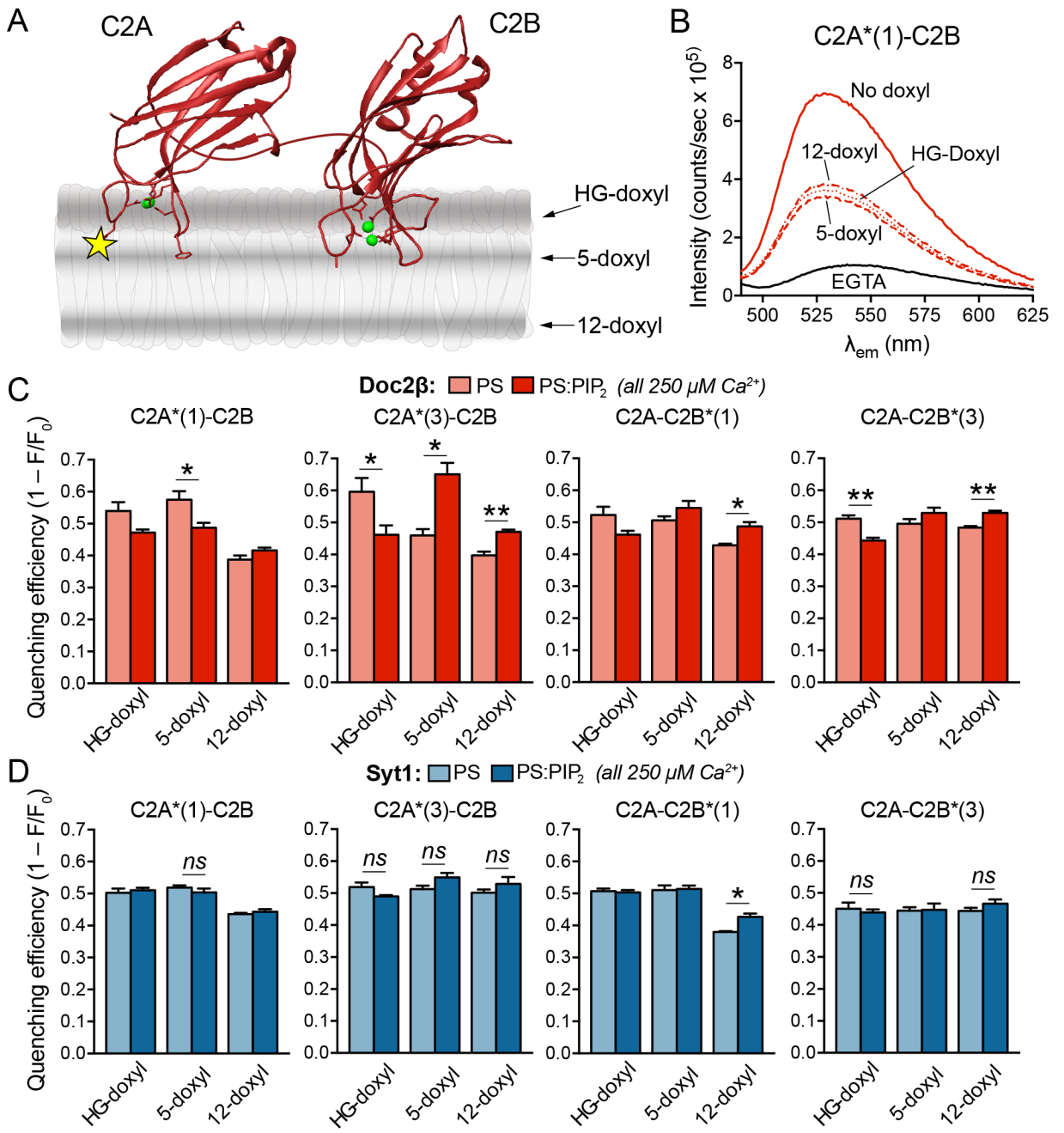


**Figure 5. $PIP_2$ markedly deepens membrane penetration by Doc2β but not syt1**. (A) Illustration depicting membrane-bound C2AB and the approximate distributions of nitroxide quenchers. Yellow star represents NBD label, green spheres represent $Ca^{2+}$ ions. (B) Representative emission spectra for non-quenching liposomes along with liposomes containing the indicated doxyl quencher. Relative quenching efficiencies at different probe locations correspond to the average location of the NBD label in the bilayer. Deeper insertion results in stronger quenching by 12-doxyl versus 5-doxyl and HG-doxyl liposomes, while shallower insertion results in stronger quenching by HG-doxyl and 5-doxyl liposomes. (C) NBD-labeled Doc2β C2AB was combined with liposomes and $Ca^{2+}$ (250 $\mu$M); quenching efficiencies of doxyl-PC liposomes with and without $PIP_2$ were quantified. Inclusion of $PIP_2$ drives both loops of C2A deeper into the bilayer, as evinced by reduced shallow quenching and increased deep quenching. This effect is also apparent for Doc2β C2B. (D) Same as in (C), but using NBD-labeled syt1. In contrast to Doc2β, syt1 C2A penetrates deeply in the absence of $PIP_2$, as shown by relatively efficient quenching by

12-doxyl liposomes. In contrast to the case of Doc2β, $PIP_2$ exhibits only a weak tendency to drive additional penetration by syt1. Error bars, SEMs of 4 independent trials; *, $p < 0.05$; **, $p < 0.005$; ns or unmarked, $p > 0.5$; all by Welch's *t*-test.

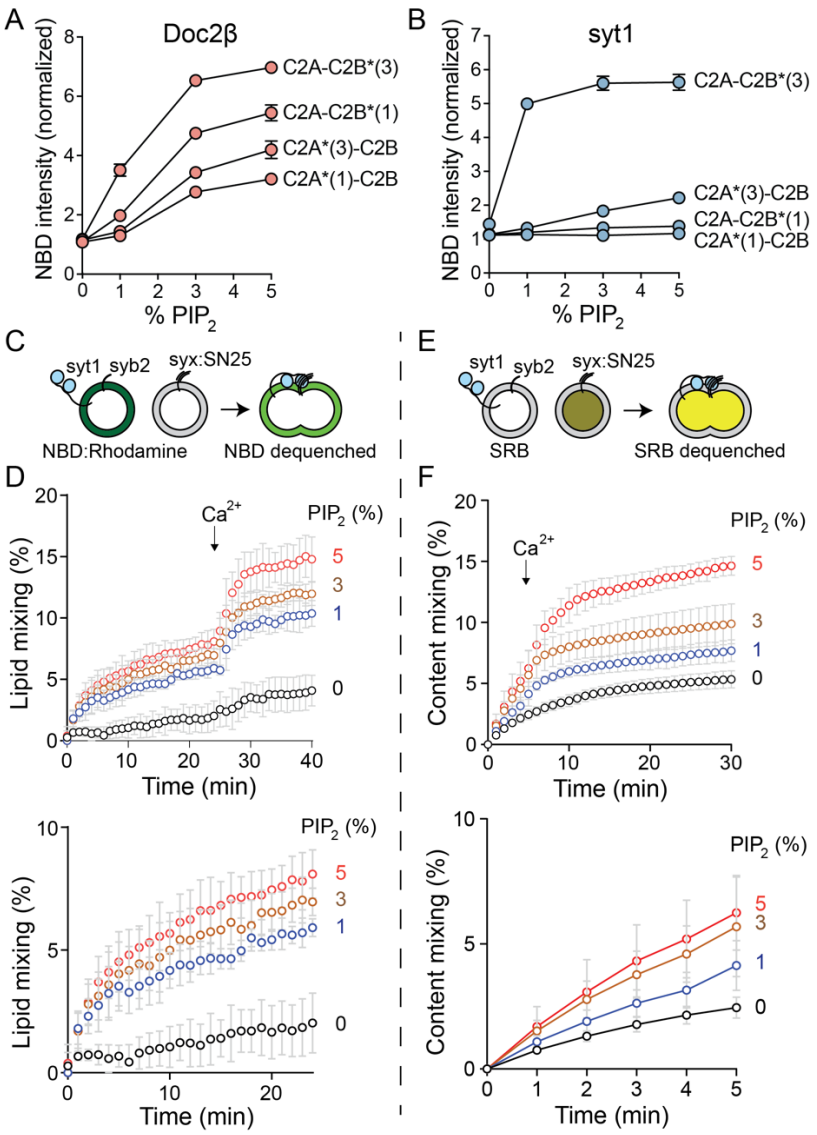


**Figure 6. Increasing [$PIP_2$] drives $Ca^{2+}$-independent penetration by both C2 domains of Doc2β and syt1 and potentiates $Ca^{2+}$-independent and -dependent vesicle fusion.** (A) NBD-labeled Doc2β C2AB was combined with liposomes harboring PS and increasing concentrations of $PIP_2$ in the absence of $Ca^{2+}$, and NBD emission intensity was quantified. Increasing [$PIP_2$] drove substantial intensity increases from NBD labels on all 4 loops of Doc2β. This effect appeared to reach near-saturation at 5 mol % $PIP_2$. (B) as in (A) but for syt1 C2AB. In addition to robust penetration by C2B, loop 3, increasing [$PIP_2$] drove partial penetration by C2A, loop 3. (C-F) v-SNARE liposomes containing full-length syb2 and full-length syt1 were combined with t-SNARE liposomes containing full-length syntaxin-1a:SNAP-25B heterodimer and increasing mol % $PIP_2$. (C) Scheme of lipid mixing assay. Fusion of vesicles was monitored by dequenching of NBD. (D) Results of lipid-mixing assays conducted with increasing mol % $PIP_2$ in the t-SNARE vesicles. Above, full traces; below, $Ca^{2+}$-free portion of the trace shown on an expanded timescale. $PIP_2$ drove $Ca^{2+}$-independent and -dependent lipid mixing in a dose-dependent manner. (E) Scheme of content mixing assay. Fusion of vesicles was monitored by dequenching of sulforhodamine B. (F) Results of content-mixing assays conducted with increasing mol % $PIP_2$ in the t-SNARE vesicles. Above, full traces; below, $Ca^{2+}$-free portion of the trace shown on an expanded timescale. As with lipid-mixing experiments, a dose-dependent effect of $PIP_2$ on $Ca^{2+}$-independent and -dependent fusion was observed. Error bars, SEMs of 4 independent trials.

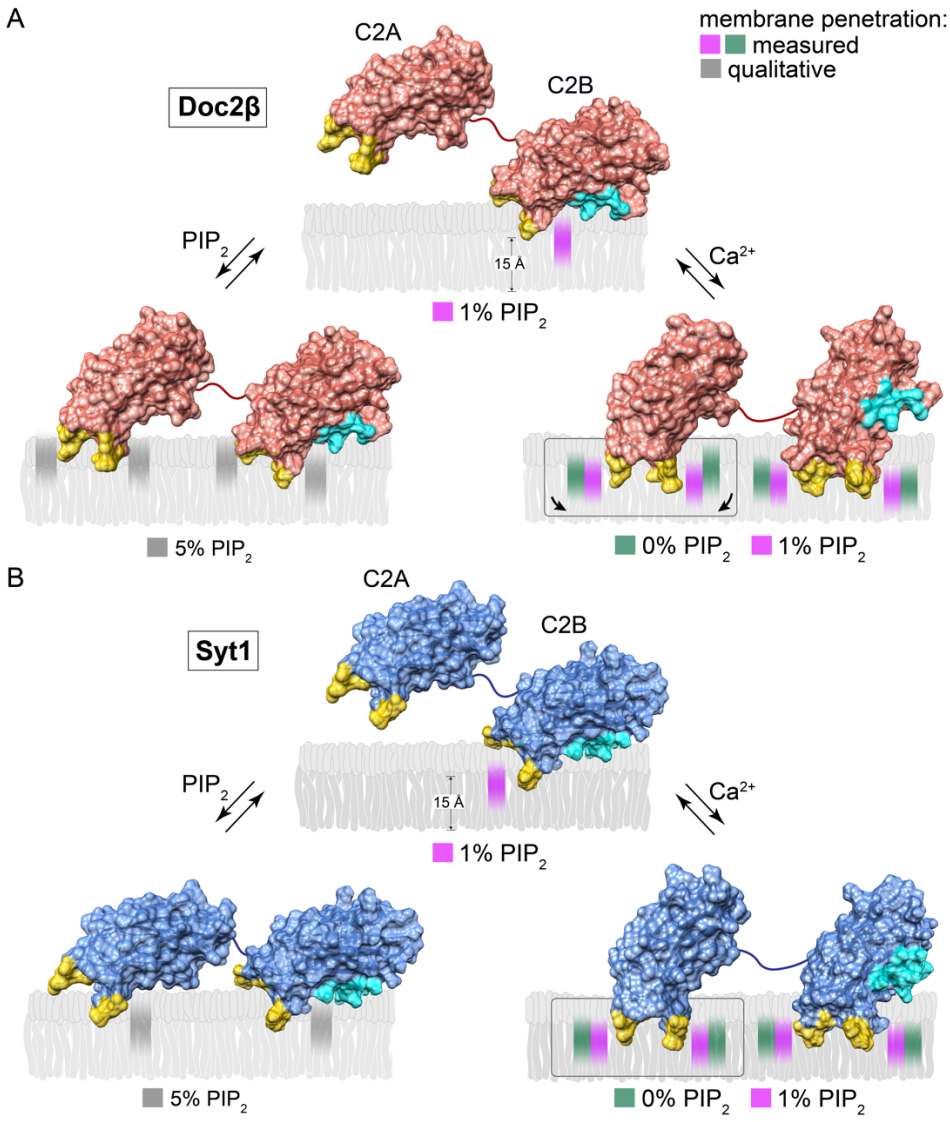


**Figure 7. Model of $Ca^{2+}$-dependent and -independent membrane penetration by Doc2β and syt1 in the presence and absence of $PIP_2$.** Calculated membrane penetration depths are illustrated, to scale, for Doc2β and syt1. Models of syt1 and Doc2 were created by rendering the molecular surfaces of the corresponding X-ray or NMR structures (Doc2: as above; syt1: PDB 1RSY (C2A), 1K5W (C2B), from Sutton et al. (1995) and Fernandez et al. (2001), respectively). The polybasic patch of C2B is rendered cyan in each model. Shaded areas in the bilayer represent the calculated half-widths of the penetration depth measurements for each probe. (A) Scale drawing of membrane penetration by Doc2β. Prior to binding $Ca^{2+}$, C2B shallowly penetrates bilayers in the presence of 1% $PIP_2$. After binding $Ca^{2+}$, all four loops penetrate the bilayer. However, both loops in C2A are relegated to a shallow position unless $PIP_2$ is also present, which enables C2A loop 3 to penetrate 3.7 angstroms deeper on average into the membrane. In the absence of $Ca^{2+}$, increases in mol % $PIP_2$ in the target membrane can drive partial penetration of the bilayer by all four loops of Doc2β. (B) Scale drawing of membrane penetration by syt1. As with Doc2β, 1% $PIP_2$ enables $Ca^{2+}$-independent penetration by C2B, loop 3, and increasing [$PIP_2$] drives penetration by C2A, loop 3. Upon binding $Ca^{2+}$, however, all four loops of syt1 penetrate deeply into the membrane

even in the absence of $PIP_2$.

## Appendix

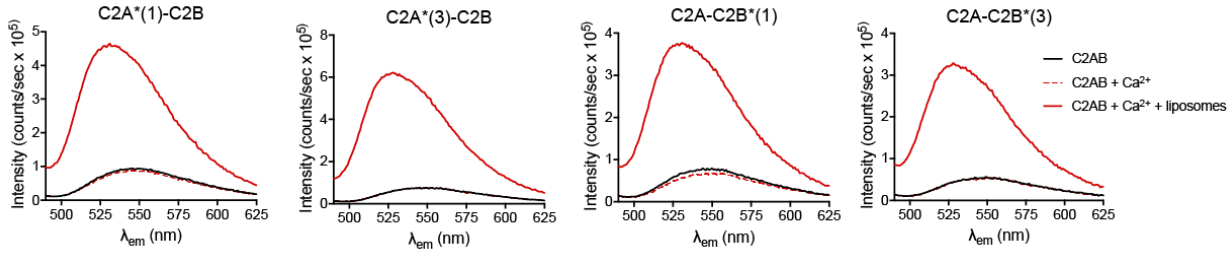


**Figure S1. NBD emission intensity increases require the presence of lipids and $Ca^{2+}$.** Labeled C2AB fragments of Doc2β were combined with $Ca^{2+}$ (250 μM) prior to the addition of liposomes. No increase in NBD fluorescence was observed unless both $Ca^{2+}$ and liposomes were present. Spectra are representative of results from two independent trials.

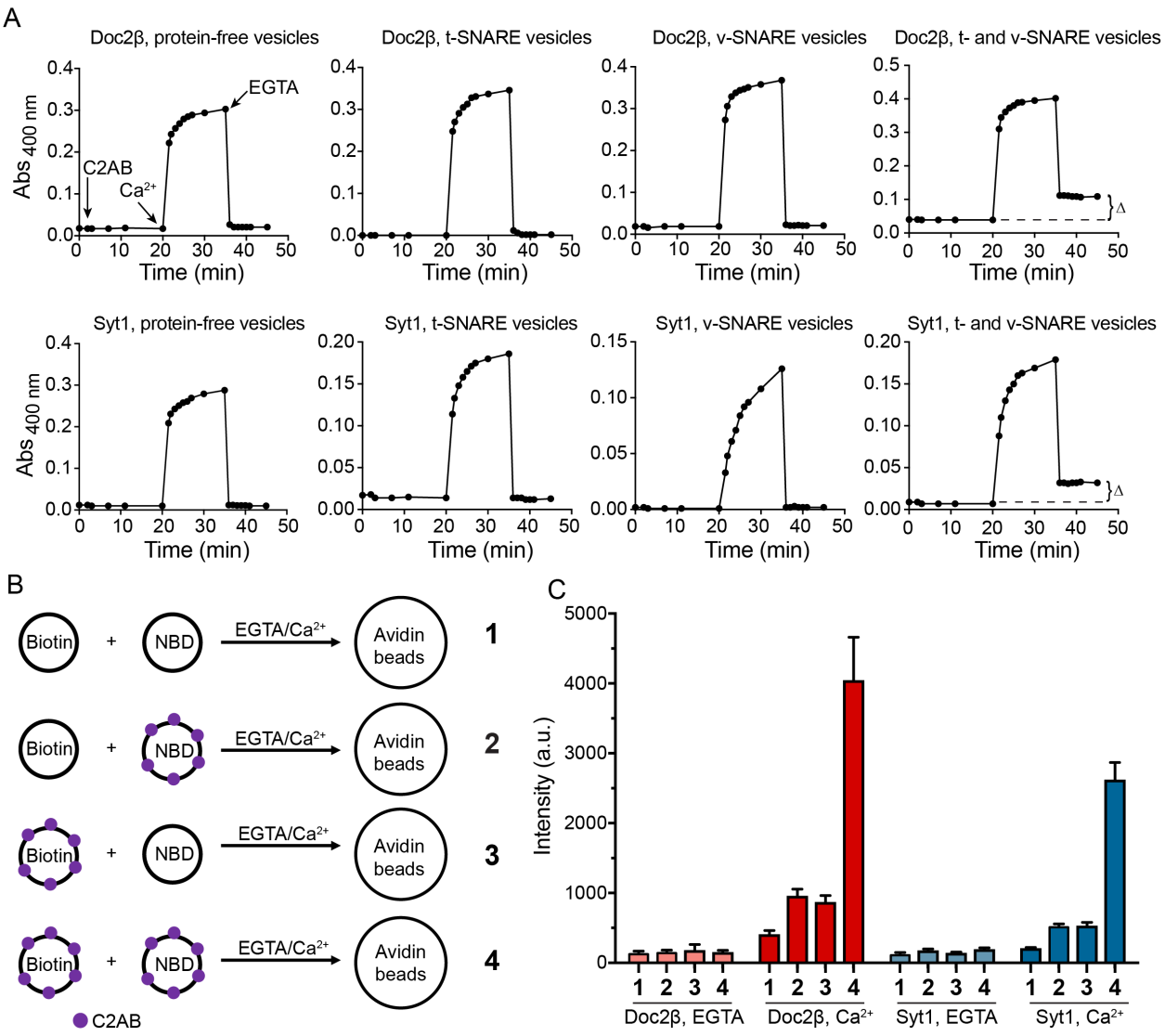


**Figure S2. Doc2β, like syt1, aggregates membranes via a back-to-back *trans* mechanism.** (A) Liposome aggregation mediated by syt1 and Doc2 was measured via absorbance at 400 nm after adding C2AB and $Ca^{2+}$ to liposomes of the indicated composition. $Ca^{2+}$ was added at 20 minutes, EGTA at 35 minutes. t-SNARE vesicles harbored reconstituted full-length SNAP-25:syntaxin-1 heterodimer and v-SNARE vesicles harbored reconstituted full-length synaptobrevin-2. Aggregation-induced absorbance increases were reversible for both proteins unless both t- and v-SNARE vesicles were included, in which case a residual absorbance increase persisted. (B) Schematic for pull-down assay to determine mechanism of vesicle aggregation. Liposomes bearing biotin-PE or NBD-PE were incubated with or without C2AB in EGTA or $Ca^{2+}$; in the latter case, C2AB is "pinned" to the vesicles due to its very slow off-rate in the presence of $Ca^{2+}$. NBD- and biotin-labeled liposomes were mixed, biotin liposomes were collected using avidin beads, and bead-bound NBD fluorescence was measured. (C) Quantification of bead-bound fluorescence. A small degree of liposome-liposome binding was observed when C2AB was pinned to one set of liposomes; pinning C2AB to both sets of liposomes dramatically increased liposome-liposome binding, suggesting that C2AB molecules associate in *trans* to mediate liposome aggregation. Error bars, standard error of the means (SEMs) of 3 independent trials.

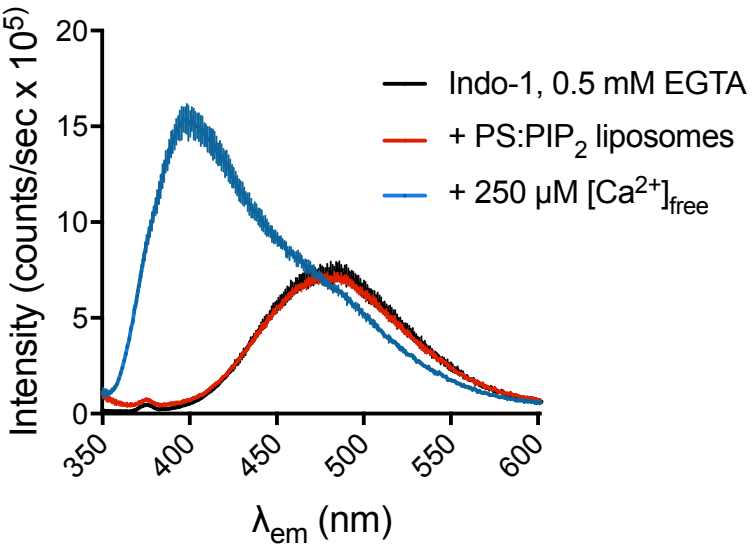


**Fig. S3: PS:$PIP_2$ liposomes do not increase $[Ca^{2+}]_{free}$.** Liposomes were added to 0.33 μM indo-1 in reconstitution buffer. A negligible increase at in the fluorescence at 400 nm, likely caused by scattering from liposomes, demonstrates that $[Ca^{2+}]_{free}$ remained < 10 nM after addition of PS:$PIP_2$ liposomes. Spectra are plotted as means +/- standard deviation for 3 separate batches of PS:$PIP_2$ liposomes.

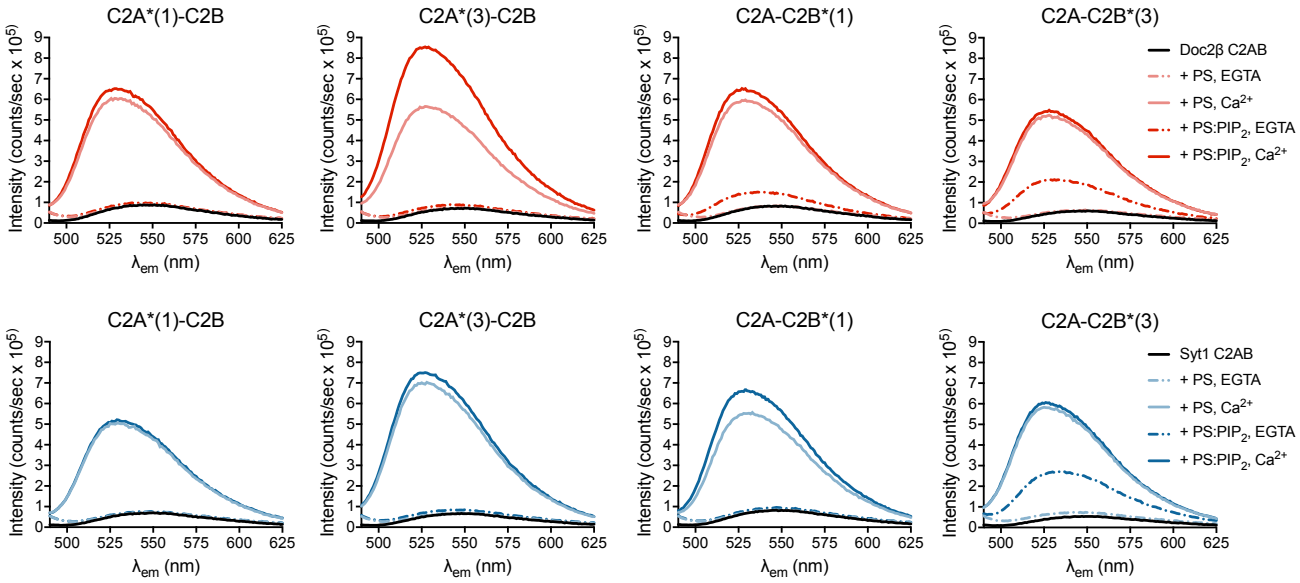


**Fig. S4. Representative spectra from penetration assays demonstrating effect of 1% $PIP_2$ on penetration of liposomes containing PS in the presence and absence of 250 µM $[Ca^{2+}]_{free}$** (related to Figure 2, main text).

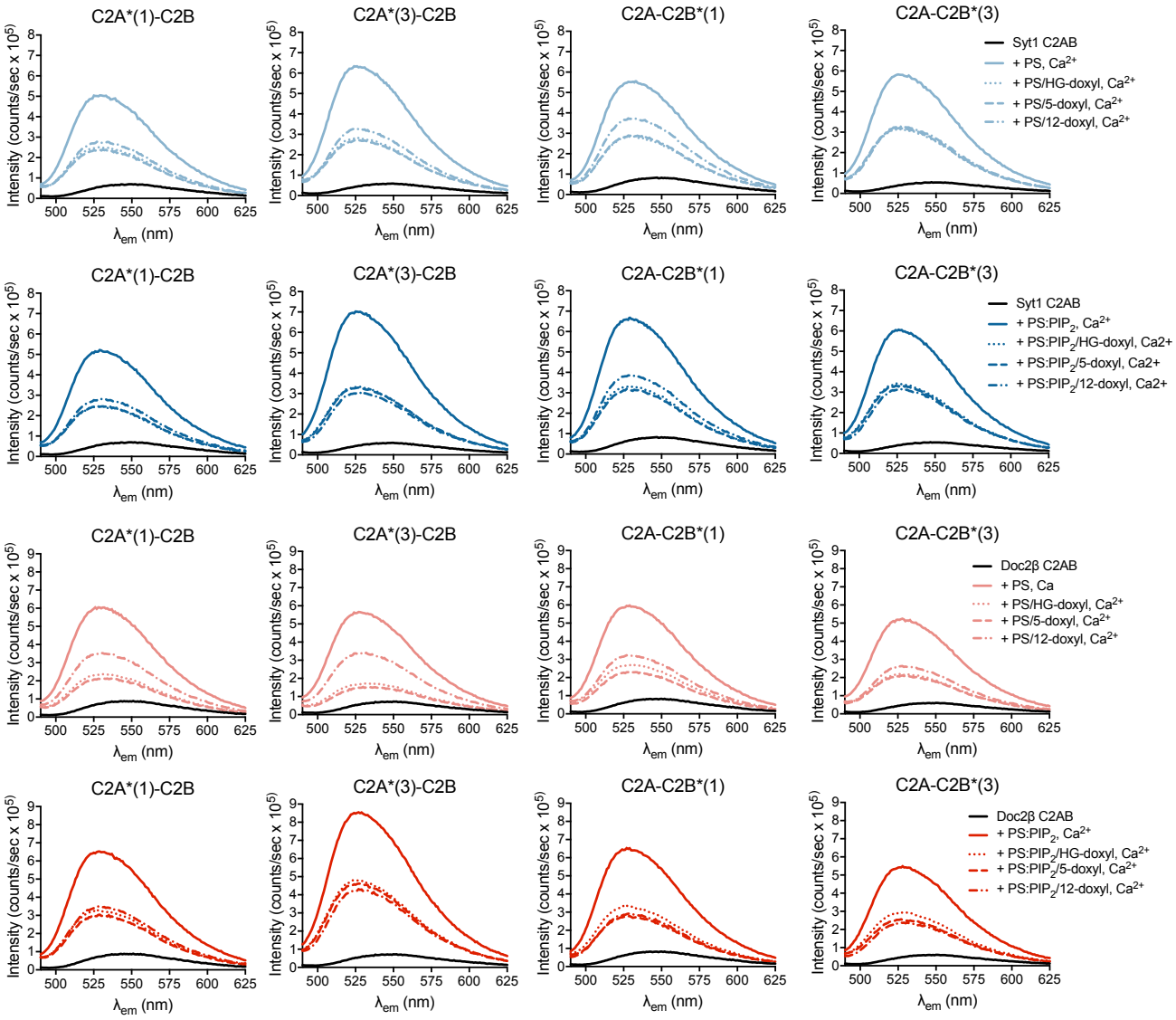


**Fig. S5. Representative spectra from doxyl quenching experiments demonstrating effect of 1% $PIP_2$ on penetration of liposomes containing PS in the presence of 250 µM $[Ca^{2+}]_{free}$** (related to Figure 5, main text).

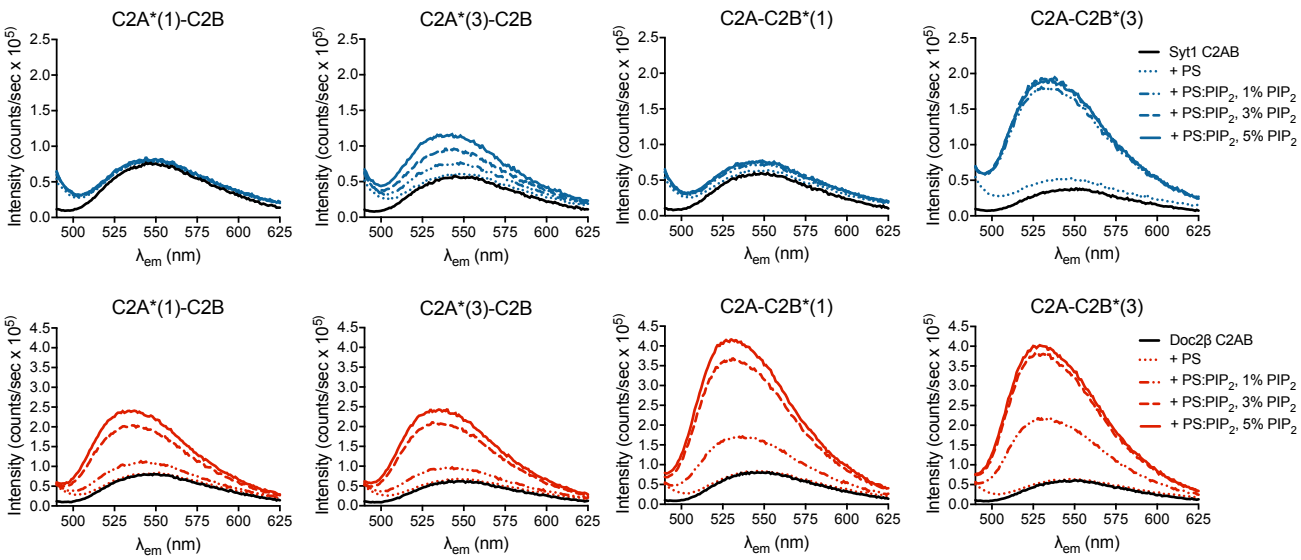


**Fig. S6. Representative spectra demonstrating effect of increasing $PIP_2$ on penetration of liposomes containing PS in 500 µM EGTA** (related to Figure 6, main text).

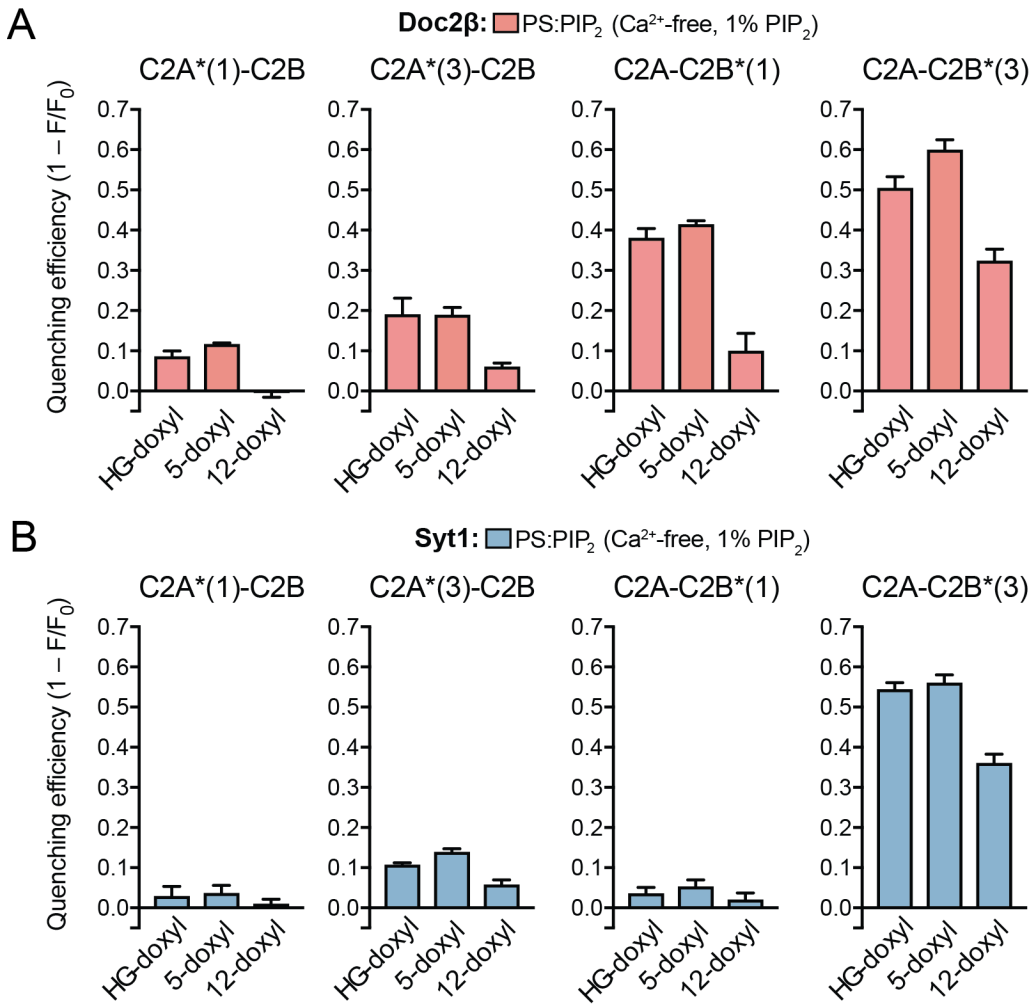


**Figure S7. Doxyl quenching of NBD-labeled Doc2β and syt1 in EGTA.** (A) NBD-labeled Doc2β C2AB was combined with PS:$PIP_2$ liposomes (1 mol % $PIP_2$) in 500 μM EGTA, and quenching efficiencies of doxyl-PC liposomes were quantified. Quenching of loops in C2A was far weaker than in C2B, consistent with localization of $Ca^{2+}$-independent penetration to the C2B domain. (B) as in (A) but for syt1 C2AB. In contrast to Doc2β minimal quenching was observed for C2B, loop 1. Both proteins showed weak quenching of C2A, loop 3, along with the expected robust quenching of C2B, loop 3. Error bars, SEMs of 4 independent trials.

## Chapter 3: Molecular basis for synaptotagmin-1-associated neurodevelopmental disorder

### Summary

At neuronal synapses, synaptotagmin-1 (syt1) acts as a $Ca^{2+}$ sensor that synchronizes neurotransmitter release with $Ca^{2+}$ influx during action potential firing. Heterozygous missense mutations in syt1 have recently been associated with a severe but heterogeneous developmental syndrome, termed syt1-associated neurodevelopmental disorder. Well-defined pathogenic mechanisms, and the basis for phenotypic heterogeneity in this disorder, remain unknown. Here, we report the clinical, physiological, and biophysical characterization of three syt1 mutations from human patients. Synaptic transmission was impaired in neurons expressing mutant variants, which demonstrated potent, graded dominant-negative effects. Biophysical interrogation of the mutant variants revealed novel mechanistic features concerning the cooperative action, and functional specialization, of the tandem $Ca^{2+}$-sensing domains of syt1. These mechanistic studies led to the discovery that a clinically approved $K^+$ channel antagonist is able to rescue the dominant-negative heterozygous phenotype. Our results establish a molecular cause, basis for phenotypic heterogeneity, and potential treatment approach for syt1-associated neurodevelopmental disorder.

### Introduction

At presynaptic terminals, neurotransmission is triggered by an elevation in cytosolic $Ca^{2+}$ ($[Ca^{2+}]_i$) that occurs upon the arrival of an action potential (B. Katz and Miledi, 1967). In most terminals, tandem-C2 domain proteins in the synaptotagmin (syt) family trigger the fusion of vesicular and plasma membranes via $Ca^{2+}$-dependent interactions with phospholipid bilayers (Mackler et al., 2002; Tucker, 2004). Synaptic vesicle (SV)-plasma membrane fusion is catalyzed by soluble *N*-ethylmaleimide sensitive factor attachment protein receptors (SNAREs) (Sudhof and Rothman, 2009; Weber et al., 1998), and several syt isoforms likely stimulate this process by promoting vesicle docking (Chang et al., 2018; Liu et al., 2009; Reist et al., 1998), deforming the plasma membrane via $Ca^{2+}$-dependent membrane penetration by both C2 domains, C2A and C2B (**Fig. 1A**) (Bai et al., 2016b; Evans et al., 2015b; Hui et al., 2009b;

Liu et al., 2014), and potentially controlling the assembly of trans-SNARE complexes ((Bhalla et al., 2006; Kiessling et al., 2018; Zhou et al., 2015), but see also (Bai et al., 2016b; Park et al., 2015)). Since each of these mechanistic findings continue to be the subject of debate, it is crucial to further address the precise biophysical action of syt1 in order to elucidate the molecular mechanisms that underlie excitation-secretion coupling (Brose et al., 2019).

Recently, a series of case reports has established a link between *de novo* heterozygous mutations in the gene encoding synaptotagmin-1 (syt1), the predominant syt isoform in the central nervous system (CNS), and a severe developmental syndrome (Baker et al., 2018, 2015). Patients with syt1-associated neurodevelopmental disorder demonstrate infantile hypotonia, profound intellectual disability, disordered movement, and electroencephalographic abnormalities without epilepsy or gross neuroanatomic abnormalities (Baker et al., 2018). The observed phenotypes vary widely in severity, but the basis for phenotypic heterogeneity in syt1-associated neurodevelopmental disorder is not known. Previous studies indicate that other point mutations in syt1 can have dominant-negative effects in *Drosophila* (Mackler et al., 2002) and in cultured mouse neurons (Wu et al., 2017). Whether, and how, disease-associated mutations in syt1 exert dominant-negative effects on synaptic transmission are crucial issues that have not been explored. Moreover, it remains unclear why all disease-associated mutations are clustered in the $Ca^{2+}$-binding, membrane-penetrating loops of the C2B domain.

In the present study, we establish a molecular basis for the cause and potential treatment of syt1-associated neurodevelopmental disorder. We first highlight three clinical cases that illustrate the severity and phenotypic heterogeneity of this disorder. X-ray crystallography of mutant syt1 variants demonstrates the physicochemical diversity of disease-associated mutations. Assays of synaptic transmission and neurotransmitter release, with controlled mutant:WT expression ratios, unambiguously provide evidence for a dominant-negative action that correlates in potency with the observed clinical severity. Biophysical and biochemical measurements establish a deleterious impact of the mutations that likewise correlates with the synaptic and human phenotypes. These experiments revealed a novel difference between the two C2 domains of synaptotagmin-1: while C2A and C2B bind $Ca^{2+}$ cooperatively to penetrate membranes,

C2B exhibits a substantially higher sensitivity to $Ca^{2+}$ that is impaired in a graded fashion by each disease-causing mutation. Finally, we show that the heterozygous mutant phenotype can be rescued with a clinically approved, centrally acting $K^+$ channel antagonist, establishing a plausible approach to pharmacotherapy for syt1-associated neurodevelopmental disorder.

## Results

### *Clinical manifestations of pathogenic syt1 mutations*

**Table 1** summarizes three exemplary cases of syt1-associated neurodevelopmental disorder. Clinical histories for each patient with a mutant variant were obtained from published studies (I368T) (Baker et al., 2015) or clinical records and interviews with parents (D304G, D366E). In each case, heterozygous *de novo* mutations in *SYT1* were discovered by whole-exome sequencing, which excluded a causal role for inherited mutations. As noted in the case series by Baker et al (2018), these mutations are associated with a profound global developmental delay that varies widely in severity. All patients exhibited hypotonia and delayed motor development apparent in the first year of life. As with patient I368T, magnetic resonance imaging of the brains of patients D304G and D366E revealed no gross neuroanatomical abnormalities, and extensive metabolic testing in each patient did not reveal any underlying metabolic abnormalities. Developmental regression and seizures are absent in all cases, but electroencephalogram (EEG) revealed background slowing and intermittent high-amplitude, low-frequency spiking activity in each case. Strikingly, the electroencephalographic disturbance was also graded, and the amplitude of spiking activity correlated with the severity of developmental delay (i.e., I368T > D366E). Two of these patients, D366E and I368T, underwent visual evoked potential recording, which demonstrated abnormally prolonged latency in both cases. Behavioral phenotypes also vary in type and severity, with two of these patients (D304G and I368T) exhibiting frequent agitation and self-injurious behavior. These cases highlight the phenotypic variability of syt1-associated neurodevelopmental disorder, with patient D366E demonstrating a substantially milder global phenotype than patients D304G and I368T.

***Crystal structures of syt1 C2B domains harboring pathogenic mutations***

We first undertook a structural analysis to define the molecular phenotype associated with these three mutations, all of which occur in the cytoplasmic C2B domain of this tandem-C2 domain protein (**Figure 1A**). X-ray crystallographic structures of the $Ca^{2+}$-binding region in *apo*-syt1 C2B variants are shown in **Fig. 1B**. Compared with the wild-type domain, each mutant variant C2B is correctly folded in the canonical $\beta$-sandwich of a C2 domain (**Fig. 1B**). While subtle differences in the position of $Ca^{2+}$-binding/membrane-penetration loops were apparent (**Fig. 1B**), these residues are likely to be highly mobile in solution, and the observed differences are likely attributable to differences in crystal packing. **Fig. 1** also highlights the physicochemical diversity of these mutations. D304G neutralizes a $Ca^{2+}$-binding aspartic acid and confers a +2 charge on the $Ca^{2+}$-binding pocket. D366E preserves a carboxylate ligand but shrinks the $Ca^{2+}$-binding pocket (**Fig. 1B**). I368T substitutes a polar threonine for a bulky, hydrophobic isoleucine that normally penetrates the plasma membrane upon $Ca^{2+}$ binding by syt1 (Bai et al., 2002). As other authors have emphasized (Baker et al., 2018), the affected residues are highly conserved in syt1 homologs across the metazoan phylogeny.

***Disease-associated syt1 variants traffic normally but fail to support synaptic transmission***

Each disease-associated mutation occurs at a residue with a defined function in the loops of C2B (Chang et al., 2018; Evans et al., 2015b; Hui et al., 2009b). However, studies of synaptic transmission in neurons expressing syt1 with C2B loop mutations have only rarely examined single point mutations, and mutations at some of these sites appear inconsequential (Mackler et al., 2002; Nishiki and Augustine, 2004). While limited evidence points to deficits in vesicular recycling of disease-associated syt1 variants (Baker et al., 2018), neurotransmission in neurons expressing these variants has not been assessed. We thus assessed the trafficking and synaptic function of each variant using immunocytochemistry and electrophysiological recordings of synaptic currents using cultured mouse hippocampal and cortical neurons (**Fig. 2**; please note: in these and all subsequent experiments, amino acid numbers for the rat and mouse syt1 sequences are used). Using a specific, KO-validated monoclonal antibody against syt1

(**Appendix - Fig. S2**), we found that each mutant variant trafficked as effectively as WT to the presynaptic compartment (**Fig. 2A-B**). Next, we measured evoked GABAergic postsynaptic currents (IPSCs) from WT or syt1 KO cortical neurons expressing mutant syt1 variants (**Fig. 2C**). Despite localizing correctly to presynaptic terminals, mutant syt1 variants largely failed to support evoked synaptic transmission (**Fig. 2D-G**). However, this effect was graded: while the evoked-transmission phenotypes of D303G and I367T appeared nearly identical to the syt1 KO (**Fig. 2D-G**), D365E preserved the rapid kinetics of wild-type syt1 (**Fig. 2E,H)**, despite also exhibiting the low amplitude and total charge transfer properties of the KO (**Fig. 2F-G**).

Syt1 also regulates spontaneous neurotransmitter release by suppressing, or clamping, fusion under resting conditions (Courtney et al., 2019; Liu et al., 2009). We observed that clamping of spontaneous vesicle fusion, as represented by the frequency of miniature IPSCs (mIPSCs), also varied among the genotypes, with partial rescue by I367T and D365E (**Fig. 2I**), consistent with an established but poorly-understood role for $Ca^{2+}$-binding loops in the clamping action of syt1 (Evans et al., 2015b; Lee et al., 2013). In summary, the pathogenic syt1 mutations affect spontaneous release rates and strongly impact evoked release. Importantly, and in correlation with the observed clinical phenotypes, D303G and I367T cause an even more severe impairment of evoked synaptic release than D365E.

***Disease-associated syt1 variants exhibit a graded dominant-negative impact on neurotransmitter release***

We next assessed the dominant-negative potency of each mutation with simultaneous lentiviral expression of mutant and WT syt1, in combination with optical imaging of evoked glutamate release (**Fig. 3**) (Marvin et al., 2013). Hippocampal neurons cultured from $SYT1^{fl/fl}$ mice were transduced with lentivirus encoding Cre recombinase along with separate lentiviruses encoding WT and mutant syt1, respectively (**Fig. 3A-B**). In each experiment the WT and mutant syt1 expression levels obtained using each dose of lentivirus were measured in separate, parallel samples by immunoblot analysis (**Fig 3A-B**). A range of WT:mutant expression ratios was assessed, and evoked glutamate release was measured as the

normalized change in fluorescence across a field of view in response to a 10-AP, 10-Hz field stimulus (**Fig. 3C-H**). iGluSNFR fluorescence transient amplitudes were plotted against the relative expression of WT and mutant protein in **Fig**. **3E**, clearly demonstrating a dominant-negative action of each mutant syt1 variant. Even at sub-stoichiometric expression levels, mutant variants dose-dependently inhibited action-potential-evoked glutamate release (**Fig. 3E**). Strikingly, we observed a graded dominant-negative potency (D303G ≈ I367T > D365E) that again correlated with the observed clinical phenotypes (**Fig. 3E-F**). As a relative measure of synaptic release probability, we also measured the amplitude of the tenth iGluSNFR transient normalized to that of the first transient ($dF/F_0$(tenth/first)) (**Fig. 3G-H**). As expected, $dF/F_0$(tenth/first) increased with the expression of mutant protein, indicating a dose-dependent reduction in relative release probability (**Fig. 3G**). As with the amplitude of the first response, mutant syt1 variants exhibited graded, dominant-negative activity, with D365E expressing the mildest phenotype (**Fig. 3G-H**). Together, these results unambiguously establish the dominant-negative action of each mutant variant and strongly suggest a physiologic basis for the phenotypic heterogeneity observed in these patients.

***Disease-associated syt1 variants show impaired binding to $Ca^{2+}$ and lipids***

Syt1 triggers SNARE-catalyzed membrane fusion *in vitro* and at neuronal synapses by $Ca^{2+}$-dependent membrane insertion of residues in two flexible loops in both C2A and C2B (Bai et al., 2016b; Courtney et al., 2019; Evans et al., 2015b; Liu et al., 2014; Tucker, 2004). This interaction requires negatively-charged phospholipids, namely phosphatidylserine (PS) and/or phosphatidylinositol(4,5)-bisphosphate ($PIP_2$) (Wang et al., 2011b). $PIP_2$, in particular, is a dynamically-regulated phospholipid (Micheva et al., 2001b) that plays an important role in exocytosis (Eberhard et al., 1990b). Importantly, syt1 can bind and partially penetrate $PIP_2$-containing membranes even in the absence of $Ca^{2+}$, allowing for enhanced kinetics of $Ca^{2+}$-dependent membrane penetration (Jihong Bai et al., 2004; Bradberry et al., 2019).

We thus performed a series of studies with purified protein and liposomes to define how mutant syt1 variants interact with $Ca^{2+}$ and membranes (**Fig. 4**). In saturating [$Ca^{2+}$] (1 mM), the purified tandem

C2 domains (C2AB) of each syt1 variant displayed largely intact $Ca^{2+}$-dependent and -independent binding to phospholipid bilayers containing PS with or without $PIP_2$ (**Fig. 4A-C**). However, each mutant variant showed diminished binding to bilayers containing $PIP_2$ as the sole acidic phospholipid, consistent with an established role for C2B as the primary $PIP_2$-binding domain of syt1 (**Fig. 4A-C**) (Jihong Bai et al., 2004). A detailed titration of $[Ca^{2+}]$ in the presence of PS:$PIP_2$ vesicles demonstrated a substantial reduction in the $Ca^{2+}$-sensitivity of membrane binding for each mutant variant (**Fig. 4D-E**). This effect was graded in a fashion that correlated with the severity of both the synaptic and human phenotypes for each mutation (**Fig. 4E**). In particular, at 10 μM $Ca^{2+}$, a relevant $Ca^{2+}$ concentration at release sites during action potential firing in cultured hippocampal neurons (Burgalossi et al., 2010), D365E exhibited substantially more $Ca^{2+}$-dependent binding than either D303G or I367T (**Fig. 4E**). t-SNARE binding, by comparison, was largely unaffected by each mutation in both the presence and absence of saturating $[Ca^{2+}]_{free}$ (**Appendix - Fig. S3**).

To assess the stability of the syt1 C2AB-$Ca^{2+}$-phospholipid complex formed by WT and mutant protein, we performed a time-resolved assay to measure the kinetics of $Ca^{2+}$ release from this complex (**Fig. 4F-H**) (Nalefski et al., 2001). In this assay, the fluorescent $Ca^{2+}$ chelator quin-2 is rapidly mixed with pre-assembled C2AB-$Ca^{2+}$-phospholipid complexes in a stopped-flow fluorescence spectrometer, and observable kinetic information corresponds to liberation of $Ca^{2+}$ from the protein-lipid complex (**Appendix - Fig. S4**). We observed that $Ca^{2+}$ release was more rapid in complexes containing mutant C2AB (**Fig. 4G-H**). Fitting of double exponential decay functions to the observed data revealed a fast and a slow component for each trace (**Fig. 4H**). WT protein exhibited a more predominant slow component of $Ca^{2+}$ release (**Fig. 4H**), indicating that in the activated, membrane-bound state, WT syt1 forms more stable complexes with $Ca^{2+}$ as compared to the three mutant proteins.

***Disease-associated mutations impair high-affinity $Ca^{2+}$-dependent membrane penetration by C2B and define cooperativity between C2A and C2B***

Thus far, all disease-causing syt1 mutations occur in the C2B domain of the protein (Baker et al., 2018), and a host of studies have found that syt1 is more functionally susceptible to mutations in C2B than in C2A (Edwin R. Chapman, 2008; Shin et al., 2009). However, the biophysical basis for this C2B-dependence remains unclear, as C2A has an equal number of $Ca^{2+}$-binding residues and binds at least as many $Ca^{2+}$ ions (Fernandez et al., 2001; Shao et al., 1998; Sutton et al., 1995). Moreover, studies using the individual C2 domains are difficult to meaningfully interpret, as significant evidence exists for a functional linkage between the two domains (Bai et al., 2002; Courtney et al., 2019; Evans et al., 2016; Herrick et al., 2006).

To better delineate the roles of C2A and C2B, we developed an assay to carefully assess membrane penetration by either domain in the context of the tandem domains (**Fig. 5**). Purified syt1 C2AB was first labeled at introduced cysteine residues with an environmentally-sensitive probe, NBD, on a $Ca^{2+}$-binding/membrane penetration loop in C2A (F234C-NBD) or C2B (I367C-NBD). This dye undergoes a blue shift and substantial emission intensity increase when buried in the hydrophobic bilayer (**Fig. 5B**). We emphasize that only bulky, hydrophobic residues (F234, V304) were replaced with cysteine labels. Labeled syt1 was then combined with $PIP_2$-containing vesicles such that NBD-syt1 was completely adsorbed to the surface of the liposomes even in the absence (<10 nM) of free $Ca^{2+}$ (**Appendix - Fig. S5**). Under these conditions, the $Ca^{2+}$-dependent membrane penetration activities of C2A and C2B can be examined independently, as avidity effects (i.e., apparent coupling of penetration by C2A and C2B due to an entropic benefit of one domain following binding by the other) are largely avoided.

Changes in NBD fluorescence, while titrating $Ca^{2+}$ in samples containing WT or mutant syt1 C2AB, are depicted in **Fig. 5B-C**. Two important features emerge from these data: first, in WT syt1, C2B exhibits a substantially higher sensitivity to $Ca^{2+}$ than C2A. Second, each mutation reduces the $Ca^{2+}$-sensitivity of membrane penetration by both C2A and C2B, though with a more pronounced effect on C2B (**Fig. 5C-D**). These results demonstrate that, in WT syt1, $Ca^{2+}$ binds more tightly to C2B than C2A at the protein-membrane interface, implying that more free energy is liberated by $Ca^{2+}$-triggered

penetration by C2B ($\Delta G = RT \ln K$). For each mutant variant, this high-affinity mode is abolished in a graded fashion, and the $Ca^{2+}$-dependence of membrane penetration by C2B more closely resembles that of C2A (**Fig. 5C,D**). As with our previous studies, this effect was graded, with D303G having the most potent effect on membrane penetration (**Fig. 5B-C**). Each mutant also showed a reduction in the $Ca^{2+}$ sensitivity of penetration by C2A (**Fig. 5D-E**), consistent with reports of functional cooperativity between C2A and C2B when linked (Bai et al., 2002; Courtney et al., 2019; Evans et al., 2016; Herrick et al., 2006). Together, these data establish a biophysical basis for the functional dominance of syt1's C2B domain and, in turn, the clustering of disease-causing mutations in this region of the protein (**Fig. 5F**).

***Rescue of dominant-negative synaptic impairments by the clinically-approved drug 4-aminopyridine***

Even when a molecular cause is well-defined, treatment of inherited developmental disorders is a challenging prospect given the paucity of suitable gene therapies. However, depending on the consequences of a given mutation, rationally guided medical or surgical treatment may benefit some patients. Because each mutation described here reduces the $Ca^{2+}$ sensitivity of membrane binding and penetration by syt1, we reasoned that interventions to boost presynaptic $Ca^{2+}$ influx might mitigate the synaptic deficits associated with each mutant. 4-aminopyridine (4-AP, fampridine, dalfampridine) (**Fig. 6A**) is a $K^+$ channel antagonist clinically approved for the treatment of walking symptoms in multiple sclerosis (Leussink et al., 2018). This drug, which is selective for $K_v3$ channels at low concentrations (Alle et al., 2011), would be expected to broaden action potentials and thus enhance presynaptic $Ca^{2+}$ influx. In neurons transduced to express roughly equal amounts of mutant and WT syt1, 4-AP dose-dependently enhanced evoked glutamate release and restored normal short-term plasticity over the course of the stimulus train (**Fig. 6B-D**). At 5 μM, the dominant-negative effects of each mutant on the amplitude of the first glutamate transient (**Fig. 6C**), as well as $dF/F_0$(tenth/first) (**Fig. 6D**), were largely mitigated, and responses appeared similar to those of WT neurons in the absence of drug. We emphasize that additional considerations apply in the clinical setting, particularly given the convulsant effects of higher doses of 4-AP. However, these results—particularly given the lack of epilepsy in patients with syt1

mutations—suggest that 4-AP or other centrally-acting $K_v$ channel blockade presents a plausible approach to pharmacotherapy for these patients.

## Discussion

*De novo* mutations in synaptotagmin-1 have been associated with a severe neurodevelopmental syndrome (Baker et al., 2018, 2015). In this study, we provide the first evidence that these mutant variants can cause disease by impairing synaptic transmission in a dominant-negative, but also graded, manner. We extend these findings to define key mechanistic insights into the action of syt1, and we provide a plausible basis for pharmacotherapy of syt1-associated neurodevelopmental disorder.

### *Dominant-negative potency and genotype-phenotype correlation in mutant syt1 variants*

Each of the mutant variants studied here alters the physicochemical properties of the $Ca^{2+}$-binding, membrane-penetrating loops of syt1 C2B while preserving the overall fold of this domain. We found that each disease-associated mutation studied here had a dramatic and deleterious impact on synaptic transmission, as shown in our whole-cell voltage clamp studies (**Fig. 2**). Even the most conservative mutation, D366E, caused near-complete loss of function in syt1 despite previous studies suggesting that a neutralizing mutation (D>N) at this position should have only mild effects (Nishiki and Augustine, 2004). Our results demonstrate that the $Ca^{2+}$-binding pocket of syt1 C2B is exquisitely tuned, highlighting the difficulty of predicting a mutation's functional impact based on biochemical principles alone. Moreover, our observations strongly suggest that these mutant syt1 variants likely provide little support for synaptic transmission *in vivo*, supporting a role for these mutations in the observed clinical phenotypes.

An unambiguous causal role for these mutations, however, requires a capacity for mutant syt1 to act in a dominant-negative manner. Previous studies have suggested that human syt1 mutant variants undergo impaired vesicular recycling (Baker et al., 2018), and unrelated heterozygous mutations in *Drosophila* syt1 have been shown to impair neurotransmitter release (Mackler et al., 2002). The current study, by contrast, is the first to quantitatively assess how disease-associated syt1 variants can disrupt

neurotransmitter release when expressed alongside WT protein (**Fig. 3**). Our findings unequivocally demonstrate the capacity for these heterozygous mutations to cause profound impairment of neurotransmitter release (**Fig. 3**). Moreover, this work provides strong evidence for a graded potency of disease-associated syt1 variants, with D365E exhibiting a markedly less severe dominant-negative phenotype *versus* D303G and I367T (**Fig. 3**). We note that substantial phenotypic heterogeneity is also observed for each given genotype (Baker et al., 2018), suggesting that allelic expressivity also plays an important role in determining disease severity. However, when controlling for allelic expression ratio, the human D366E variant can be expected to produce a less severe clinical phenotype than either D304G or I368T—as observed in the limited number of mutation-bearing patients described so far (Baker et al., 2018).

Our biochemical (**Fig. 4**) and spectroscopic (**Fig. 5**) studies establish that this graded effect on synaptic physiology (**Figs. 2,3**) corresponds well to a graded impact on $Ca^{2+}$-dependent binding and penetration of membranes by syt1. Across these studies, variants D365E and I367T were more evenly matched, with a trend toward more severe impairment in I368T (**Figs. 4,5**). In comparison, variant D303G, which is associated with the most severe human phenotype (Baker et al., 2018) and showed the most substantial impairment of synaptic release at low mutant:WT expression ratios (**Fig. 3**), also exhibited the most severe biophysical impairments. These results thus provide strong support for a mechanism of action of syt1 that specifically involves $Ca^{2+}$-dependent penetration of the plasma membrane to trigger synaptic vesicle fusion (Bai et al., 2016b; Evans et al., 2015b; Liu et al., 2014). Further studies may define whether these mutations also impact other roles for syt1, such as SV-plasma membrane docking (Chang et al., 2018; Liu et al., 2009).

***Functional segregation and cooperative interactions between the tandem C2 domains of syt1***

Our membrane penetration studies (**Fig. 5**) also reveal several interesting features of a prototypical $Ca^{2+}$-dependent protein-lipid interaction involving tandem protein domains. By adsorbing syt1 C2AB to the lipid bilayer prior to the addition of free $Ca^{2+}$, our approach allowed for a rigorous

assessment of membrane-penetration activity for each domain in the tethered pair (**Fig. 5, Appendix - Fig. S5**). To our surprise, the $Ca^{2+}$ responses of C2A and C2B were distinct in WT syt1, with C2B exhibiting a higher-affinity mode of $Ca^{2+}$-dependent membrane penetration (**Fig. 5**). While the basis for the higher $Ca^{2+}$ sensitivity of C2B is not clear, this effect is likely due to the substantial cooperativity between $Ca^{2+}$- and $PIP_2$-binding activities of syt1 C2B (Jihong Bai et al., 2004; Li et al., 2006; van den Bogaart et al., 2012). Indeed, each disease-associated mutation inhibited $Ca^{2+}$-dependent membrane penetration (**Fig. 5**) and dramatically disrupted $Ca^{2+}$-dependent binding to $PIP_2$ (**Fig. 4**). Thus, in addition to binding a polybasic patch on the side of C2B and juxtaposing the cytoplasmic domain of syt1 with the target membrane (Jihong Bai et al., 2004), $PIP_2$ may directly interact with the $Ca^{2+}$-binding, membrane-inserting residues of C2B. This interpretation is supported by the capacity of $PIP_2$ to drive $Ca^{2+}$-independent membrane penetration by syt1 (Bradberry et al., 2019). Further studies will help define a structural picture of how syt1 binds $PIP_2$ in concert with $Ca^{2+}$ to promote SV fusion.

An unresolved question regarding the mechanism of action for syt1 concerns the differential sensitivity of its C2-domains to mutations. While mutations in C2A are often well-tolerated (Stevens and Sullivan, 2003), mutations in C2B readily disrupt the function of this protein (Mackler et al., 2002), as evidenced by the clustering of disease-associated mutations in C2B (Baker et al., 2018). The higher $Ca^{2+}$ sensitivity of membrane penetration by C2B (**Fig. 5**) implies that penetration by this domain liberates more free energy than penetration by C2A and suggests a biochemical basis for the sensitivity of mutations in C2B. This high $Ca^{2+}$ sensitivity may also be critical for the role of C2B in dynamic, $Ca^{2+}$-dependent docking of synaptic vesicles (Chang et al., 2018). C2A, by contrast, penetrates the membrane with a lower $Ca^{2+}$ sensitivity than C2B (**Fig. 5**). This may serve to enable a wider dynamic range of $Ca^{2+}$ sensitivity for syt1-triggered membrane fusion, which is sensitive to changes in $[Ca^{2+}]_i$ across a range of $[Ca^{2+}]_i$ spanning orders of magnitude (Burgalossi et al., 2010; Neher and Sakaba, 2008; Stevens and Sullivan, 2003).

A closely related problem is the question of how and whether C2A and C2B exhibit cooperativity in terms of $Ca^{2+}$-dependent membrane binding activity. Several previous studies have suggested a

functional link between the two domains that depends on their relative orientations (Bai et al., 2016b, 2002; Evans et al., 2016; Herrick et al., 2006; Liu et al., 2014; Tran et al., 2019). However, these studies have not addressed $Ca^{2+}$ cooperativity *per se*, i.e., does $Ca^{2+}$ and lipid binding by one domain drive $Ca^{2+}$ and lipid binding by the other domain? Our penetration studies, which rigorously address this problem by pre-tethering syt1 C2AB to the membrane surface, formally establish a cooperative action between C2A and C2B by demonstrating that each mutation in C2B reduces the $Ca^{2+}$ sensitivity of penetration by C2A (**Fig. 5**). Our data help establish a clear mechanistic picture for how $Ca^{2+}$ activates syt1: C2B, by binding $PIP_2$ and penetrating the membrane with high $Ca^{2+}$ sensitivity, drives the adjacent C2A to likewise bind $Ca^{2+}$ and penetrate the membrane to increase release probability (Courtney et al., 2019). The interactions underlying this cooperativity are unclear but likely involve changes in the membrane-water interface that occur with penetration of the membrane by each C2 domain.

***Molecular correlates of synaptic $Ca^{2+}$ cooperativity***

Another critical but poorly understood cooperative relationship is the logarithmic dependence of synaptic vesicle fusion rate on $[Ca^{2+}]_i$ (Dodge and Rahamimoff, 1967; Neher and Sakaba, 2008). Because syt1 binds 4-5 $Ca^{2+}$ ions (Brose et al., 1992b; Fernandez et al., 2001; Shao et al., 1996), this stoichiometric relationship has long been proposed to mediate the $Ca^{2+}$ dependence of synaptic release (Brose et al., 1992b). However, in a number of studies, including data reported here, the $Ca^{2+}$-dependent membrane binding and penetration by syt1 exhibits a far shallower dependence on $Ca^{2+}$ (Brose et al., 1992b; Evans et al., 2016; Gaffaney et al., 2008; Tran et al., 2019; van den Bogaart et al., 2012) (**Fig. 4, Fig. 5**). In particular, the present study demonstrates this relatively low degree of $Ca^{2+}$ cooperativity using two different assays of $Ca^{2+}$-dependent syt-membrane interaction (**Fig. 4, Fig. 5**). The high $Ca^{2+}$ cooperativity of release but low $Ca^{2+}$ cooperativity of membrane penetration by syt1 can be readily reconciled by the participation of multiple copies of syt1 in the membrane fusion reaction. Our finding that disease-associated syt1 variants potently disrupt the function of WT syt1 at sub-stoichiometric expression ratios, particularly for variant D303G (**Fig. 3**), supports this notion. Further studies, combining

accurate syt1 copy number measurements *in situ* with more rigorous measurements of vesicle release rates, may better define a role for syt1 in the $Ca^{2+}$ cooperativity of neurotransmitter release.

***Pharmacologic strategies for treatment of syt1-associated neurodevelopmental disorder***

Finally, our mechanistic studies culminated in the discovery that 4-aminopyridine, a drug that is approved for clinical use (Leussink et al., 2018), may help to mitigate the synaptic deficits in syt1-associated neurodevelopmental disorder (**Fig. 6**). In patients with more severe phenotypes (D304G and I368T, in this series), treatment targets may include agitation and self-injurious behavior. In patients with less severe phenotypes (D366E in this series), treatment targets may include improved attention and learning ability. The concentrations used in this study are higher than, but within fivefold, of typical serum concentrations achieved with standard doses of 4-AP (Bever et al., 1994), and even a partial recovery of presynaptic function may allow for functional improvement in these patients. Importantly, the concentrations of 4-AP studied here are several orders of magnitude lower than those expected to cause cardiotoxicity (Renganathan et al., 2009). We also emphasize that, given the importance of brain developmental processes, any pharmacologic intervention is unlikely to cause complete functional recovery, though this may also depend on the age at which such interventions are initiated. Regardless, given the lack of other viable and specific treatment options, centrally acting $K_v$ blockade by 4-AP appears to be a rational, plausible option for treatment of patients with this profound neurodevelopmental disorder.

**Methods**

***Experimental model and subject details*** All neuronal cultures were prepared from early postnatal (P0-P1) mouse pups in accordance with all relevant regulations and with the approval of the University of Wisconsin Institutional Animal Care and Use Committee. For electrophysiologic studies (Fig. 2), pups from $syt1^{+/-}$ breeders (Jackson Labs stock # 002478) were used; for imaging studies (Figs. 2, 3, 6), pups from $syt1^{fl/fl}$ breeders (Quadros et al., 2017) were used. Clinical histories for patients harboring syt1

variants D304G and D366E were obtained through interviews with the parents of these patients and through standard record request protocols. All procedures were performed with the approval of the University of Wisconsin Health Sciences Institutional Review Board.

***Patient genotyping*** Sanger sequencing (Functional Biosciences, Madison, WI) was performed following extraction of genomic DNA from saliva samples (Oragene collection kit and Prep-IT L2P reagent, both from DNA Genotek) using the primers: gcaagagaaattgggtgatatctgcttctccc (D303G, forward); cgcagcatgtgcgccatgc (D303G, reverse); gggccttatctctagagctagatgattcatattcatttcatggc (D365E, forward); cttcttgacggccagcatggcatc (D365E, reverse).

***Protein purification and labeling*** The cDNA encoding human syt1 C2B (amino acids 272-422) was cloned into a pET-based expression vector that included a His6-tagged maltose binding protein and a tobacco etch virus protease (TEV) restriction site. Site-directed mutagenesis (Stratagene QuikChange) of syt1 C2B was performed to make three single-point mutant constructs. All mutations were confirmed by DNA sequencing. Plasmids containing the recombinant C2B domains were transformed into BL21(DE3) *E. coli*, which were grown in Terrific Broth and induced with IPTG for protein production. The cell pellets were frozen at -80 °C and stored until needed. Cells were thawed in lysis buffer [20 mM HEPES (pH 7.4), 150 mM NaCl], lysed using a Microfluidizer, and clarified by centrifugation using a Beckman JA-20 rotor at 19,500 rpm (45,900 g) for 45 min. The supernatant was passed through a Ni-NTA affinity column which was equilibrated with lysis buffer. The column then was washed with 150 ml lysis buffer, followed by a wash in lysis buffer plus 30 mM imidazole. Finally, $His_6$-MBP-C2B was eluted with 80 ml lysis buffer including 300 mM imidazole. The resulting fusion protein was cleaved with TEV protease overnight at 4°C. Next, an SP-Sepharose column was used to separate the C2B domain from MBP, TEV protease, and uncleaved fusion proteins. Elution from the cation exchange column was done with a 0 to 1 M NaCl gradient and the solution containing the protein of interest was concentrated and loaded onto a Superdex 75 column to remove the remaining contaminants. Purity was assessed using SDS-PAGE Stain-Free gels from BioRad, and protein concentrations were quantified by $OD_{280}$ using each protein's

calculated extinction coefficient. For membrane binding and penetration studies, WT and mutant rat syt1 C2AB (residues 96-421), with or without cysteines introduced for labeling, were purified as glutathione-S-transferase fusion constructs (pGEX4T-1 vector, GE healthcare) and eluted by thrombin cleavage as described previously (Bradberry et al., 2019). Labeling was performed using IANBD-amide followed by desalting with size-exclusion chromatography, also as described previously (Bradberry et al., 2019). For SNARE binding assays, HaloTag-syt1 C2AB and the syntaxin1A/SNAP-25B t-SNARE heterodimer were expressed as N-terminal $his_6$ fusion constructs (pTrcHis vector, Thermo), purified by immobilized metal affinity chromatography, and eluted with imidazole as described previously (Bradberry et al., 2019; Courtney et al., 2018b).

***Crystallization and data collection*** The WT syt1 C2B domain was crystallized in 0.2 M ammonium sulfate (pH 6.0), 30% PEG3350 (pH 6.0); the D304G mutant was crystallized in 2.0 M ammonium sulfate (pH: 4.6), 0.1 M sodium acetate; the D366E mutant was crystallized in 1.6 M ammonium sulfate (pH 4.0), 0.1 M citrate; and the I368T mutant was crystallized in 1.5 M ammonium sulfate (pH range: 4.5-4.8), 0.1 M sodium acetate. All crystals were grown at 20 °C using the hanging droplet method with purified protein at a stock concentration of 20 mg/ml. The crystals were captured into nylon loops and frozen in liquid $N_2$. Initial data sets were collected on a Rigaku ScreenMachine. High resolution data sets were collected at SLAC beamline 7-1. The wavelength of each dataset were wild type 1.097 Å, D304G 0.984 Å, D366E 0.9795 Å, and I368T 1.099 Å and the data were collected at 90 K. X-ray data were processed and scaled using XIA2 (Evans, 2006; Kabsch, 2010; Winn et al., 2011; Winter, 2010; Winter et al., 2018). The X-ray crystal structure was solved using molecular replacement techniques (Phaser) (McCoy et al., 2007) and subsequently refined using Phenix (Adams et al., 2010).

***Cell culture and lentiviral transduction*** Briefly, cortices (syt1 WT/KO, data in fig. 2) or hippocampal formations ($syt1^{fl/fl}$, data in Fig. 3) were obtained by microdissection and kept in Hibernate-A until the completion of dissection, at which point they were incubated with trypsin-EDTA (Corning, 0.25%) for 30 minutes at 37 ºC with periodic agitation. Trypsin was then replaced with plating medium (DMEM +10%

FBS) and tissue was triturated 10-20 times with a 1 ml pipette before plating at ~100,000 cells/cm$^2$ onto poly-D-lysine coated glass coverslips. Plating medium was replaced with complete growth medium (Neurobasal-A medium supplemented with B-27 (1X, Gibco) and Glutamax (1X, Gibco) after 1 hour. For imaging experiments, lentivirus encoding Cre recombinase under the control of a synapsin promoter and lentivirus encoding a modified iGluSNFR construct were added to cultures at 0-2DIV. Lentivirus encoding WT or mutant syt1 variants was added at 5-7DIV.

***Molecular biology and lentiviral preparation*** For lentiviral constructs, DNA sequences encoding WT syt1 or mutant variants generated by site-directed mutagenesis (QuikChange Lightning, Agilent) were subcloned into the FUGW lentiviral transfer plasmid (Addgene plasmid #14883, a gift from Dr. David Baltimore) modified to include the human synapsin promoter and an internal ribosome entry sequence followed by the red fluorescent protein mRuby3. A lentiviral transfer plasmid encoding Cre recombinase under the control of the human synapsin promoter was used in experiments with syt1$^{fl/fl}$ neurons (Addgene plasmid #86641, a gift from Dr. Fan Wang). Lentivirus was generated by $CaPO_4$-mediated cotransfection of HEK293-T cells with transfer plasmid and the helper plasmids pCD/NL-BH*ΔΔΔ (Addgene plasmid #17531, a gift from Dr. Jakob Reiser) and pLTR-G (Addgene plasmid #17532, a gift from Dr. Jakob Reiser) followed by concentration of virus-bearing supernatant by ultracentrifugation as described (Kutner et al., 2009). iGluSNFR (Addgene plasmid # 41732, a gift from Dr. Loren Looger) was modified to remove the final four amino acids and include a Golgi export sequence (Parmar et al., 2014) and ER exit motif (Stockklausner et al., 2001). This construct was subcloned into the FUGW lentiviral transfer plasmid modified to include the CamKIIα promoter.

***Immunocytochemistry and confocal microscopy*** At 14-16 DIV, coverslips of hippocampal neurons from syt1$^{fl/fl}$ mice expressing WT or mutant variant syt1 were rinsed 2-3 times with phosphate-buffered saline (PBS) and fixed by incubation with pre-warmed 4% paraformaldehyde for 10 minutes at 37 ºC. Cells were washed in PBS, incubated for 10 minutes in PBS containing 0.2% saponin and 50 mM Tris-HCl pH 8.0, washed in PBS, and blocked for 1 hour at room temperature in PBS containing 5% normal goat

serum, 5% BSA, and 0.02% saponin. Coverslips were then incubated with primary antibodies against syt1 (mouse mAb 48 (Matthew et al., 1981), 1:250 dilution of a 3.7 mg/ml purified stock) and synaptophysin (guinea pig pAb, Synaptic Systems, 1:250 dilution of a 1 mg/ml stock) in PBS containing 1% BSA and 0.02% saponin at 4ºC overnight. Coverslips were washed in PBS containing 0.02% saponin and incubated with fluorescent secondary antibodies (AlexaFluor488 conjugated goat anti-guinea pig IgG and AlexaFluor647 conjugated goat anti-mouse IgG2b) for 1 hour at room temperature. Cells were then washed in PBS containing 0.02% saponin, followed by PBS without saponin, and mounted on glass slides. Fixed, stained slides were later imaged on a Zeiss LSM 880 confocal microscope equipped with a 40x 1.3NA oil objective with identical laser power and gain settings used for all experiments. Replicates represent single fields of view from at least 2 separate dissections.

***Immunoblotting*** Coverslips of neurons (14-18 DIV) from syt1$^{fl/fl}$ mice expressing WT or mutant syt1 variants were rinsed 2-3 times in PBS and lysed by repeated pipetting of 150 µl lysis buffer (50 mM Tris pH 8.0, 150 mM NaCl, 2% SDS, 0.1% Triton X-100, 10 mM EDTA) containing protease inhibitors (cOmplete mini EDTA-free, Roche, 1 tablet / 10 ml lysis buffer). These samples were combined with 50 µl 4X Laemmli sample buffer, heated to 70 ºC for 10 minutes, and stored at -20 ºC until use. For each experiment, samples were subjected to SDS-PAGE, transferred to PVDF membrane, blocked in Tris-buffered saline containing 0.1% Tween-20 (TBS-T) with 5% milk, and blotted using an anti-syt1 antibody (mAb 48 (Matthew et al., 1981), 1:500 dilution of hybridoma supernatant (Developmental Studies Hybridoma Bank)) in TBS-T with 1% milk at 4 ºC overnight. After washing in TBS-T, blots were incubated with HRP-conjugated goat anti-mouse IgG2b 2º antibody (Invitrogen) in TBS-T for 1 hr at room temperature, washed in TBS-T, and imaged with a CCD gel imaging device (GE). Equal protein loading across lanes was confirmed by Coomassie staining gels after transfer.

***Electrophysiology*** Whole-cell voltage-clamp recordings of cultured neurons (13-14DIV) were performed at room temperature in a bath containing (in mM): 128 NaCl, 5 KCl, 1 $MgCl_2$, 2 $CaCl_2$ 25 HEPES-NaOH, 30 glucose) using patch pipettes pulled from borosilicate glass (Sutter instruments, 1.5 mm OD, 1.1 mm

ID, 3-5 MOhm) with an internal solution containing (in mM): 130 KCl, 1 EGTA, 10 HEPES-NaOH, 2 ATP (Mg salt), 0.3 GTP (Na salt), 5 phosphocreatine (Na salt). Recordings were performed using a MultiClamp 700B combined amplifier and digitizer (Molecular Devices) under the control of Clampex 10 software (Molecular Devices). $GABA_A$-mediated currents were isolated using CNQX (20 μM) and APV (50 μM); for mIPSC recordings, 1 μM TTX was included in the bath. Neurons were held at -70 mV in all experiments without correction for liquid junction potentials. Series resistance was monitored and recordings were discarded if this quantity rose above 15 MOhms. For evoked recordings, a concentric bipolar electrode (FHC, 125/50 um extended tip) was placed 100-200 um away from the patched soma and stimulation currents were adjusted evoke maximal responses. For mIPSC recordings, sixty seconds of data were recorded for each cell. mIPSCs were quantified for each recording using a template-matching algorithm in Clampfit (Molecular Devices). Each replicate represents an individual cell from at least 2 separate dissections.

***Glutamate imaging*** All experiments were performed at room temperature. Imaging bath solution contained (in mM): 128 NaCl, 2.5 KCl, 1 $MgCl_2$, 2 $CaCl_2$, 25 HEPES-NaOH, 30 glucose; complete blockade of synaptic currents achieved using CNQX (20 μM), APV (50 μM), and picrotoxin (50 μM). Coverslips were mounted in a field stimulus chamber (RC-49MFSH, Warner Instruments) and imaged on a motorized inverted epifluorescence microscope (Olympus IX81) equipped with a 60x, 1.45 NA oil immersion objective (Olympus) and standard GFP filter set (49002, Chroma). Illumination was provided with a 470 nm LED (Thorlabs) and fluorescence was detected on the central quadrant of an sCMOS camera (OrcaFLASH V2.0, Hamamatsu) operated in 4x4 binning mode (256 x 256 pixels, 111 x 111 μm field of view) using a 10 ms exposure time. The optical setup was controlled using Micro-Manager (Edelstein et al., 2010), with LED intensity controlled using a USB DAQ (National Instruments). Stimulus control was accomplished using the input/output section of a HEKA EPC 10 combined amplifier and digitizer connected to the timing input of the sCMOS camera and controlled with PatchMaster software (HEKA). Stimuli (100 V, 0.5 ms) were delivered using a stimulation box (Grass

SX88). For each coverslip, responses to 10-AP, 10-Hz stimulus trains were acquired with at least 4 minutes of rest in between acquisitions. $dF/F_0$ was calculated for the whole field of view to normalize for the amount of sensor present, with baseline subtraction determined using a dark area of the coverslip. For experiments involving 4-AP treatment, the microscope was equipped with a motorized XY stage (Mad City Labs) and the same fields of view were imaged in control and 4-AP conditions. Conversion of raw fluorescence to $dF/F_0$ was performed using a custom-written R script. Replicates were defined as average traces for a whole coverslip (Fig. 3) or fields of view (Fig. 6) across 2-5 separate dissections.

***Liposome preparation*** Liposomes were prepared by evaporation from chloroform:methanol lipid stocks, rehydration at 10 mM [lipid] in reconstitution buffer (25 mM HEPES-NaOH pH 7.4, 100 mM KCl), and extrusion as described (Bradberry et al., 2019). In Fig. 2C, liposomes contained 30% POPE and the indicated amount of POPS and $PIP_2$, with the remainder comprising POPC. For Fig. 2D-H and Fig. 5, liposomes contained 35% cholesterol, 25% POPC, 15% POPS, 20% POPE, 5% phosphatidylinositol, and 1% $PIP_2$ (all from Avanti Polar Lipids).

***Cosedimentation assays*** In Fig. 2C, liposomes (2 mM [lipid]) were mixed with C2AB (4 uM) in reconstitution buffer containing 0.5 mM EGTA in volume of 100 µl; where indicated, 1.5 mM $Ca^{2+}$ was added, yielding 1.0 mM $[Ca]_{free}$. Reaction mixtures was incubated with shaking for 30 minutes, transferred to small polycarbonate centrifuge tubes, and centrifuged at 65,000 RPM in a TLA-100 rotor (Beckman). Supernatants were combined with Laemmli sample buffer, run out on SDS-PAGE gels, and C2AB was detected by staining with Coomassie Brilliant Blue. For Fig. 2D-E, conditions were the same except that the reconstitution buffer contained 5 mM nitrilotriacetic acid (NTA) and 1 mM EGTA, along with 0-5 mM $CaCl_2$. $[Ca^{2+}]_{free}$ in these buffers was established using home-built $Ca^{2+}$ minielectrodes (Bers et al., 2010; Hove-Madsen et al., 2010). For fig. S5, NBD-C2AB (250 nM) was combined with liposomes of the same formulation in reconstitution buffer containing 5 mM NTA and 1 mM EGTA. This mixture was immediately centrifuged at 90,000 RPM in a TLA-100 rotor, the supernatants mixed with Laemmli buffer and subjected to SDS-PAGE, and the labeled C2AB was detected by in-gel fluorescence with a

CCD gel imaging device (GE). Independent experiments were defined as replicates performed with separately prepared batches of C2AB and liposomes.

***Syt1-t-SNARE binding assays*** Binding assays were performed as described previously (Courtney et al., 2018b). Briefly, purified WT or mutant C2AB protein containing an N-terminal HaloTag was bound to HaloLink beads, the beads were washed, and these Halo-C2AB beads were incubated with purified t-SNARE heterodimer in buffer containing 150 mM NaCl, 25 mM HEPES-NaOH pH 7.4, 1% Triton X-100, and 1 mM EGTA +/- 1.5 mM $CaCl_2$ for 30 minutes at room temperature with rotation. The beads were washed (3 x 1 ml) in the same buffer and the bound t-SNAREs eluted with Laemmli sample buffer. This eluate was subjected to SDS-PAGE and t-SNAREs were detected by Coomassie staining. Independent experiments were defined as replicates performed with separately prepared batches of C2AB and t-SNAREs.

***Stopped-flow rapid mixing*** Syt1 C2AB (4 μM), liposomes (1 mM), and $CaCl_2$ (250 μM) were combined in reconstitution buffer and loaded into one syringe of an SX-18.MV stopped-flow spectrometer (Applied Photophysics). The second syringe of the stopped-flow device was filled with quin-2 (500 μM) in reconstitution buffer. Equal volumes from the two syringes were rapidly mixed at room temperature while monitoring quin-2 fluorescence. Excitation at 335 nm was provided by a xenon arc lamp via monochromator while emission was monitored via a 470 nm long-pass filter (KV470, Schott). Exponential decays were fitted using Prism (GraphPad) before normalization, with the first 1.5 ms of each trace omitted to account for instrument dead time. Independent experiments were defined as replicates performed with a unique combination of separately prepared batches of protein and lipid.

***Penetration assays*** Labeled syt1 C2AB (250 nM) and liposomes (0.6 mM) were combined in reconstitution buffer containing 5 mM NTA, 1 mM EGTA (500 μl total volume) in a quartz cuvette. $CaCl_2$ (100 mM or 1 M stocks) were added to achieve the $[Ca^{2+}]_{free}$ indicated in Fig. 5. Spectra (470 nm excitation, 490-630 nm emission scan) were acquired before and after the addition of lipids, as well as

after each $Ca^{2+}$ addition, using a fluorimeter with excitation and emission monochromator slits set to 4 nm (Photon Technology International). Spectra were corrected for scattering using a lipid blank, and additional scattering after addition of $Ca^{2+}$ did not contribute substantially to the observed signal in the $[Ca^{2+}]_{free}$ range used. $dF/F_0$ values were calculated by averaging the raw, baseline-corrected intensity from 510-610 nm and normalizing to the fluorescence observed prior to the addition of liposomes. Independent experiments were defined as replicates performed with separately prepared batches of protein and lipid.

***Quantification and statistical analysis*** All electrophysiological data in Fig. 2 were acquired and analyzed by an investigator blinded to the genotype of each condition. All other data were collected and analyzed in a non-blinded fashion. Values are reported as mean ± standard error of the mean (SEM) or as means with 95% confidence intervals as indicated in the figure legends. Replicates are defined as indicated in the corresponding Methods sections and in the figure legends. All data were tested for normality prior to choosing the appropriate statistical test. No estimation of required sample sizes was performed. All statistical analysis was performed using Prism (GraphPad).

**Tables and Figures**

| | D304G (male) | D366E (female) | I368T (male) |
|---|---|---|---|
| **Infantile hypotonia** | Yes | Yes | Yes |
| **First sat independently** | 3 yrs | 14 mo. | 4 yrs |
| **First walked** | - | 2 yrs | 10 yrs |
| **Self-injurious behavior** | Yes | No | Yes |
| **Movement disorder** | Yes: dystonia | No | Yes: dystonia, ballismus of lower limbs, chorea |
| **Receptive language** | None | Responds to name | None |
| **Expressive language** | None | 4-5 words at age 4 yrs | None |
| **MRI brain** | Normal | Normal | Normal |
| **Epilepsy** | No | No | No |
| **EEG** | (at 4 yrs, asleep) High-amplitude slow waves with intermittent epileptiform spikes | (at 2 yrs, awake) Diffuse slow background rhythm with frequent high-voltage (180-240 uV) slow waves | (at 2 yrs, awake) Diffuse slow background rhythm, frequent very-high amplitude (300-600 uV) slow waves |
| **Visual Evoked Potentials** | Not assessed | Increased latency, reduced amplitude | Increased latency, reduced amplitude |
| **Other conditions** | Scoliosis, gastroesophageal reflux, esotropia | Atrial septal defect, laryngomalacia, esotropia | Talipes equinovarus, esotropia |

**Table 1. Clinical histories of patients with *de novo* heterozygous missense mutation in *SYT1*.** Histories were obtained directly from patient records and interviews with family members (D304G, D366E) or from previously published case histories (I368T). Phenotypes associated with these mutations are highly variable; among these patients, mutation D365E is associated with a substantially milder phenotype.

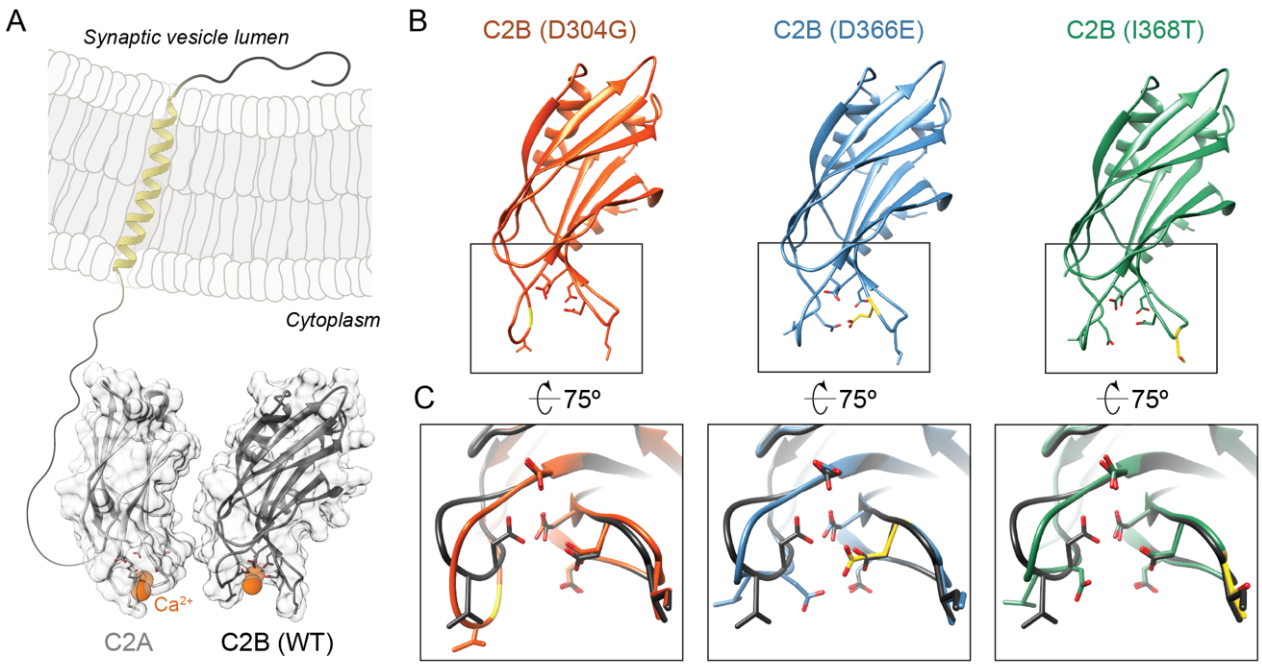


**Figure 1. X-ray crystallographic structures of human syt1 C2B domains harboring disease-associated mutations.** (A) Schematic diagram of full-length syt1 embedded in a synaptic vesicle membrane. Each C2 domain was rendered from an X-ray crystal structure (C2A: PDB 1RSY, Sutton et al. 1995; C2B: 6TZ3, this work). The membrane is drawn to scale, and the N-terminal segments before C2A were added with a drawing program to illustrate the topology of syt1. $Ca^{2+}$ ligands are rendered in wireframe, and $Ca^{2+}$ ions are shown as orange spheres. (B) X-ray crystal structures of human syt1 C2B domains harboring disease-associated mutations. In each case, the overall fold of the WT C2 domain is preserved, and differences in the positions of $Ca^{2+}$-binding/membrane-penetration loops are attributable to crystal packing artifacts. (C) Comparison of mutant $Ca^{2+}$-binding sites to the WT protein. The WT structure was rendered in grey and overlaid on each mutant, to illustrate the effect of each mutation on the $Ca^{2+}$-binding pocket: D304G removes an acidic $Ca^{2+}$ ligand; D366E preserves the ligand but makes the binding pocket smaller; and I368T reduces the hydrophobicity of the membrane-penetrating tip of loop 3.

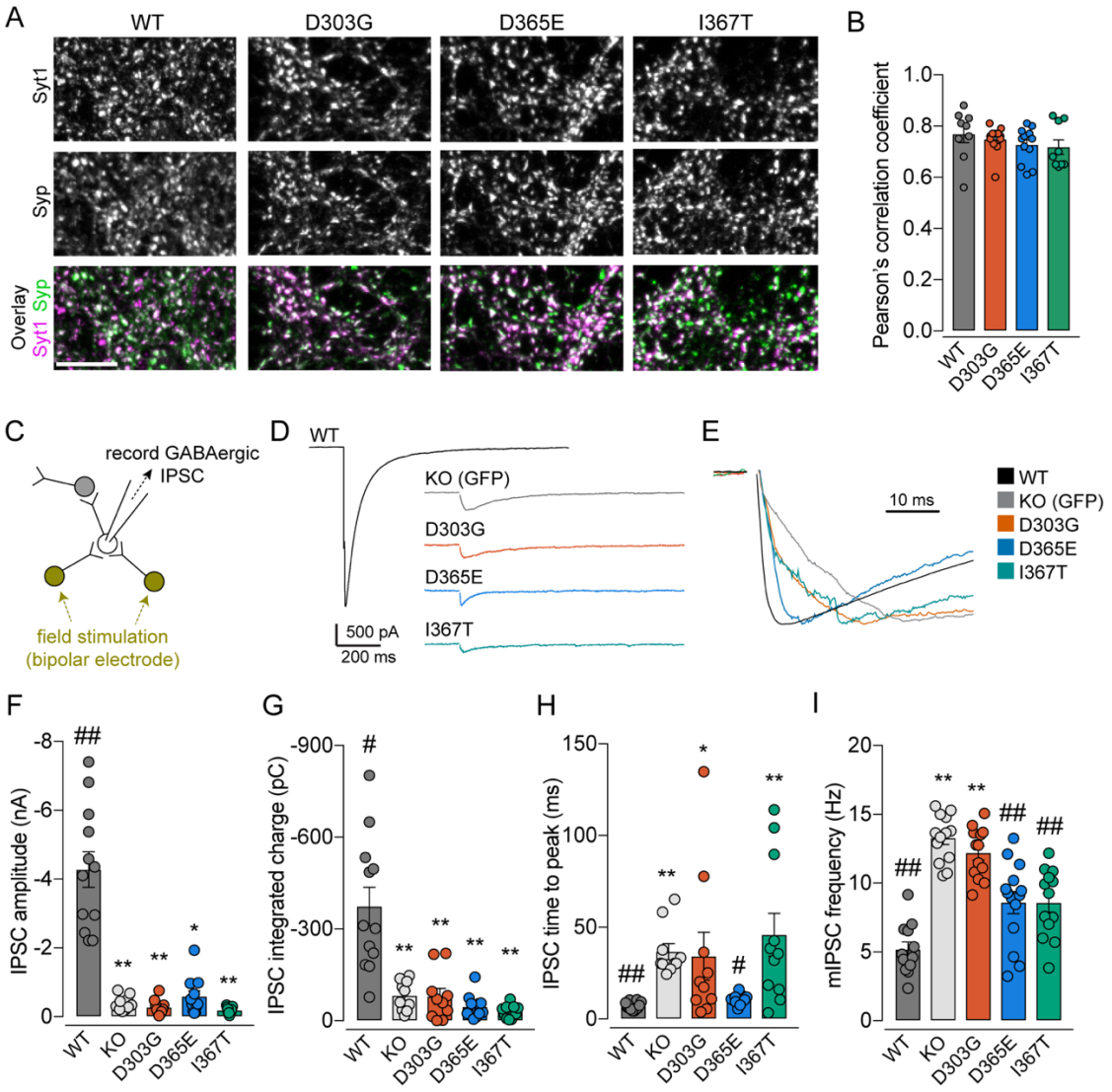


**Figure 2. Disease-associated syt1 variants fail to support synaptic transmission but have distinct phenotypes.** (A) Confocal micrographs of cultured hippocampal neurons expressing WT or mutant syt1 variants immunolabeled for syt1 and the presynaptic marker synaptophysin (syp). Scale bar, 10 µm. (B) Colocalization of syt1 variants and syp was quantified via calculation of Pearson's correlation coefficient. No significant differences were observed between WT and mutant variants ($n$ = 9-12 fields of view from 3-4 coverslips from at least 2 cultures). (C) Scheme of whole-cell patch clamp measurement of synaptic transmission in cultured cortical neurons. GABAergic responses to maximal field stimulation using a bipolar field electrode were isolated pharmacologically. (D) Average traces of evoked IPSCs from neurons expressing no syt1 (KO), WT, or mutant syt1 variants. Stimulus artifacts are removed from KO and mutant traces for clarity. (E) Evoked IPSCs shown with normalized amplitude on an expanded timescale. (F) Quantification of evoked IPSC amplitudes. (G) Quantification of total evoked IPSC charge. (H) Quantification of IPSC time to peak. D365E was the only variant that yielded rapid release kinetics comparable to the WT protein. (I) Quantification of miniature IPSC frequency, recorded in TTX without stimulation. For panels. F-I, $n$ = 10-15 cells from at least 2 separate cultures. Significance values: *, $p < 0.05$ vs. WT; **, $p < 0.006$ against WT; #, $p < 0.05$ vs KO, ##, $p < 0.005$ vs KO (Kruskal-Wallis test with Dunn's multiple comparison test).

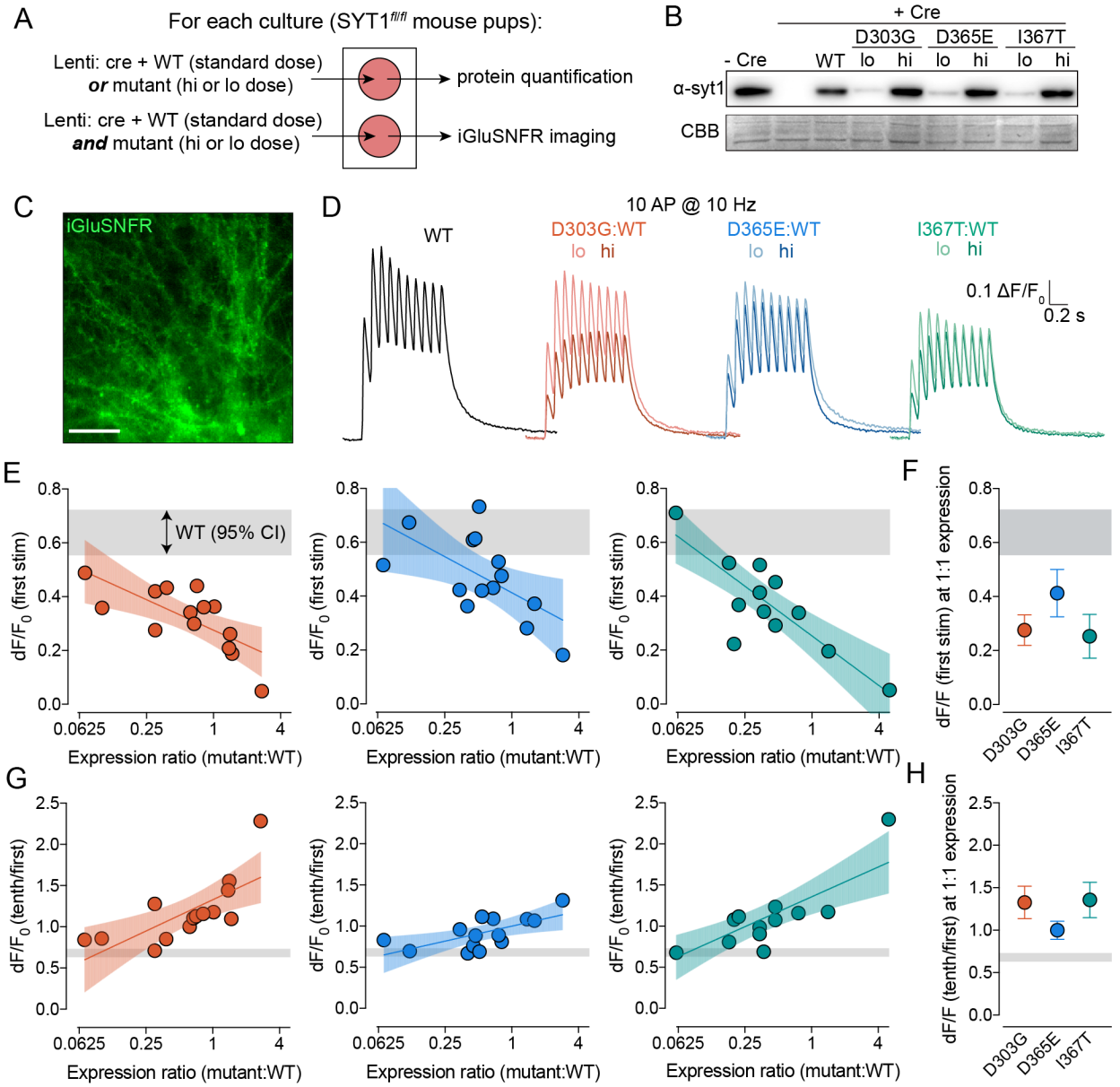


**Figure 3. Co-expression of mutant and WT syt1 defines a dominant-negative action for each mutation that varies in potency.** (A) Scheme of approach used to address dominant-negative activity for each mutant. Quantification of expression level was performed in parallel with optical imaging of evoked neurotransmitter release. (B) Representative immunoblot and loading control (CBB: Coomassie Brilliant Blue) for syt1 quantification experiments. (C) Representative field of view for iGluSNFR imaging; scale bar, 25 µm. (D) Representative raw traces for iGluSNFR imaging of samples expressing only WT syt1 or WT syt1 in combination with mutant syt1. These traces correspond to the same experiment for which protein quantification is shown in panel (B). In each case, the same amount of lentivirus used to achieve the WT expression shown in panel (B) was used, with either a low or high dose lentivirus encoding mutant syt1 added simultaneously. (E) The normalized fluorescence transient ($dF/F_0$) upon the first stimulus pulse was plotted against the ratio of WT and mutant protein expressed using the same lentivirus dose in the same experiment. Each point represents an average of 4 fields of view from a single coverslip (N = X coverslips, Y experiments). Pooled results were plotted on a log-linear plot and fit by linear

regression. Lines display best-fit with shaded regions depicting 95% confidence intervals. (F) The 95% confidence intervals corresponding to the linear model at 1:1 mutant:WT expression are plotted, demonstrating the increased dominant-negative potency of variants D303G and I367T over D365E. (G) As in panel (E), but with y-axes displaying the amplitude of the tenth fluorescence transient normalized to the first fluorescent transient of a 10 Hz, 10-pulse stimulus train ($dF/F_0$(tenth/first)). (H) as in panel (F), but with 95% confidence interval of the fit to $dF/F_0$(tenth/first) at 1:1 mutant:WT expression plotted. For all experiments, $n$ = 13-14 coverslips from at least 4 separate cultures.

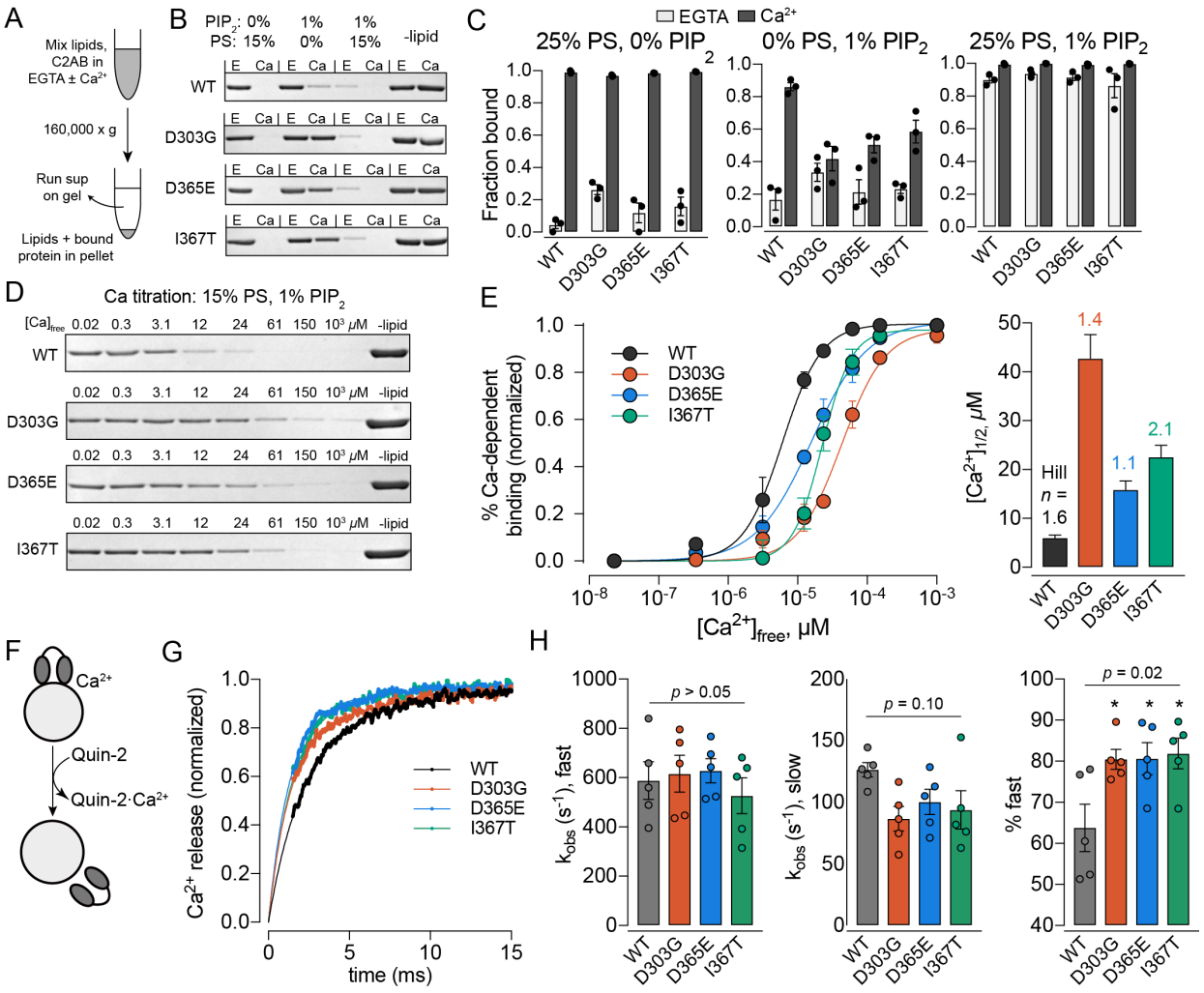


**Figure 4. Disease-associated syt1 variants cause deficits in $Ca^{2+}$-dependent lipid binding activity.** (A) Scheme of the cosedimentation assay used to monitor lipid binding. (B) Representative Coomassie-stained gel of a cosedimentation assay showing depletion of the protein from supernatant upon binding to liposomes. (C) Pooled results of cosedimentation assays using the indicated lipid compositions ($n = 3$ independent batches of liposomes and proteins). (D) Representative Coomassie-stained gel of a cosedimentation assay performed while titrating $[Ca^{2+}]_{free}$ using an EGTA-NTA $Ca^{2+}$ buffering system. (E) Pooled results of $Ca^{2+}$ titration cosedimentations. Each point is depicted as the mean ± SEM of at least 4 experiments. Dose-response curves were fitted using the Hill equation. The right panel depicts the derived $[Ca^{2+}]_{1/2}$ values; error bars represent the standard error. Calculated Hill coefficients are noted for each variant. (F) Assay scheme for measuring the kinetics of $Ca^{2+}$ release from protein-membrane complexes. $Ca^{2+}$, syt1 C2AB, and liposomes are combined, then mixed with the fluorescent $Ca^{2+}$ indicator Quin-2 in a stopped-flow rapid-mixing spectrometer. (G) Average traces for $Ca^{2+}$ release kinetics; these were fitted with double exponential functions (smooth lines) extrapolated to $t = 0$. (H) Parameters from the biexponential fits are plotted. Each mutation had minor effects on the slow component of $Ca^{2+}$ release but also increased the relative amplitude of the fast component of $Ca^{2+}$ release ($n = 5$ unique combinations of protein and lipid batches). Significance values: indicated $p$-values indicate results of one-way ANOVA; *, $p < 0.05$ vs. WT, Dunnett's multiple comparisons test.

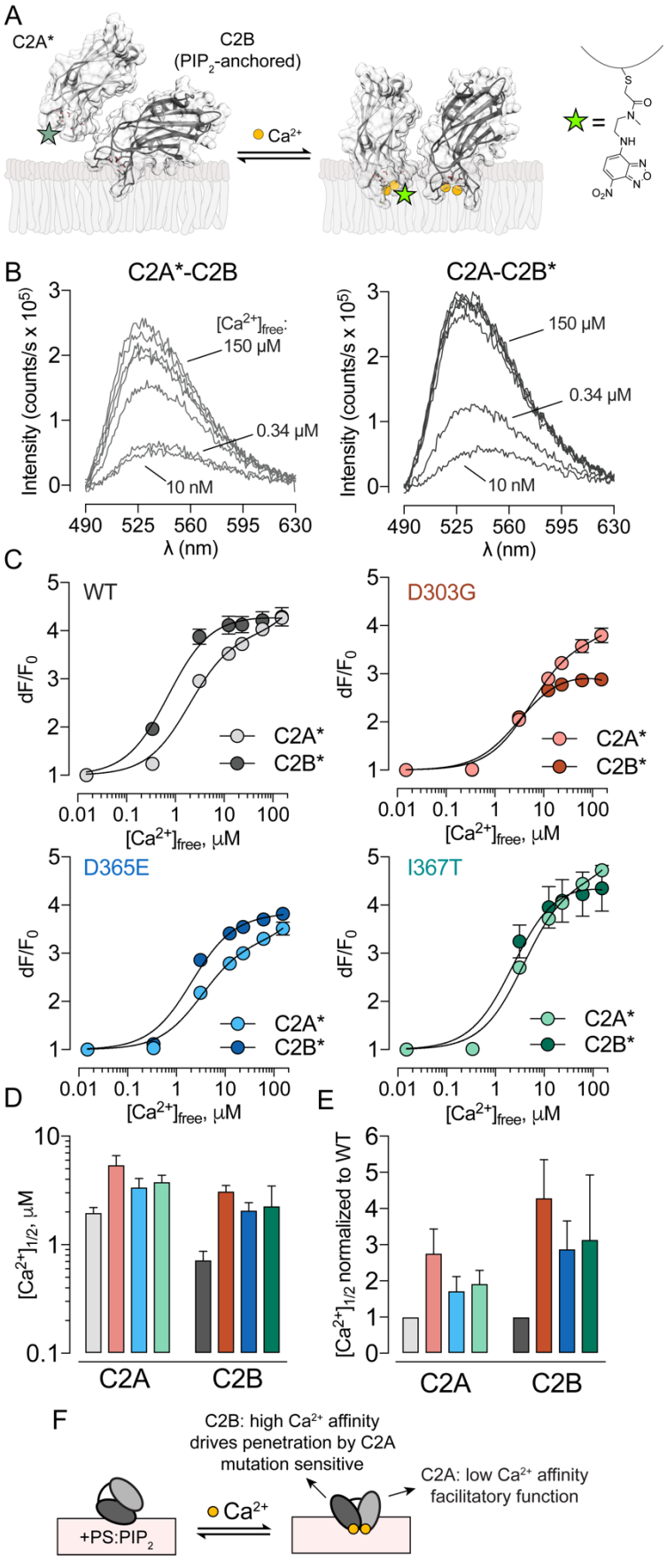
A
C2A*
C2B
(PIP2-anchored)
Ca2+
B
C2A*-C2B
C2A-C2B*
Intensity (counts/s x 10^5)
[Ca2+]free:
150 µM
0.34 µM
10 nM
λ (nm)
C
WT
D303G
D365E
I367T
dF/F0
C2A*
C2B*
[Ca2+]free, µM
D
[Ca2+]1/2, µM
C2A
C2B
E
[Ca2+]1/2 normalized to WT
F
C2B: high Ca2+ affinity
drives penetration by C2A
mutation sensitive
C2A: low Ca2+ affinity
facilitatory function
+PS:PIP2

**Figure 5. Disease-associated syt1 variants disrupt a low $Ca^{2+}$ affinity membrane penetration mode in C2A and a novel, high $Ca^{2+}$ affinity penetration mode in C2B.** (A) Scheme illustrating the membrane penetration assay. Syt1 C2AB was labeled with the environmentally-sensitive probe NBD (green star) and adsorbed to liposomes containing 15% PS and 3% $PIP_2$, which together mediate $Ca^{2+}$-independent syt1 C2AB-liposome binding, before the addition of $Ca^{2+}$. Pre-adsorption of C2AB mitigates the entropic benefit that accompanies binding by a single high-affinity site and thus allows for specific examination of penetration by C2A and C2B (see text). (B) Representative raw traces of NBD fluorescence emission upon titration of $Ca^{2+}$. (C) NBD fluorescence emission from C2AB labeled on either C2A or C2B was integrated from 510-610 nm and plotted against $[Ca^{2+}]_{free}$ ($n$ = 4 unique combinations of lipid and protein batches) for WT and each mutant variant form of syt1. Overlaid lines represent fits from single-site binding models. (D) The $[Ca^{2+}]_{1/2}$ value was calculated for penetration by C2A and C2B for WT and mutant variants. Error bars represent standard errors. (E) $[Ca^{2+}]_{1/2}$ values for $Ca^{2+}$-dependent membrane penetration normalized to WT. Error bars represent propagated standard errors. (F) Model depicting specialization of the individual C2 domains of syt1. C2B contains a higher-affinity $Ca^{2+}$-binding site and is more sensitive to mutations, whereas C2A contains a lower-affinity site and is functionally less sensitive to mutations.

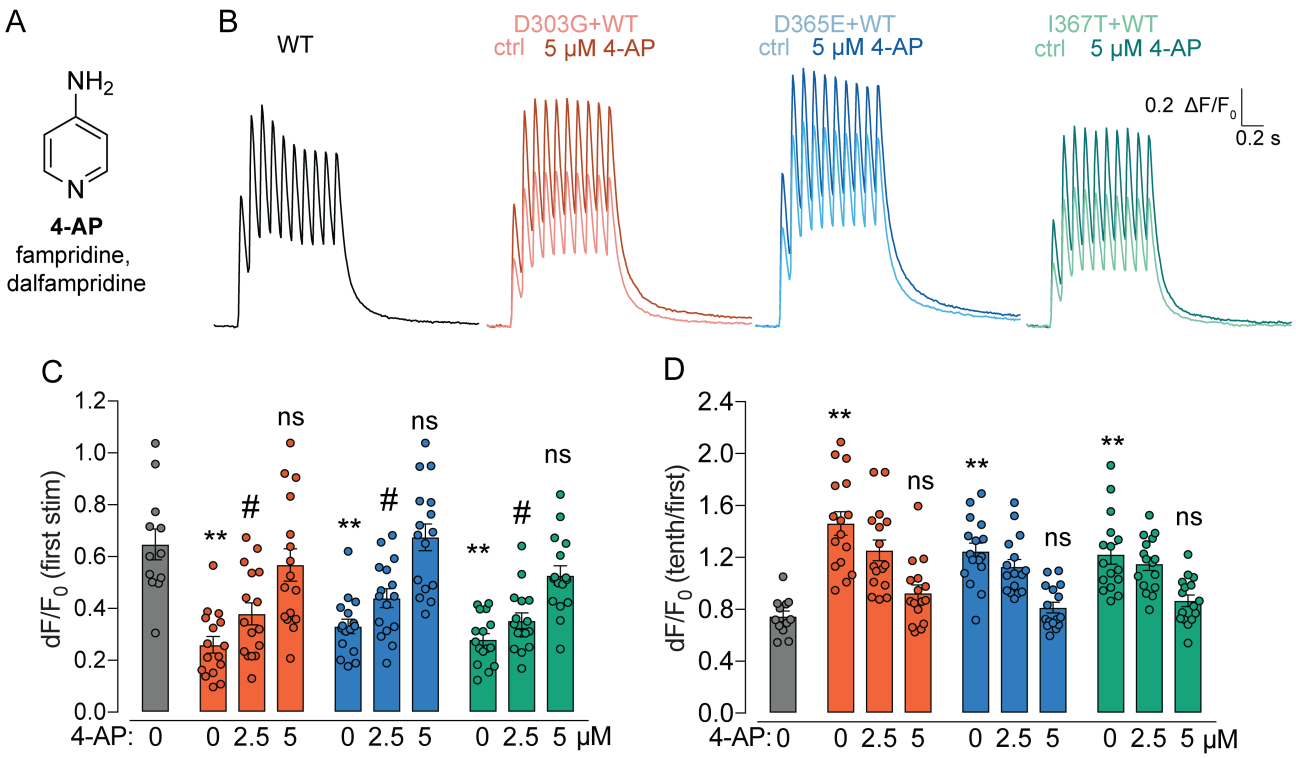


**Figure 6. Rescue of dominant-negative syt1 mutant phenotypes by a clinically approved, centrally acting $K^+$ channel blocker.** (A) Structure and generic names of 4-aminopyridine, a centrally-acting voltage-gated $K^+$ channel antagonist clinically approved for the treatment of walking symptoms in multiple sclerosis. (B) Representative iGluSNFR $dF/F_0$ traces from individual fields of view before and after treatment of 5 µM 4-aminopyridine. Cultures were transduced with lentivirus to achieve ~1:1 expression of mutant and WT protein. (C) $dF/F_0$ transients upon the first stimulation of a 10-AP train are plotted for each genotype in control bath, followed by the addition of 4-AP to 2.5 and 5 µM. The same fields of view were imaged in control and each 4-AP condition, enabling the use of paired statistics. (D) as in (C) but for $dF/F_0$ transients for the tenth response normalized to the first response. Both synaptic release parameters normalized in response to 4-AP in a dose-dependent fashion, with near-complete rescue of WT glutamate release at 5 µM 4-AP. For all experiments, $n$ = 12-16 fields of view from 3-4 coverslips from at least 2 separate cultures. Significance values: ns, $p > 0.3$ vs. WT (One-way ANOVA with Dunnett's multiple comparisons test), #, $p < 0.01$ vs ctrl for the same genotype (paired $t$-test).

**Appendix**

| | Syt1 C2B WT | Syt1 C2B D304G | Syt1 C2B D366E | Syt1 C2B I368T |
|---|---|---|---|---|
| **PDB Code** | 6TZ3 | 6U41 | 6U4W | 6U4U |
| **Wavelength** | 1.097 | 0.984 | 0.9795 | 1.099 |
| **Resolution range** | 23.64 - 1.17 (1.212 - 1.17) | 34.59 - 1.7 (1.761 - 1.7) | 27.91 - 1.4 (1.45 - 1.4) | 26.32 - 1.3 (1.347 - 1.3) |
| **Space group** | P $3_2$ 2 1 | P $3_2$ 2 1 | P $3_2$ 2 1 | P $3_2$ 2 1 |
| **Unit cell** | 54.594 54.594 103.904 90 90 120 | 54.29 54.29 103.77 90 90 120 | 54.39 54.39 103.93 90 90 120 | 54.41 54.41 103.77 90 90 120 |
| **Total reflections** | 279817 (28084) | 369674 (24602) | 328559 (32897) | 197826 (12066) |
| **Unique reflections** | 59556 (5530) | 20015 (1882) | 35709 (3505) | 44121 (4117) |
| **Multiplicity** | 4.7 (4.7) | 18.5 (13.1) | 9.2 (9.4) | 4.5 (2.9) |
| **Completeness (%)** | 96.36 (91.03) | 99.50 (96.32) | 99.14 (96.64) | 99.06 (93.21) |
| **Mean I/sigma(I)** | 16.71 (5.28) | 50.73 (16.99) | 16.44 (2.45) | 20.99 (2.70) |
| **Wilson B-factor** | 15.76 | 14.94 | 12.27 | 11.90 |
| **R-merge** | 0.03867 (0.3145) | 0.03775 (0.1251) | 0.07736 (1.309) | 0.03336 (0.4135) |
| **R-meas** | 0.04362 (0.3532) | 0.0388 (0.1302) | 0.08231 (1.386) | 0.03779 (0.4988) |
| **R-pim** | 0.01979 (0.1578) | 0.008874 (0.03528) | 0.02758 (0.4533) | 0.01742 (0.2734) |
| **CC1/2** | 0.999 (0.914) | 1 (0.994) | 0.998 (0.746) | 1 (0.859) |
| **CC*** | 1 (0.977) | 1 (0.999) | 0.999 (0.924) | 1 (0.961) |
| **Reflections used in refinement** | 59044 (5532) | 20014 (1883) | 35500 (3397) | 44117 (4117) |
| **Reflections used for R-free** | 1992 (187) | 1085 (87) | 1852 (151) | 2002 (182) |
| **R-work** | 0.1554 (0.1415) | 0.1569 (0.1606) | 0.1864 (0.5205) | 0.1434 (0.1991) |
| **R-free** | 0.1750 (0.1736) | 0.1783 (0.1982) | 0.2104 (0.6876) | 0.1695 (0.2321) |
| **CC(work)** | 0.935 (0.939) | 0.961 (0.954) | 0.928 (0.342) | 0.966 (0.926) |

| | | | | |
|---|---|---|---|---|
| **CC(free)** | 0.942 (0.945) | 0.963 (0.935) | 0.933 (0.304) | 0.968 (0.914) |
| **Number of non-hydrogen atoms** | 1425 | 1568 | 1414 | 1640 |
| **macromolecules** | 1231 | 1351 | 1284 | 1378 |
| **ligands** | 15 | 25 | 20 | 45 |
| **solvent** | 179 | 192 | 110 | 217 |
| **Protein residues** | 148 | 148 | 149 | 148 |
| **RMS(bonds)** | 0.013 | 0.008 | 0.011 | 0.008 |
| **RMS(angles)** | 1.25 | 0.85 | 1.12 | 1.02 |
| **Ramachandran favored (%)** | 97.26 | 100.00 | 97.96 | 98.60 |
| **Ramachandran allowed (%)** | 2.74 | 0.00 | 2.04 | 1.40 |
| **Ramachandran outliers (%)** | 0.00 | 0.00 | 0.00 | 0.00 |
| **Rotamer outliers (%)** | 1.43 | 1.96 | 1.41 | 1.27 |
| **Clashscore** | 1.58 | 2.14 | 2.26 | 3.84 |
| **Average B-factor** | 24.37 | 22.82 | 21.98 | 18.57 |
| **macromolecules** | 21.90 | 20.37 | 20.02 | 15.53 |
| **ligands** | 50.91 | 69.67 | 69.86 | 50.20 |
| **solvent** | 39.13 | 33.99 | 36.16 | 31.35 |

**Table S1. Data collection and refinement statistics for syt1 C2B X-ray crystallography, related to Figure 1.** Statistics for the highest-resolution shell are shown in parentheses.

Patient D304G

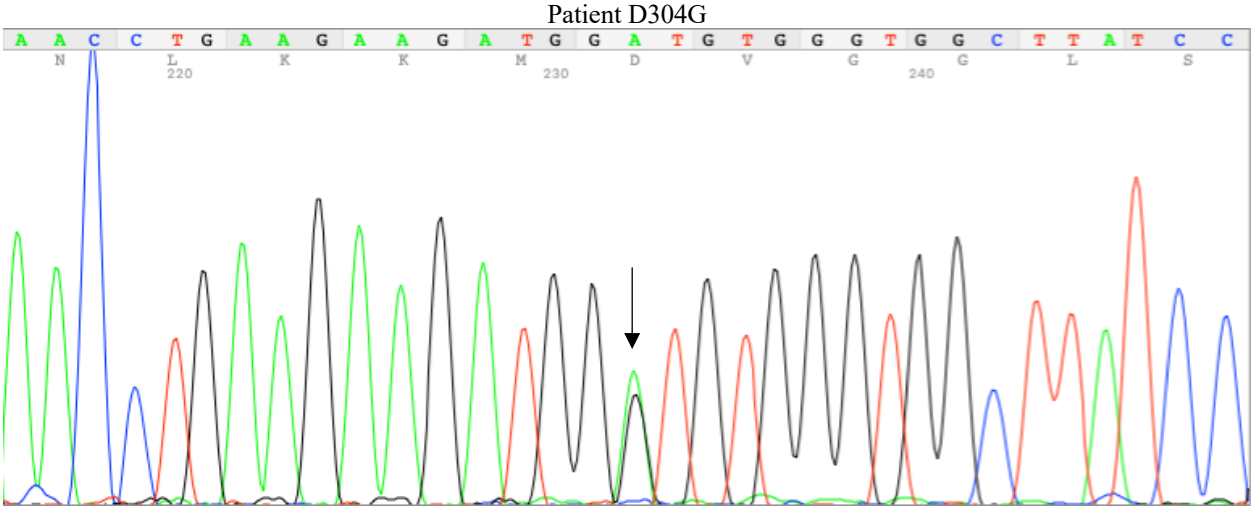

Patient D366E

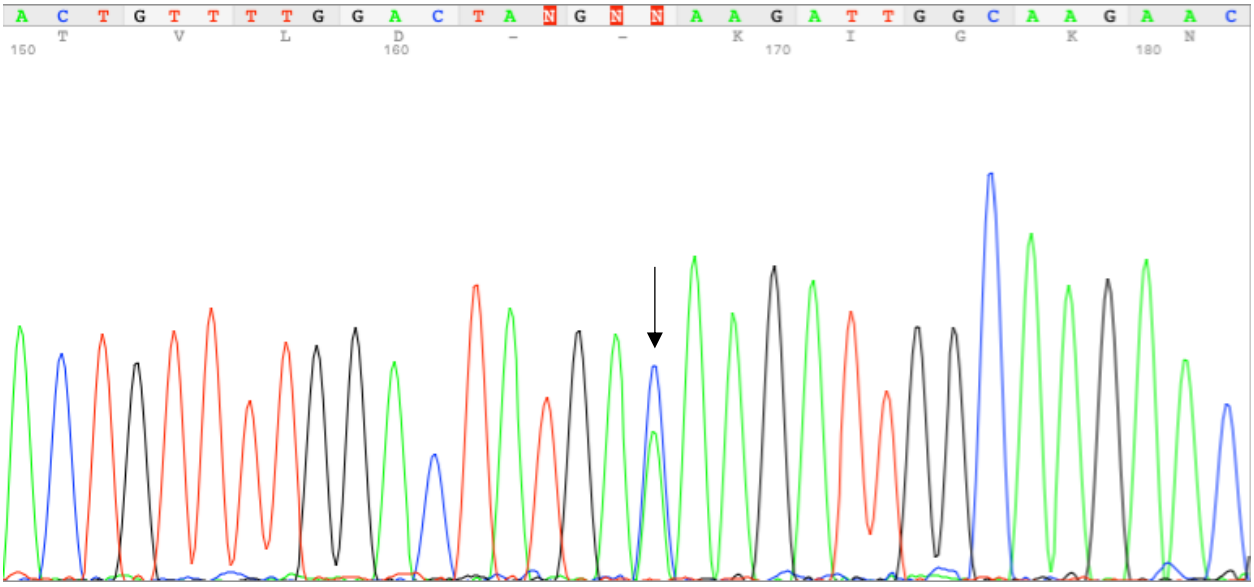

**Figure S1. Chromatograms from Sanger sequencing of genomic DNA from patients harboring mutations D304G and D366E, related to Table 1.** Genomic DNA was extracted from saliva samples, amplified with PCR, and subjected to Sanger sequencing. Results confirm heterozygosity at the positions in question, indicated with arrows (D304G: A/G; D366E: A/C).

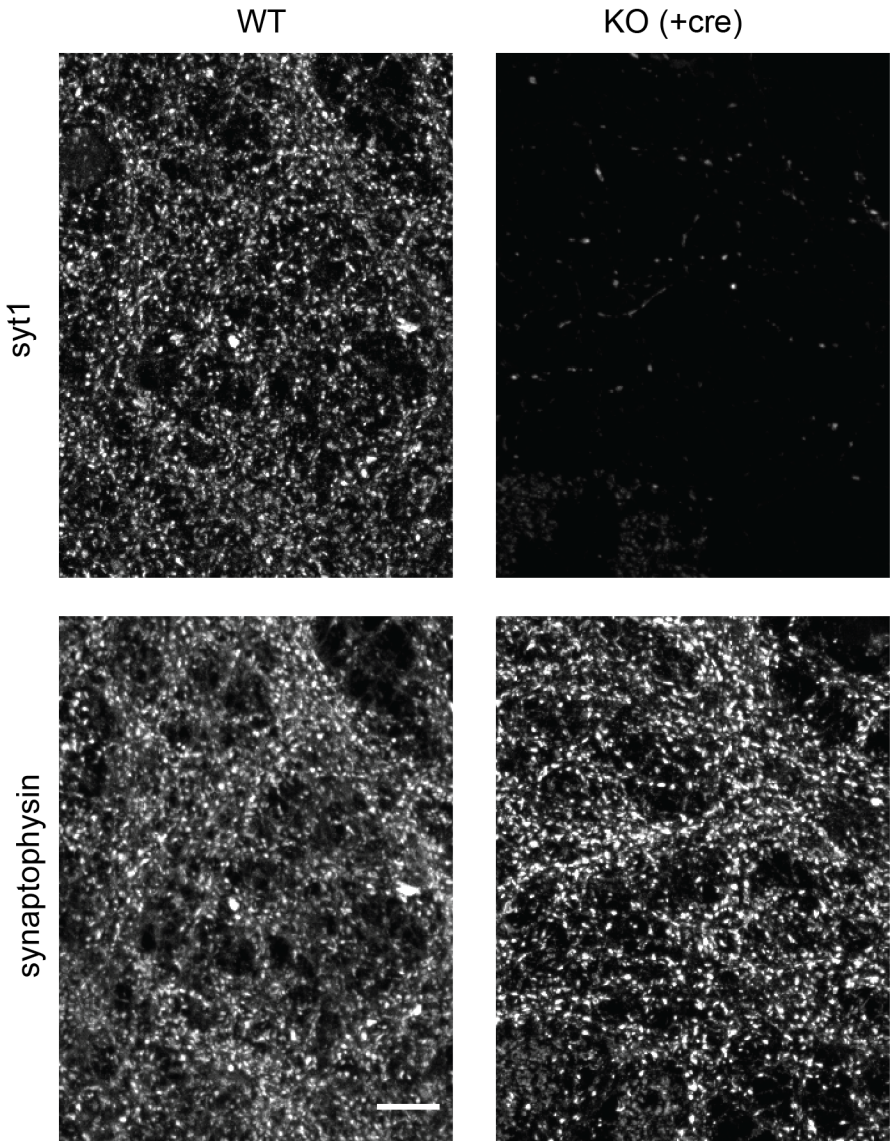


**Figure S2**. **Immunocytochemical staining for syt1 is specific, related to Figure 2.** Samples from *Syt1*$^{fl/fl}$ coverslips were transduced with lentivirus encoding Cre recombinase +/- lentivirus encoding WT syt1. Samples transduced with Cre alone did not stain with anti-syt1 antibody (upper panels) despite a qualitatively normal distribution of nerve terminals, as shown by staining with anti-synaptophysin antibody (lower panels). Scale bar, 10 μm.

***Extra sum-of-squares F test***

| | dF/F(first stim) | dF/F(tenth/first) |
|---|---|---|
| **Null hypothesis** | One curve for all data sets | One curve for all data sets |
| **Alternative hypothesis** | Different curve for each data set | Different curve for each data set |
| **P value** | 0.0053 | 0.0219 |
| **Conclusion (alpha = 0.05)** | Reject null hypothesis | Reject null hypothesis |
| **Preferred model** | Different curve for each data set | Different curve for each data set |
| **F (DFn, DFd)** | 4.433 (4, 35) | 3.284 (4, 35) |

***Aikike information criteria***

| | dF/F(first stim) | dF/F(tenth/first) |
|---|---|---|
| **Simpler model** | One curve for all data sets | One curve for all data sets |
| **Probability it is correct** | 4.61% | 23.86% |
| **Alternative model** | Different curve for each data set | Different curve for each data set |
| **Probability it is correct** | 95.39% | 76.14% |
| **Ratio of probabilities** | 20.7 | 3.19 |
| **Preferred model** | Different curve for each data set | Different curve for each data set |
| **Difference in AICc** | 6.06 | 2.32 |

**Table S2**. **Tests supporting the use of separate curves to fit the data in Figures 3F and 3H.** Log-linear fits (shown in Figure 3) were compared among D303G, D365E, and I367T.

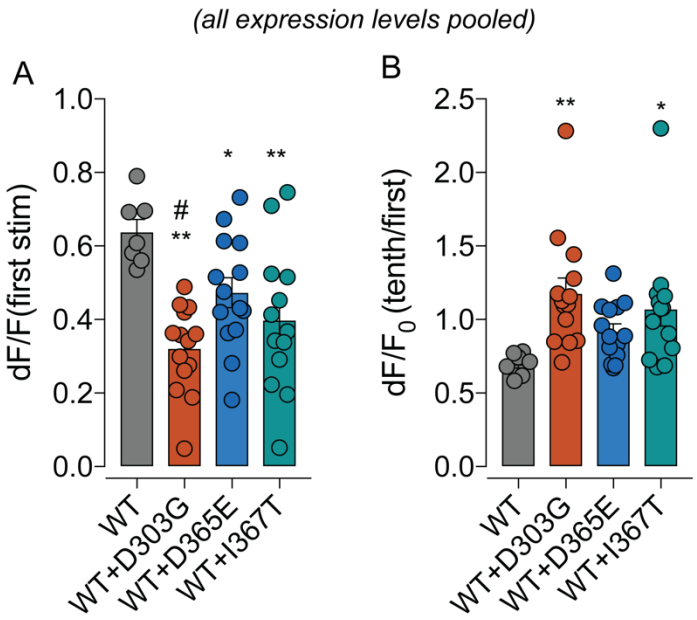


**Figure S3. Comparison of dominant-negative effects among mutant variants without controlling for expression level, related to Figure 3.** (A-B) Quantification of iGluSnFR responses on the first field stimulus (A) as well as those of tenth stimulus normalized to the first (B) in cultures expressing WT and variable amounts of mutant variant syt1. *, $p < 0.05$, **, $p < 0.006$ *vs*. WT; #, $p < 0.05$ vs. WT+D365E (One-way ANOVA with Holm-Sidak multiple comparison test (A); Kruskal-Wallis with Dunn's multiple comparison test (B)). Each data point represents the average of four fields of view from one coverslip. Error bars represent SEMs.

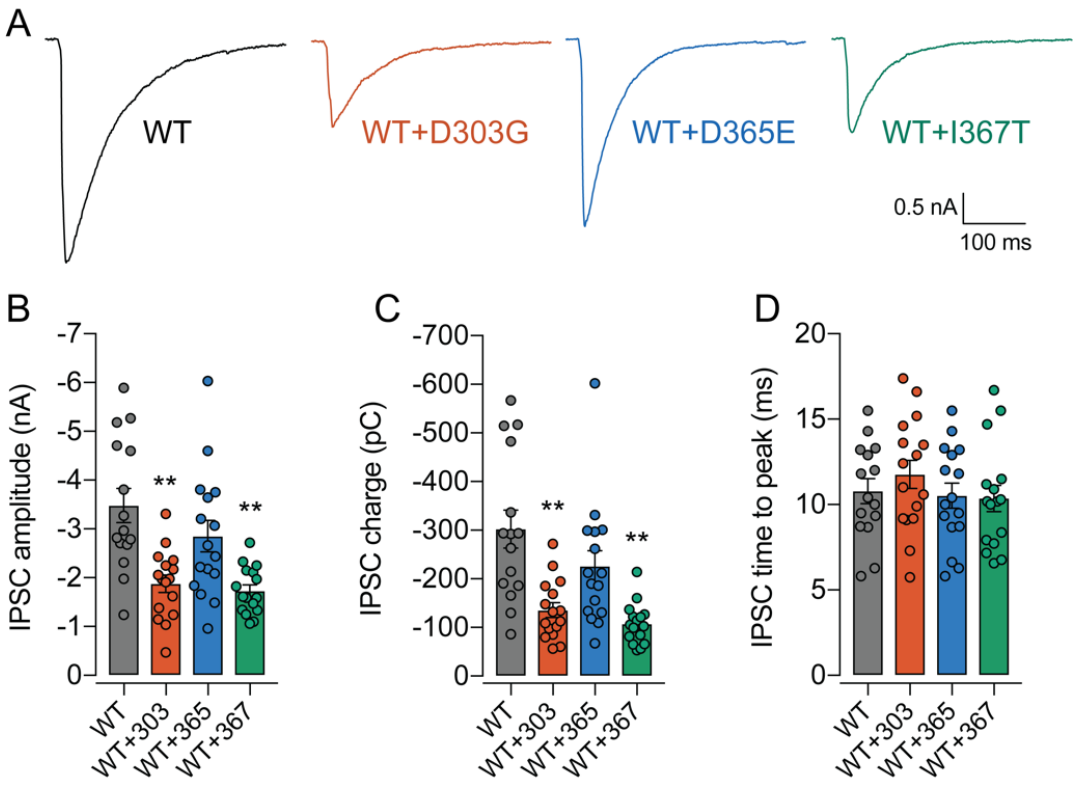


**Figure S4. Mutant variants exert dominant-negative effects on GABAergic synaptic transmission, related to Figure 3.** (A) Representative IPSC traces from cultured *Syt1*$^{fl/fl}$ hippocampal neurons transduced with lentivirus to express Cre along with WT syt1 alone or WT and mutant syt1 variants at a ~1:1 ratio. (B-D) Quantification of amplitude (B), charge (C), and time to peak (D) of evoked IPSCs for each expression condition ($n$ = 15-16 cells from 2 cultures per condition). **, $p < 0.005$ *vs*. WT (Kruskal-Wallis with Dunnett's multiple comparison test). Error bars represent SEMs.

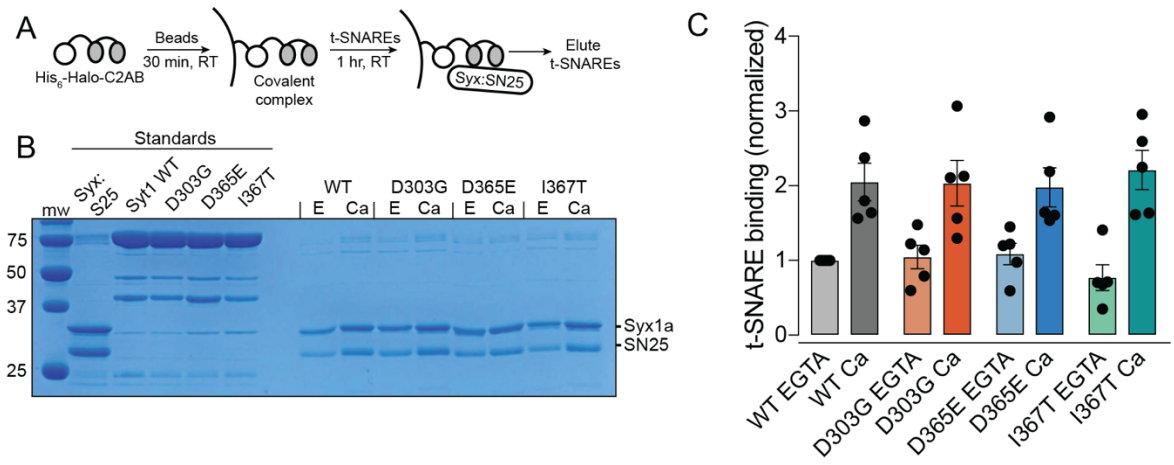


**Figure S5**. **SNARE binding is unaffected in disease-associated syt1 variants, related to Figure 4.** (A) Scheme of HaloTag-C2AB•t-SNARE binding assay. (B) Representative Coomassie-stained gel of Halo-C2AB constructs and eluted t-SNARES. Binding assays were performed in 1 mM EGTA (condition E) or 1 mM EGTA plus 1.5 mM $CaCl_2$ (0.5 mM $[Ca^{2+}]_{free}$, condition Ca). (C) Bands corresponding to eluted t-SNAREs were quantified by densitometry and normalized to WT binding in EGTA. No differences were observed between WT and mutant constructs binding to t-SNAREs in EGTA or $Ca^{2+}$. Error bars represent SEMs.

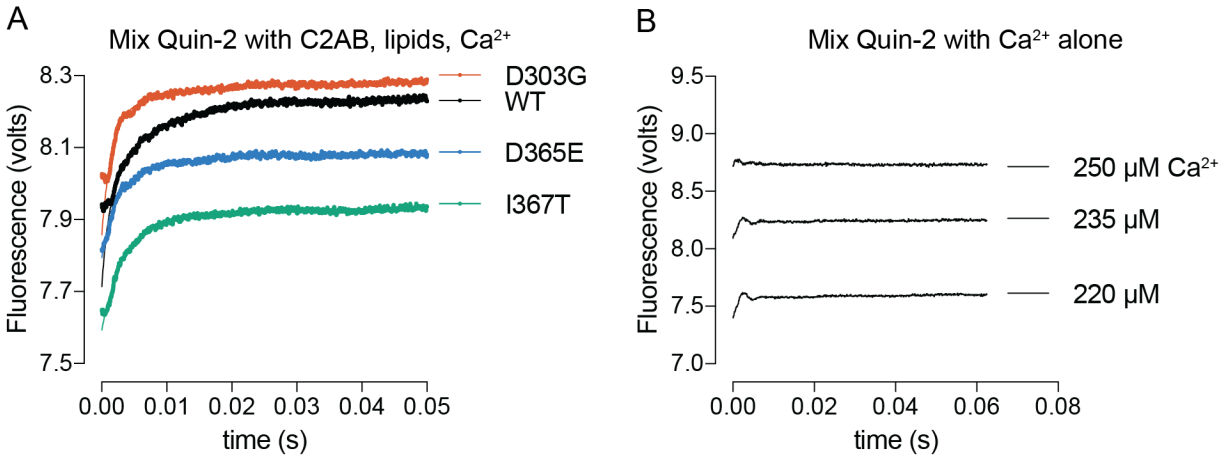


**Figure S6. Quin-2 detects kinetics of $Ca^{2+}$ release from syt1-$Ca^{2+}$-liposome complexes, related to Figure 4.** (A) Representative data from an experiment measuring $Ca^{2+}$ release from syt1-$Ca^{2+}$-liposome complexes. Each trace is the average of 5-7 single shots in the stopped-flow device. (B) Mixing quin-2 with $Ca^{2+}$ in the absence of C2AB and liposomes yields traces that are dependent on [$Ca^{2+}$] but do not provide kinetic information, demonstrating that Quin-2 binds $Ca^{2+}$ within the dead time of the instrument.

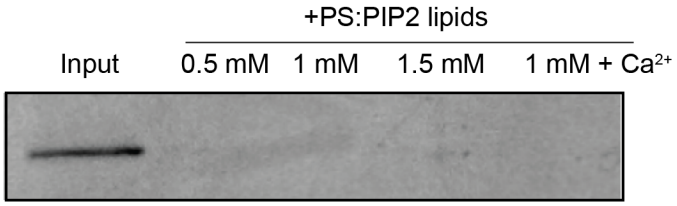


**Figure S7. $Ca^{2+}$-independent binding of NBD-C2AB to PS:$PIP_2$ vesicles, related to Figure 5**. Cosedimentation was performed with NBD-C2AB, labeled at F234C, and PS:$PIP_2$ vesicles containing 3% $PIP_2$ under the same conditions used for the penetration assays shown in **Figure 5**. Following sedimentation, the supernatant was subjected to SDS-PAGE and NBD-syt1 was detected by in-gel fluorescence. At 0.5 mM [lipid], the supernatant was completed depleted of NBD-C2AB. For penetration assays (**Figure 5**), a lipid concentration of 0.6 mM was used.

# Chapter 4: SV2A supports synaptic vesicle fusion downstream of evoked $Ca^{2+}$ entry


## Summary

SV2A, an essential transporter-like synaptic vesicle protein, has no well-defined molecular function at the synapse despite being a major target for antiepileptic drugs. While SV2A is required for normal levels of evoked neurotransmitter release, the mechanism underlying this role remains unclear. Here, we introduce a new chemogenetic approach for all-optical monitoring of excitation-secretion coupling, and we demonstrate its use in characterizing the SV2A KO phenotype in cultured hippocampal neurons. This method employs the HaloTag system to target a fast small-molecule $Ca^{2+}$ indicator, $JF_{646}$-BAPTA, to the presynaptic compartment. The far-red fluorescence of this indicator enables multiplexing with the fluorescent glutamate sensor iGluSnFR for detection of presynaptic $Ca^{2+}$ influx and glutamate release at the same axonal boutons. Evoked glutamate release probability was reduced in SV2A KO neurons without a change in presynaptic $Ca^{2+}$ entry or sensitivity to $Ca^{2+}$, suggesting that SV2 supports vesicle fusion by increasing the availability of $Ca^{2+}$-sensitive release machinery.


## Introduction

Many basic tenets of synaptic vesicle cycle are well-accepted: at the nerve terminal, vesicles are assembled locally from precursors (Rizalar et al., 2021), and these vesicles accumulate neurotransmitter and undergo $Ca^{2+}$-dependent fusion with the plasma membrane (Brose et al., 2019). However, major questions remain about basic elements of this process: which molecules and interactions drive the assembly of synaptic vesicles (Park et al., 2021)? How are these assemblies maintained during rapid vesicle recycling (Fernández-Alfonso et al., 2006; Hua et al., 2011)? What are the mechanisms for synaptic vesicle quality control and degradation?

One protein that exemplifies the need for further study is SV2A, one of the first-cloned synaptic vesicle proteins (Bajjalieh et al., 1992; Buckley and Kelly, 1985; Feany et al., 1992). These pioneering studies established that SV2A is homologous to transport proteins in the major facilitator superfamily, whose members largely carry out secondary active transport processes and include the vesicular

transporters for classical neurotransmitters (Yan, 2015). Mice lacking SV2A (SV2A KO) fail to gain weight, develop seizures, and die by ~14 days of age (Crowder et al., 1999; Janz et al., 1999). Action-potential-dependent neurotransmitter release is attenuated in cultured SV2A KO neurons (Chang and Sudhof, 2009; Custer, 2006), suggesting a mechanism for epileptogenesis, but how SV2A modulates the release machinery is unknown. In particular, whether SV2A affects presynaptic $Ca^{2+}$ entry, a key factor in neurotransmitter release, has not been established.

Strikingly, SV2A is also a major drug target in the treatment of epilepsy (Löscher et al., 2016). The anti-epileptic drugs levetiracetam (Keppra) and brivaracetam (Briviact) bind SV2A (Klitgaard et al., 2016; Lynch et al., 2004), and it is well-established that this interaction underlies these drugs' anti-epileptic action (Kaminski et al., 2009, 2008). However, as with SV2A's endogenous function, the antiepileptic mechanism of these drugs is otherwise undefined at the molecular level. While most antiepileptic drugs directly inhibit the excitatory machinery of neurons or enhance inhibitory processes, several clues indicate an unusual mechanism of action for racetam antiepileptics. Their profile in rodent epilepsy models is atypical, and they have only subtle effects on neurotransmission even at high concentrations (García-Pérez et al., 2015; Löscher et al., 2016; Yang et al., 2015). The clinical presentation of levetiracetam overdose is unusually benign (Kartal, 2017), suggesting a mechanism of action that relies specifically on epileptic processes.

Whether SV2A affects presynaptic $Ca^{2+}$ entry, a key factor in neurotransmitter release, has not been conclusively established. While one report has suggested role for the related protein SV2B in presynaptic $Ca^{2+}$ signaling in bipolar neurons of the retina (Wan et al., 2010), other reports have used indirect methods to suggest that SV2A does (Janz et al., 1999) or does not (Chang and Sudhof, 2009; Custer, 2006) modulate presynaptic $Ca^{2+}$ signaling at small boutons in cultured neurons. To clarify the relationship between SV2A and presynaptic $Ca^{2+}$, we developed and applied an all-optical approach to monitor excitation-secretion coupling, determining that SV2A supports SV fusion downstream of presynaptic $Ca^{2+}$ entry.

**Results**

Because it is unclear at what step SV2A acts in exocytosis, we sought to definitely establish whether SV2A modulates presynaptic $Ca^{2+}$ or $Ca^{2+}$-secretion coupling. *Sv2a*$^{-/-}$ mice do not gain weight and die before reaching 2 weeks of age (Crowder et al., 1999), making brain slice studies impractical and potentially confounded by a global failure to thrive. Neuronal cultures from neonatal mouse hippocampus thus provide an ideal model to study the role of SV2A in synaptic transmission. However, the irregular morphology, long processes, and absence of tissue organization in neuronal cultures present obstacles to measuring presynaptic $Ca^{2+}$ fluxes using $Ca^{2+}$indicators loaded either by bath application or by whole-cell dialysis. Published approaches have involved combining bath-loaded $Ca^{2+}$ indicators with presynaptic markers (Hoppa et al., 2012) or targeting genetically-encoded $Ca^{2+}$ sensors to the nerve terminal (de Juan-Sanz et al., 2017), but these techniques suffer from poor rejection of non-presynaptic $Ca^{2+}$ signals or poor temporal resolution of $Ca^{2+}$ signals, respectively.

We thus took advantage of the HaloTag system (Los et al., 2008) along with recent advancements in synthetic $Ca^{2+}$ indicators (Deo et al., 2019) to target a sensitive, small-molecule $Ca^{2+}$ sensor to the presynaptic compartment. The indicator used here, $JF_{646}$-BAPTA, offers several advantages over existing $Ca^{2+}$ indicators. In particular, this far-red indicator undergoes substantial brightness increases when bound to the HaloTag protein via a chloroalkane linker, enabling spatially-resolved measurements of $Ca^{2+}$ depending on the subcellular targeting of the HaloTag protein (Deo et al., 2019). In neurons expressing a synaptophysin-HaloTag fusion protein, incubation with the acetoxymethyl ester of $JF_{646}$-BAPTA-HaloTag ligand generated a presynaptic $Ca^{2+}$ sensor with the punctate presynaptic localization of synaptophysin (syp) (**Fig. 1B**) along with the speed and sensitivity of small-molecule $Ca^{2+}$ ligands (**Fig. 1C**). While $JF_{646}$-BAPTA is a high-affinity $Ca^{2+}$ indicator ($K_D$ ~ 150 nM) (Deo et al., 2019) and thus tracks $Ca^{2+}$ fluxes slightly less faithfully than lower-affinity dyes (Sabatini and Regehr, 1998), this approach provided a substantial improvement in kinetic fidelity over a similarly targeted Syp-GCaMP6f construct (**Fig. 1C**). For each field of view, a dye-saturating stimulus performed at the end of each

experiment allowed estimation of absolute $[Ca^{2+}]_i$ using the known properties of the dye (Methods) (de Juan-Sanz et al., 2017; Deo et al., 2019; Maravall et al., 2000).

Co-expression of the fluorescent glutamate sensor iGluSnFR (Marvin et al., 2018), which is spectrally well-separated from $JF_{646}$-BAPTA, permitted paired measurements of glutamate release from the same fields of view as used for $Ca^{2+}$ measurements. In this all-optical approach to measuring excitation-secretion coupling, cultured hippocampal neurons were transduced with lentiviruses to express a synaptophysin-Halotag fusion protein as well as iGluSnFR (**Fig. 2A-B**). We applied this method to hippocampal neurons cultured from *Sv2a* WT and KO mouse pups (**Fig. 2C-F**). Resting $[Ca^{2+}]$ was unchanged between WT and KO mice (**Fig. 2C**), consistent with the absence of a change in spontaneous synaptic current frequency in *Sv2aA* KO mice (Chang and Sudhof, 2009; Crowder et al., 1999; Custer, 2006). Syp-HaloTag-$JF_{646}$-BAPTA reported peak $[Ca^{2+}]_i$ values that increased linearly with $[Ca^{2+}]_e$ under all conditions studied here, and $Ca^{2+}$ entry was unchanged between WT and KO (**Fig. 2D**). By contrast, glutamate release was attenuated in the SV2A KO at every $[Ca^{2+}]_e$ studied, in accordance with previous reports (Chang and Sudhof, 2009; Custer, 2006). For both genotypes, the relationship between iGluSnFR dF/F0 and $[Ca^{2+}]_e$ (**Fig. 2E**) was well-fit by a cooperative binding model with a Hill parameter of ~2.3 (WT: 2.2, 95% CI 1.7-2.9; KO: 2.5, 95% CI 1.9-3.0). Plotting the paired data for iGluSnFR versus peak $[Ca^{2+}]_i$ in each field of view (**Fig. 2F**) yielded a similar relationship, which was noisier but converged on values closer to 4 (WT: 4.3, 95% CI 2.9-6.1; KO: 3.5, 95% CI 2.3-5.2). These results are comparable to those obtained in young cultured hippocampal neurons using flash photolysis (Burgalossi et al., 2010), which estimate this parameter to be approximately 3. Values for the Hill coefficient and half-maximal $[Ca^{2+}]$ were nearly identical between SV2A WT and KO neurons, and the reduction in glutamate release in the SV2A KO was well-approximated by linearly scaling down the $Ca^{2+}$-glutamate release curves observed for WT neurons (**Fig. 2D-E**).

Application of 10-Hz stimulus trains (**Fig. 2G**) demonstrated that the reduced glutamate release resulted from a reduction in initial release probability (**Fig. 2H-K**), as supported by an increase in the paired-pulse ratio in SV2A KO neurons (**Fig. 2I**) as well as a normalization of evoked glutamate release

over the course of the stimulus train (**Fig. 2H, J-K**). Our results are in accordance with previous studies of glutamatergic and GABAergic transmission in SV2A KO neurons (Chang and Sudhof, 2009; Custer, 2006). Together, these results strongly suggest that SV2 does not modulate $Ca^{2+}$ influx or the direct action of $Ca^{2+}$ effector molecules, but instead controls the functional abundance of these effectors in a dynamic manner influenced by ongoing activity.

**Discussion**

The role of SV2A in synaptic transmission has been enigmatic since its discovery. The ubiquity and physiologic importance of a synaptic vesicle transporter, which does not appear to transport neurotransmitter, suggests important aspects of synaptic vesicle biology are yet to be defined. Because it is already a major drug target (Löscher et al., 2016), defining a molecular function for SV2A at the synapse would have likewise have important clinical ramifications.

A role for SV2 proteins as $Ca^{2+}$ regulators has been suggested by some studies (Janz et al., 1999; Wan et al., 2010) but not others (Chang and Sudhof, 2009; Custer, 2006). None of these studies, however, assessed $Ca^{2+}$ dynamics in small nerve terminals lacking SV2A. The chemogenetic $Ca^{2+}$-sensing construct described here (**Fig. 1**) represents a useful tool for probing presynaptic $Ca^{2+}$ and represents a favorable compromise among speed, spatial resolution, and temporal resolution versus existing techniques (**Fig. 1**). Future studies that capitalize on the spatial resolution of Syp-Halo-$JF_{646}$-BAPTA, particularly using confocal imaging techniques, may expand the use of this tool for monitoring heterogeneity of synaptic $Ca^{2+}$ transients among nerve terminals in genetically-specified populations of neurons.

Integration of Syp-Halo-$JF_{646}$-BAPTA with iGluSnFR enabled the monitoring of excitation-secretion with a convenient all-optical approach, which was employed to determine that presynaptic $Ca^{2+}$ entry is unaltered by the loss of SV2A (**Fig. 2**). The unchanged sensitivity of glutamate release to extracellular [$Ca^{2+}$] is consistent with this finding, as a reduction in $Ca^{2+}$ entry per action potential should cause a shift in this curve (**Fig. 2E-F**) to the right. Our results are likewise consistent with previous studies in cultured hippocampal neurons (Chang and Sudhof, 2009; Custer, 2006). Rather than change

$Ca^{2+}$ dynamics, SV2A appears to influence the release machinery itself. However, we interpret these data to favor an indirect mechanism of action of SV2A rather than a direct allosteric effect on the $Ca^{2+}$-secretion coupling process *per se*. The loss of a direct modulator is more likely to change the $Ca^{2+}$ dependence of exocytosis, exemplified by the phenotype observed in neurons lacking the syt1-SNARE-binding protein complexin (Reim et al., 2001) or synaptotagmin (Kochubey and Schneggenburger, 2011b). In any case, these results establish unambiguously that SV2 modulates excitation-secretion coupling downstream of $Ca^{2+}$ entry. Our results differ from those obtained from synaptic terminals of retinal bipolar neurons from SV2B knockout mice (Wan et al., 2010), though it is difficult to draw meaningful comparisons across SV2 isoforms and synapse types.

While our results help to define the physiologic role of SV2A, a well-defined molecular function remains elusive. The normalization of synaptic deficits during sustained activity (**Fig. 2G-K**) suggests that ongoing action potential firing, $Ca^{2+}$ entry, and vesicular recycling may help compensate for the absence of SV2A. One explanation for this could involve a role for SV2A in SV protein trafficking during periods of rest or development (Custer, 2006), and changes in abundance or localized trafficking of proteins such as syt1 (Yao et al., 2010; Zhang et al., 2015) may play a role in the SV2A KO phenotype. Because SV2A co-immunoprecipitates with the $Ca^{2+}$ sensor synaptotagmin-1 (syt1) (Schivell et al., 1996), and because presynaptic syt1 is less abundant at synapses lacking SV2A (Yao et al., 2010), altered trafficking of syt1 provides an attractive candidate mechanism for SV2A's role in exocytosis. However, certain point mutants suggest that presynaptic syt1 abundance does not correlate with SV2A's function (Nowack et al., 2010). Further studies are underway to determine how the SV2A KO phenotype depends on syt1, and whether it may be rescued e.g. by chimeric variants of syt1 harboring additional trafficking motifs (Hui et al., 2009a).

Another major question regarding SV2A centers on the mechanism for the racetam antiepileptic drugs. The clinical pharmacology of levetiracetam may provide some important clues. Unlike other antiepileptic drugs, levetiracetam is not a broad-spectrum CNS depressant (Kartal, 2017), though it is as effective as the sodium-channel blocker phenytoin as a second-line treatment for status epilepticus

(Klowak et al., 2021), which indicates a rapid mechanism of action. Several investigators have found that these drugs, even at high concentrations, exert only subtle effects on neurotransmitter release (García-Pérez et al., 2015; Nowack et al., 2011; Yang et al., 2015). A role for levetiracetam in changing the trafficking of SV proteins, particularly under the conditions of SV2 overexpression, has also been proposed (Nowack et al., 2011). It is thus possible that racetam antiepileptics stabilize particular conformations of SV2A with altered protein-protein interaction profiles to disrupt SV protein trafficking, which may have selective importance during epileptic activity. Alternatively, racetam antiepileptics may stabilize conformations of SV2A that have alternative, inhibitory functions at the nerve terminal, such as ionic conductances. It is not uncommon for transporters to function as ion channels, e.g., the $Cl^-$ conductance of the vesicular glutamate transporter (Eriksen et al., 2016). These effects may then depend on accumulation of SV2A in the plasma membrane, which may happen selectively under epileptic conditions. Further studies may rigorously establish whether any of these mechanisms contributes to the anti-epileptic effect of levetiracetam and brivaracetam, which remains one of the outstanding mysteries of clinical neuroscience.

Finally, it is important to affirm that the amino acid sequence of SV2A strongly suggests some type of recognition and/or transport function for ions or small molecules. Multiple independent lines of work have suggested glycobiological roles for SV2A, including the transport of galactose in yeast (Madeo et al., 2014) and the binding of fucose-α(1,2)-galactose motifs (Wibowo et al., 2014). While sugar transport and protein glycosylation are key for protein and membrane trafficking in the secretory pathway, only a few studies have begun to characterize these processes at the nerve terminal (Boll et al., 2020; Bosmann, 1972), and it remains possible that SV2A may support exocytosis through biochemical pathways that remain to be defined. It is also possible that SV2A may carry out multiple important functions, such as both molecular transport and trafficking, of which only a fraction may influence synaptic transmission.

## Tables and Figures

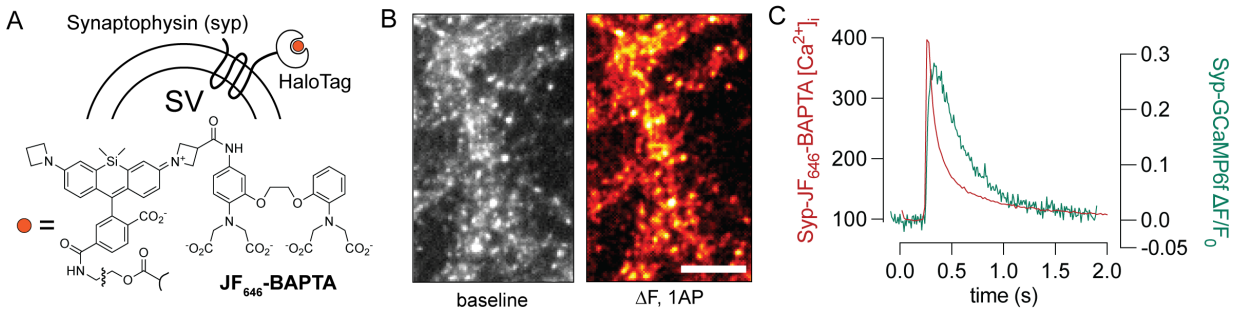


**Fig. 1. A chemogenetic sensor for presynaptic $Ca^{2+}$.** (A) $Ca^{2+}$ sensor scheme. The HaloTag protein was targeted to nerve terminals by expression as a fusion construct with the SV protein synaptophysin. $JF_{646}$-BAPTA bearing a HaloTag chloroalkane ligand was added to the bath in AM ester form and allowed to undergo fluorogenic binding to Syp-HaloTag. (B) The reaction yields Syp-HaloTag-$JF_{646}$-BAPTA, a $Ca^{2+}$ sensor with bright resting fluorescence that matches the expected punctate distribution of synaptophysin labeling and readily reports presynaptic $Ca^{2+}$ fluxes from single action potentials. (C) Comparison between Syp-HaloTag-$JF_{646}$-BAPTA and Syp-GCaMP6f, a high-performance genetically encoded presynaptic $Ca^{2+}$ sensor, demonstrates the enhancement in signal:noise and temporal fidelity afforded by the chemogenetic approach shown here. Estimated $[Ca^{2+}]_i$ was determined using a dye-saturating stimulus train following the single action potential shown here (see Methods).

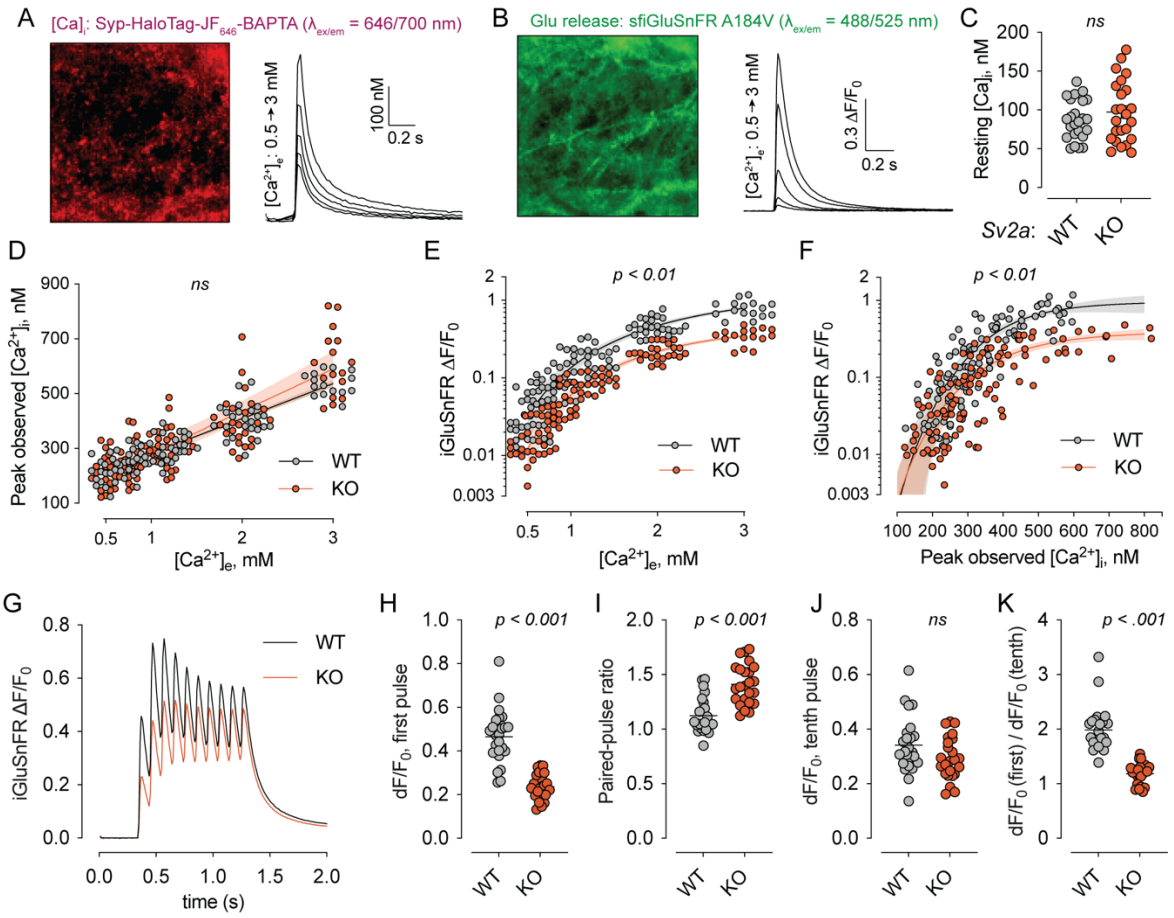


**Fig. 2: SV2A supports release probability independently of presynaptic $Ca^{2+}$.** (A) Representative field of view for Syp-HaloTag-$JF_{646}$-BAPTA (left) and fluorescence responses in that field of view from single action potentials triggered at increasing $[Ca^{2+}]_e$. (B) The same field of view as in (A) was imaged in the GFP channel, showing the plasma-membrane localized iGluSnFR construct (left) and corresponding fluorescence responses from action potentials triggered at increasing $[Ca^{2+}]_e$ (right). (C) Resting $[Ca^{2+}]_i$ at 2 mM $[Ca^{2+}]_e$ did not differ between SV2A WT and KO neurons ($p > 0.4$, Mann-Whitney test). (D) Peak $[Ca^{2+}]_i$ was plotted for each field of view at each $[Ca^{2+}]_e$ examined. $[Ca^{2+}]_i$ was calculated using a normalization procedure after applying an indicator-saturating stimulus at the end of each experiment. (E) iGluSnFR responses were plotted against $[Ca^{2+}]_e$ for each field of view.. Lines show the fit using a cooperative binding model with a Hill coefficient of ~2.3. (F) iGluSnFR responses were plotted against peak $[Ca^{2+}]_i$ for each field of view. Lines show the fit of a cooperative binding model with Hill coefficient of ~4. In panels (E) and (F), no difference in the $[Ca^{2+}]_e$ (E) and $[Ca^{2+}]_i$ (F) at which glutamate release was half-maximal was observed for the WT and KO. The value of the Hill coefficient likewise did not differ between WT and KO. *P* values for panels (E) and (F) are given as the probability that two separate curves are required to fit the data as determined via the Aikike Information Criteria. For the data showin in panel (E), SV2A KO neurons released less glutamate per action potential at all $[Ca^{2+}]_e$ values studied ($p < 0.0001$, Mann-Whitney test). (G) Averaged iGluSnFR signals from SV2A WT and KO neurons in response to 10-AP, 10-Hz stimulus trains. (H-I) Parameters describing short-term plasticity calculated from each stimulus train response and plotted. The exocytosis deficit in SV2A KO neurons normalized over the course of the stimulus train, indicating that SV2A acts to support initial release probability. In panels (H-I), values stated indicate results of Mann-Whitney tests (*ns*, $p > 0.08$). For panels (A-F), $n = 16$-24 fields of view from 2-3 neuronal cultures; for panels (H-K, $n = 24$ fields of view from 2 neuronal cultures.

**Methods**

***Cell culture and lentiviral transduction*** P0-P2 newborn mouse pups from $SV2B^{-/-}$, $SV2A^{+/-}$ breeders were genotyped prior to dissection. Hippocampal formations from $SV2A^{+/+}$ and $SV2A^{-/-}$ pups were obtained by microdissection and kept in Hibernate-A until the completion of dissection, at which point they were incubated with trypsin-EDTA (Corning, 0.25%) for 30 minutes at 37 ºC with periodic agitation. Trypsin was then replaced with plating medium (DMEM +10% FBS) and tissue was triturated 10-20 times with a 1 ml pipette before plating at ~100,000 cells/$cm^2$ (two pups per 12-well plate) onto poly-D-lysine coated glass coverslips. Plating medium was replaced with complete growth medium (Neurobasal-A medium supplemented with B-27 (1X, Gibco) and Glutamax (1X, Gibco) after 1 hour. Lentivirus encoding iGluSnFR A184V and lentivirus encoding GAP43-jRGECO1a P2A synaptophysin-HaloTag were added on 5DIV.

***Molecular biology and lentiviral preparation*** A modified iGluSnFR A184V bearing endoplasmic reticulum and Golgi export signals (Bradberry et al., 2020) was subcloned into the FUGW transfer plasmid under the synapsin promoter. GAP43-jRGECO1a (Dana et al., 2016) P2A synaptophysin-HaloTag was generated by overlap extension PCR. DNA sequences were subcloned using the In-Fusion cloning system (Takara) into the FUGW lentiviral transfer plasmid (Addgene plasmid #14883, a gift from Dr. David Baltimore) modified to include the human synapsin promoter. Lentivirus was generated by $CaPO_4$-mediated cotransfection of HEK293-T cells with transfer plasmid and the helper plasmids pCD/NL-BH*ΔΔΔ (Addgene plasmid #17531, a gift from Dr. Jakob Reiser) and pLTR-G (Addgene plasmid #17532, a gift from Dr. Jakob Reiser) followed by concentration of virus-bearing supernatant by ultracentrifugation as described (Kutner et al., 2009). The GAP43-jRGECO1a P2A Syp-Halo construct was used because we observed more even and widespread expression of Syp-HaloTag with this construct than with constructs expressing Syp-HaloTag alone. Fluorescence from GAP43-jRGECO did not interfere with glutamate or $Ca^{2+}$ measurements, nor did it affect the well-described SV2 KO phenotype of reduced glutamate release (**Fig. 1**).

***Glutamate and $Ca^{2+}$ imaging*** Neurons (15-18DIV) were washed twice with an artificial cerebrospinal fluid (ACSF) containing (in mM) NaCl 128, KCl 2.5, MgCl 1, $CaCl_2$ 1.2, HEPES 25, glucose 30 and incubated for 20 minutes at 37 ºC in the same ACSF containing $JF_{646}$-BAPTA-HTL-AM (a gift from Dr. Luke Lavis, Janelia Research Campus). $JF_{646}$-BAPTA-HTL-AM was aliquoted as a 1 mM stock in anhydrous DMSO. For each experiment, an aliquot was diluted to 100 µM in anhydrous DMSO, and 1 µl of this diluted solution was added to 550 µl ACSF immediately prior to this incubation. After incubation with dye, the coverslip was washed (3 x 1 ml) and incubated for 20 more minutes at 37 ºC in dye-free ACSF before being mounted in an imaging chamber with platinum electrodes (Warner Instruments). Imaging was carried out with a 40X 1.4 NA objective on an inverted epifluorescence microscope (IX81, Olympus) equipped with CMOS camera (Orca Flash 4.0 V2, Hamamatsu), motorized stage (Mad City Labs), and a custom illumination source containing three LEDs (470 nm, 530 nm, 625 nm) (Thorlabs). The system was controlled using Micro-Manager (Edelstein et al., 2010). Stimulus pulses (100V, 0.5 ms) were delivered with a stimulation box (SD9, Grass) controlled via a HEKA EPC 10 DAQ-amplifier and PatchMaster software, which was also used to synchronize the start of image sequence acquisition. For iGluSnFR measurements, the 470 nm LED, a standard GFP filter set (49002, Chroma) and a 10 ms exposure time was used, while $JF_{646}$-BAPTA signals were acquired using the 625 nm LED, custom 3-band pass dichroic mirror (Chroma) and far-red emission filter with a 20 ms exposure time. Images were collected using binning at 2x2 (0.325 µm pixels, Fig. 1) or 4x4 (0.65 µm pixel size, Fig. 2). For each coverslip, four fields of view were selected, and each field of view was imaged sequentially for glutamate release and presynaptic $Ca^{2+}$ entry, with at least 15 seconds allowed between stimuli. This was repeated for each field of view for each ACSF solution containing varying $CaCl_2$, and the motorized stage was used to return to the same 4 fields of view for all external solutions. At the end of each experiment, each field of view was subjected to a saturating stimulus (100 AP @ 50 Hz) while imaging Syp-HaloTag-$JF_{646}$-BAPTA to establish a maximum fluorescence ($F_{max}$) for that field of view, which was used to derive $[Ca^{2+}]_i$ values (see below). Given the expected presynaptic localization of Syp-HaloTag-$JF_{646}$-BAPTA, the fluorogenic properties of the complete HaloTag-bound $Ca^{2+}$ sensor (Deo et al., 2019) the dense

expression of this marker, and the difficulty of obtaining the exact focal plane for each $Ca^{2+}$ condition, image sequences were analyzed as entire fields of view. For the data shown in Fig. 2 panels (H-K), no $Ca^{2+}$ sensing constructs were expressed, and coverslips were simply transferred from the incubator to the microscope and equilibrated at room temperature for at least 5 minutes before recording. At least 4 minutes were allowed between stimulus trains.

***Data analysis*** iGluSnFR image sequences were converted to $\Delta F/F_0$ traces after background subtraction using custom-written scripts in FIJI and R. Syp-Halo-$HF_{646}$-BAPTA traces were background-subtracted, and the $F_{max}$ for each field of view was used to derive $[Ca^{2+}]_i$ using the following equation (de Juan-Sanz et al., 2017; Maravall et al., 2000):

$$[Ca]_i = K_d \left( \frac{{}^{F}/_{F_{max}} - {}^{1}/_{R_f}}{1 - {}^{F}/_{F_{max}}} \right)^{1/n}$$

Where $K_d$ is the dissociation constant of the indicator, $F_{syp}$ is the average fluorescence across all ROI's in the field of view, $R_f$ is the dynamic range of the indicator, and $n$ is the Hill coefficient. For $K_d$, $R_f$, and $n$, we used *in vitro* measurements from Deo et al. (2019). Data for glutamate release versus $Ca^{2+}$ were plotted and fit in Prism (GraphPad) using a cooperative binding equation with Hill slope.

# Chapter 5: Ultra-purification of brain synaptic vesicles


## Summary

Synaptic vesicles (SVs) are the fundamental packets, or quanta, of rapid neurotransmission. Much remains to be learned about the processes underlying their function, particularly how SVs are assembled from precursors and how molecular interactions shape this process. A rate-limiting step in these studies is the isolation of pure SVs, which usually requires specialized materials and up to >24 hours. Here, a robust method is described for rapid isolation of native SVs using the widely available rho1D4 monoclonal antibody. Rho1D4-coated beads rapidly immunoprecipitate SVs from a mouse brain supernatant, and elution of the beads with the 9-mer 1D4 peptide readily affords native vesicles >10-fold purer than with classical techniques in <1/10$^{th}$ the amount of time. We employ 1D4-IP to show that, in contrast to chromaffin granules and some peripheral nerve endings, ATP is not an abundant cargo of rodent brain synaptic vesicles.


## Introduction

The current state-of-the-art procedure for isolating free synaptic vesicles (SVs) relies on the size, physical properties, and abundance of these protein-rich organelles (Ahmed et al., 2013). Based on techniques developed in the 1960s (Nagy et al., 1976; Whittaker et al., 1964), this approach takes approximately 24 hours and involves gradient centrifugation and pelleting vesicles at high speed prior to size exclusion chromatography. The chromatography media typically used for the final size-exclusion step, controlled pore glass (CPG) or Sephacryl S-1000, are no longer widely available, and these preparations are unavoidably contaminated with other cellular components (Ahmed et al., 2013). Other approaches for SV purification, in which rapid purification of SVs is achieved by immunoprecipitation, have been limited by elution steps that damage or destroy the resin-bound vesicles (Burger et al., 1989; Chantranupong et al., 2020; Takamori et al., 2000b). These techniques have been valuable in determining SV membrane composition (Takamori et al., 2006), neurotransmitter content (Burger et al., 1991, 1989; Chantranupong et al., 2020), and transport activity (Burger et al., 1989, 1991; Takamori et al., 2000b).

However, each of these approaches also requires highly specialized materials, such as custom antibodies or mice expressing exogenous genes. Investigators seeking deeper insights into the biogenesis, composition, and function of SVs would be substantially aided by gentler, more selective, and more convenient procedures for their isolation. Here, a method is presented for SV purification that yields vesicles >10 times purer than with classical techniques in $<1/10^{th}$ the amount of time using readily available reagents. We provide an example of its application, demonstrating that mouse brain synaptic vesicles contain, on average, fewer than 50 molecules of ATP.

**Results**

During exploratory metabolomic studies of SVs, we were surprised by preliminary findings (not shown) that beads bearing the rho1D4 monoclonal antibody (mAb) could immunoprecipitate synaptic vesicle proteins from a mouse brain supernatant (35,000 x g, 20 minutes) containing soluble proteins and light membranes (Burger et al., 1989). We thus performed pulldown experiments comparing rho1D4 to monoclonal antibodies against the ubiquitous SV proteins synaptotagmin-1 (syt1) and SV2A (**Figure 1A**). When coupled to 2.7-µm diameter nonporous magnetic beads, each antibody precipitated a similar subset of proteins (**Fig. 1B**). For each antibody immunoprecipitate, the protein bands observed on reducing SDS-PAGE corresponded well to those observed in previous studies of SVs isolated by either conventional means or immunoprecipitation (Ahmed et al., 2013; Burger et al., 1989; Jahn et al., 1985) (**Fig 1B**). In particular, a dominant band at 38 kDa, representing synaptophysin, was observed, along with strong bands around 65 kDa, representing Syt1 and vesicular transporters, and 18 kDa, representing synaptobrevin (**Fig**. **1C**). Among the antibodies used here for IP, the anti-SV2 antibody precipitated synaptic vesicles most efficiently, likely due to higher affinity for SVs versus the other antibodies. The minor differences in protein content observed could, in part, be attributed to differences in the molecular weights of antibody fragments eluted by SDS. In each case, the bead-bound fraction was highly enriched in synaptic vesicle proteins and largely devoid of contaminants from mitochondrial or plasma membranes (**Fig. 1C**).

Fluorescence HPLC analysis of polar amines eluted from the beads demonstrated the near-exclusive presence of glutamate and GABA, as expected for pure synaptic vesicles isolated at 0 ºC (**Fig. 1D**) (Burger et al., 1991; Chantranupong et al., 2020). These data likewise indicate the absence of intact lysosomes or mitochondria, which contain many other polar amines (Abu-Remaileh et al., 2017; Chen et al., 2016). Beads coated with pooled bovine IgG did not immunoprecipitate SV proteins or vesicular amino acids (**Fig. 1B-D**). Reassuringly, the amount of neurotransmitter immunoprecipitated by each antibody correlated well with the yield of synaptophysin, confirming that these antibodies pull down a similar set of vesicles despite differences in affinity for SVs (SV2 > syt1 > rho1D4) (**Fig. 1 E-F**). The rho1D4 monoclonal antibody is thus comparable to antibodies against established SV proteins for rapid immunoprecipitation of a general SV sample.

The rho1D4 mAb was originally isolated after immunization of mice with bovine retinal membranes (Molday and MacKenzie, 1983). We note that many monoclonal antibodies named "1D4" have been described in the literature, and thus refer to this antibody as rho1D4. This antibody was determined to bind to the C-terminus of bovine rhodopsin in a manner allowing competitive peptide elution (MacKenzie et al., 1984). The 9-mer 1D4 peptide sequence (TETSQVAPA) has been commercialized as C-terminal affinity tag, and the free 1D4 peptide gently elutes rho1D4 mAb-bound targets under native conditions (Wong et al., 2009).

We thus assessed the effects of incubating rho1D4 bead-bound SVs with the 1D4 peptide. A single incubation of SV-bearing rho1D4 beads with 200 uM 1D4 peptide eluted a substantial fraction of the bead-bound protein (**Fig. 2A**). This eluate, which typically contained ~20 ng/ul protein but a concentration of synaptophysin ~2-fold that of the 3.5 mg/ml input fraction **(Fig 2A**), represents an enrichment of vesicular protein by over 300-fold (**Table 1**). By contrast, classical techniques typically report a synaptophysin enrichment of ~20-fold (Ahmed et al., 2013). Examination of this eluate by dynamic light scattering demonstrated a population of particles 40-60 nm in diameter (**Fig. 2B**). Negative-stain transmission electron microscopy (TEM) of these samples likewise demonstrated population of vesicular structures 40-60 nm across, studded with ~8-nm tall structures that likely represent the V1

sector of the V-ATPase (**Fig. 2C**). 1D4-eluted vesicles were also free of the residual, bead-adsorbed antibody that inevitably eluted with SDS (**Appendix – Fig S1**). 1D4 immunoprecipitation and elution thus enables the rapid (< 2 hr) isolation of an exceptionally pure SV sample without contamination from antibodies or exposure to harsh physical or chemical conditions. Vesicles can readily be eluted in volatile buffers such as ammonium acetate to facilitate downstream analyses. If native vesicles are not needed, harsh elution of the beads provides a favorable compromise of purity for yield (**Table 1**).

It is clear in **Fig. 1** that several bands are enriched in the rho1D4 immunoprecipitate relative to the anti-Syt1 and anti-SV2 material. Because it is likely that one of these proteins is the SV antigen bound by the rho1D4 mAb, studies are underway to determine their identity (see Future Directions).

1D4-IP was applied to definitively answer the question of whether brain synaptic vesicles contain adenine nucleotides. The presence of adenine nucleotides in secretory vesicles is common, with notable examples including chromaffin granules (Douglas and Poisner, 1966; Zhang et al., 2019) and nerve terminals of the autonomic nervous system (Ren et al., 2003), but the role of vesicular nucleotides in the brain is less clear. A recent SV metabolomic study (Chantranupong et al., 2020) did not report the detection of adenine nucleotides in a rapidly prepared SV sample, though it is unclear what the limit of detection for these molecules was in that study. Because the presence of nucleotides as ubiquitous vesicular cargoes has been suggested by a number of studies (Estévez-Herrera et al., 2016; Larsson et al., 2012; Sawada et al., 2008), we sought to address the matter directly by analysis of 1D4-immunoprecipitated vesicles. Adenine nucleotides were detected by fluorescence HPLC after etheno-derivatization with chloroacetaldehyde (**Fig. 3A**) (Levitt et al., 1984). In agreement with previous work (Chantranupong et al., 2020) we did not detect large quantities of adenine nucleotides in brain SVs (**Fig. 3B-C**). Analysis of SV samples spiked with ATP demonstrated a robust response with 1 pmol ATP in the sample, which corresponds to ~60-100 molecules of ATP per vesicle, or 15 mM ATP in vesicles assuming a volume of 20 zL (**Fig. 3B**). While the possibility remains that adenine nucleotides may be weakly concentrated (< 5 mM) in most SV's, or highly concentrated in a subset of vesicles, our results argue against a role for ATP as a widespread, concentrated vesicular cargo in mammalian brain.

1D4-IP was next applied to the study of protein glycosylation in synaptic vesicles. The abundant SV proteins synaptophysin, synaptotagmin, and SV2 are *N*-glycosylated, and glycosylation is essential for the trafficking of most of these proteins. However, a direct role for glycans in the synaptic vesicle cycle has not been established. Furthermore, while glycosylation is critical to protein biogenesis in the early secretory pathway, the fates of glycans on proteins that accumulate far away from the cell body, in neuronal processes, are largely unknown. Classical studies suggest the presence of enzymes for cleavage and extension of glycans at nerve terminals, and a recent study has suggested that sialylation is depolarization-responsive process in synaptosomes. Maturation of *N*-linked glycans is essential for dense core vesicle targeting in PC12 cells. Some studies point to a role for galectin, a galactose-binding protein, in clathrin-independent exocytosis, which plays an important role at the synapse. However, while some studies have been performed to assess glycosylation in dissected brain tissue, the cell-type-specific and organelle-specific glycosylation patterns in the brain are also largely undefined.

We thus analyzed the *N*-linked glycans of 1D4-immunoprecipitated SVs using derivatization, enzymatic digestion and fluorescence HPLC analysis (**Fig. 4**). Beads were eluted with detergent, subject to *N*-linked glycan removal by PNGase F, and the glycans were labeled with procainamide by reductive amination (**Fig. 4A**). After desalting, the labeled glycans were subject to structure characterization by treatment with specific enzymes followed by HILIC-HPLC with fluorescence detection. As an example, the *N*-linked glycans of the rho1D4 antibody were sequenced in this manner (**Appendix – Fig S2**), which may aid in reproducibility of rho1D4 reagents in the future. Analysis of *N*-glycans from SVs (**Fig. 4B**) revealed three striking characteristics:

**Discussion**

Our results demonstrate that the rho1D4 mAb specifically binds a synaptic vesicle antigen, and that this interaction is well-suited for affinity purification of native SVs from mammalian brain. The entire process, from homogenization to elution, takes less than two hours. Ultracentrifugation, density gradients, and size-exclusion chromatography are avoided, and the vesicles are not pelleted at any point.

Critically, the materials required for 1D4 immunoprecipitation are chemically definable, relatively inexpensive, and readily available to investigators. A single P10-P20 mouse brain (0.3-0.4 g) comfortably provides enough material for two IP experiments (3 mg Ab-Dynabeads each) including protein and neurotransmitter analyses (**Fig. 1**). The preparation can easily be scaled up, but satisfactory results may also be obtained with substantially smaller amounts of starting material, depending on the target of analysis. At present, it is unclear which protein or proteins mediate the SV-rho1D4 interaction, but efforts are ongoing to clarify this matter (see Chapter 6: Future Directions).

In comparison to classical techniques (Ahmed et al., 2013; Nagy et al., 1976; Whittaker et al., 1964), the yield of a typical 1D4-IP experiment is lower, but the final product is of >20-fold higher purity (with peptide elution), and the procedure is completed in ~$1/10^{th}$ the amount of time. Thus, unlike classical techniques, 1D4-IP is well-suited to the isolation of SVs containing native neurotransmitter and intact assemblies of multi-subunit complexes such as the v-ATPase, which may disassemble during prolonged purification steps (Bodzęta et al., 2017; Kane, 1995). For most functional and biochemical studies, the presence of the 1D4 peptide should not interfere, but the free peptide may be removed from eluted SVs using ultrafiltration or size-exclusion chromatography if needed. For applications not requiring native elution, the performance of the anti-syt1 and anti-SV2 antibodies (**Fig. 1**) indicate that immunoprecipitation is generally favorable to classical fractionation techniques for the analysis of SVs.

In comparison to the recently-described SV-tag approach (Chantranupong et al., 2020), 1D4-IP of vesicles does not afford genetic specification of the target vesicles, but introduction of exogenous epitopes by transgenic breeding approaches or viral transduction is not required. Compared to SV-tag and other reported immunoprecipitation approaches (Burger et al., 1989; Takamori et al., 2000b, 2000a), 1D4-IP has the advantage of native vesicle elution.

We emphasize the purity and native state of the peptide-eluted SV product, which is enriched >300-fold for synaptophysin and represents a new gold standard for the synaptic vesicle preparation (**Table 1**). Modern mass spectrometry methods allow semi-quantitative analysis of whole proteomes with < 1 ug of total peptide analyte, and the reduced yield of 1D4-IP compared to classical techniques is

unlikely to pose a major technical hurdle for such studies. Recent ultra-high-definition proteomic studies using classically prepared SVs have described a synaptic vesicle proteome containing >1600 proteins (Taoufiq et al., 2020). Deeper mass spectrometric characterization of rho1D4 immunoprecipitates, which are at least 10- to 20-fold purer, will thus likely yield further insights into synaptic vesicle biology. Future experiments may also employ these vesicles in functional assays for, e.g., neurotransmitter transport or membrane fusion.

Our results provide clarity to the long-standing question of whether ATP is a widespread co-transmitter in brain synaptic vesicles. The concentration of ATP in presynaptic cytoplasm is 1-1.5 mM (Rangaraju et al., 2014), and our results indicate that brain synaptic vesicles do not concentrate ATP much beyond this (**Fig. 3**). While the presence of ATP in some secretory vesicles has led to the hypothesis that ATP is also a widespread vesicular cargo in brain (Larsson et al., 2012; Sawada et al., 2008), electrophysiological studies have indicated that ATP likely plays a minor role and is released distinctly from both glutamate and GABA (Pankratov et al., 2006). Our results are consistent with the latter interpretation and agree with recent metabolomic studies of synaptic vesicles (Chantranupong et al., 2020). However, our results do not rule out a modulatory role for adenine nucleotides in the central nervous system, particularly as a gliotransmitter (Lalo et al., 2014; Pougnet et al., 2014). Additionally, because at least some neuroendocrine cells in the periphery use adenine nucleotides as vesicular transmitters (Ren et al., 2003; Zhang et al., 2019), a small subset of central nervous system synapses, e.g. in the lateral habenula (Robertson and Edwards, 1998) may rely on such molecules for fast synaptic transmission.

The robustness and convenience of 1D4-IP reagents represent a major improvement in the accessibility of the brain synaptic vesicle preparation. We anticipate that 1D4-IP will enable substantial progress among structural, chemical, and functional studies of SVs. These organelles contain both proteins and lipids involved in synaptic signaling, and they require functioning, metabolically active axonal processes. By enabling preparation of analytical quantities of SVs from small amounts of starting

material, 1D4-IP may expand the use of SV analysis in the study of normal and disease-related brain processes, such as aging, neuroinflammation, and metabolic disease. We speculate that 1D4-IP may allow for isolation of SVs directly from human tissue samples, though further study is required to determine the species specificity of the rho1D4-SV interaction. Finally, it remains to be seen whether the rho1D4 mAb may precipitate other organelles, proteins, or whole cells from other tissues and bodily fluids.

## Tables and Figures

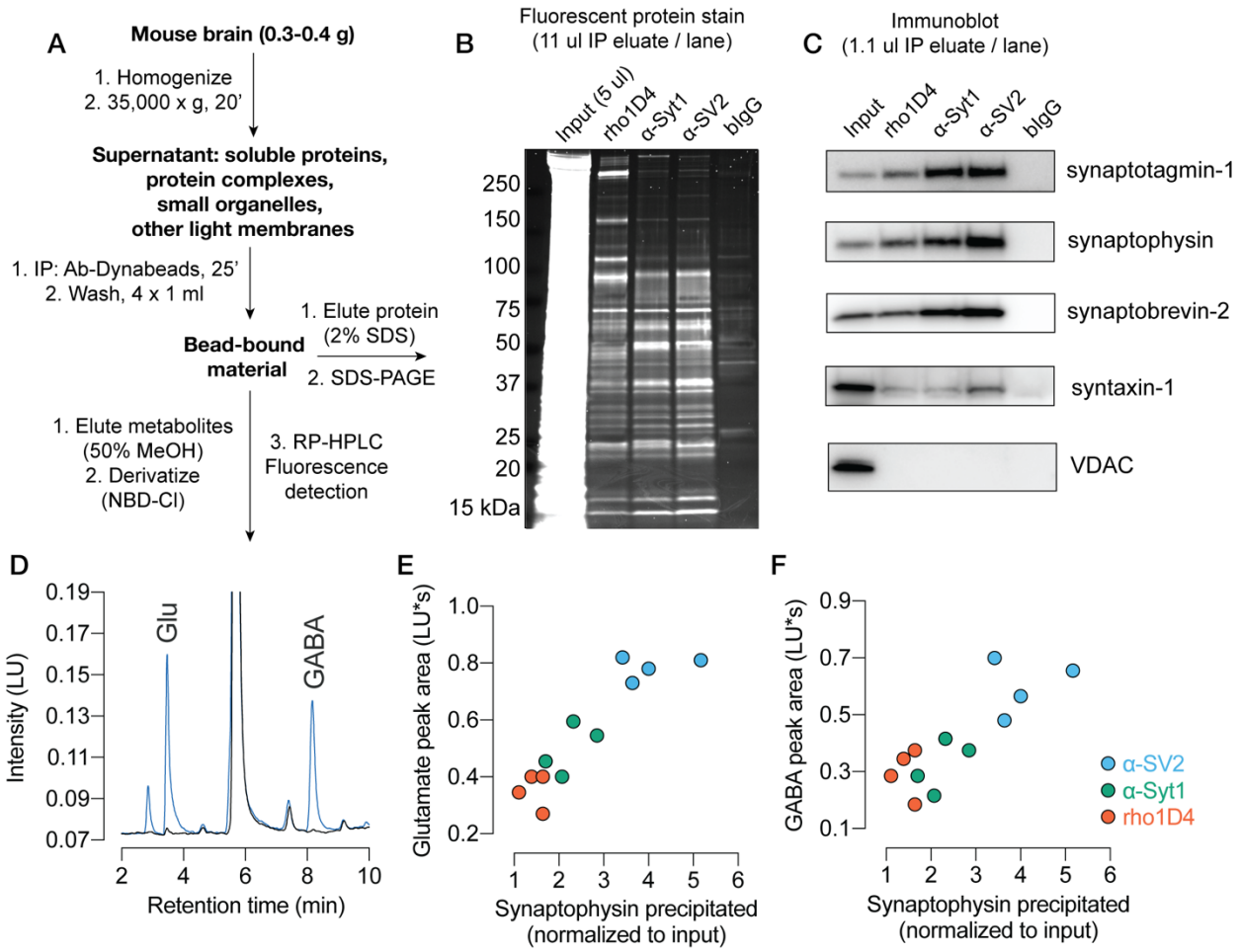


**Fig. 1** The rho1D4 mAb immunoprecipitates synaptic vesicles,. (A) Scheme for vesicle immunoprecipitation and analysis. Each mouse brain provided sufficient material for analysis of protein and neurotransmitter using two different mAbs. (B) Staining of proteins separated by SDS-PAGE demonstrates broad similarity among anti-SV2, anti-Syt1, and rho1D4 immunoprecipitates, with minimal protein binding by control beads bearing pooled bovine IgG. Note the dominant band at 38 kDa, corresponding to synaptophysin (C). Western blot analysis of immunoprecipitated material. Each antibody yields strong enrichment of synaptic vesicle proteins, but not proteins associated with mitochondria (VDAC) or the plasma membrane (syntaxin-1). (D) Representative HPLC fluorescence traces for NBD-derivatized amines obtained by eluting the beads with 50% methanol. Peak identities were determined by running glutamate and GABA standards. Blue trace corresponds to eluate from α-SV2 Dynabeads, and black trace corresponds to eluate from bIgG Dynabeads. (E) For each experiment, the area of the HPLC peak corresponding to glutamate was plotted against the normalized intensity of the synaptophysin band on immunoblot. (F) As in (E) but for the HPLC peak corresponding to GABA. For panels E and F, $n = 4$ experiments using 2 separately prepared batches of Ab-Dynabeads for each mAb, from which representative examples were used for panels B-D.

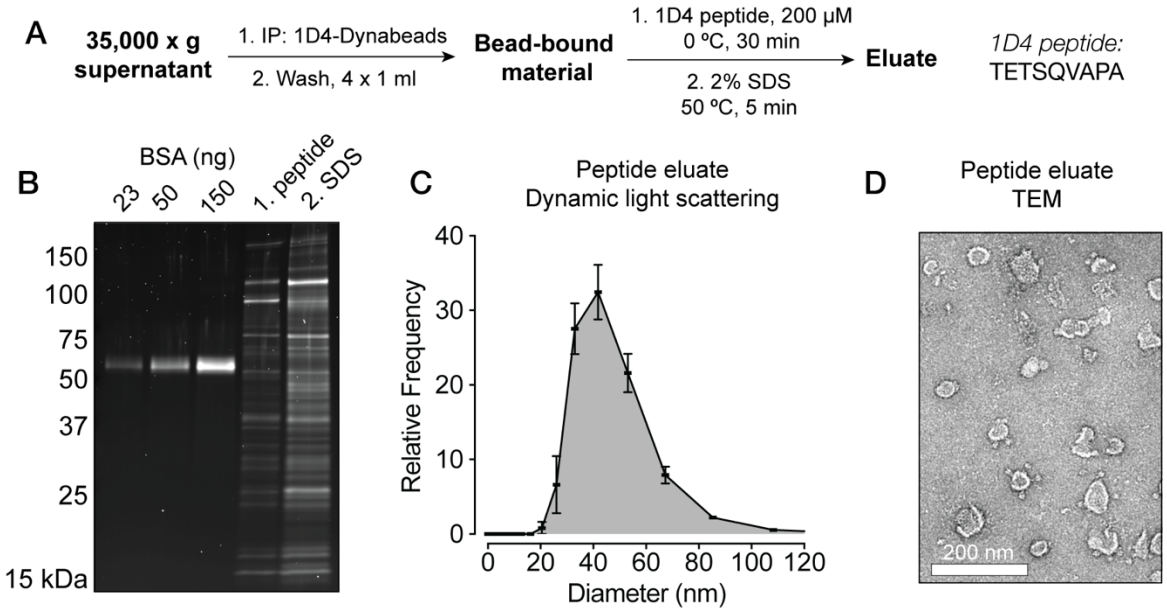


**Fig. 2** Native synaptic vesicles are readily eluted from rho1D4-coated magnetic beads. (A) Purification scheme for 1D4-IP. The amino acid sequence of the 1D4 peptide sequence is shown. (B) SDS-PAGE with fluorescent stain of protein eluted from rho1D4 beads using the 1D4 peptide. Synaptic vesicle proteins were readily eluted from the beads. (C) Dynamic light scattering measurements (n = 3 biological replicates) of eluted material indicates a single population of particles ca. 50 nm in diameter. This population represented 99% of particles detected in the sample. (D) Negative-stain transmission electron microscopy of 1D4-eluted material demonstrates vesicles of the appropriate size with minimal contamination by non-vesicular structures.

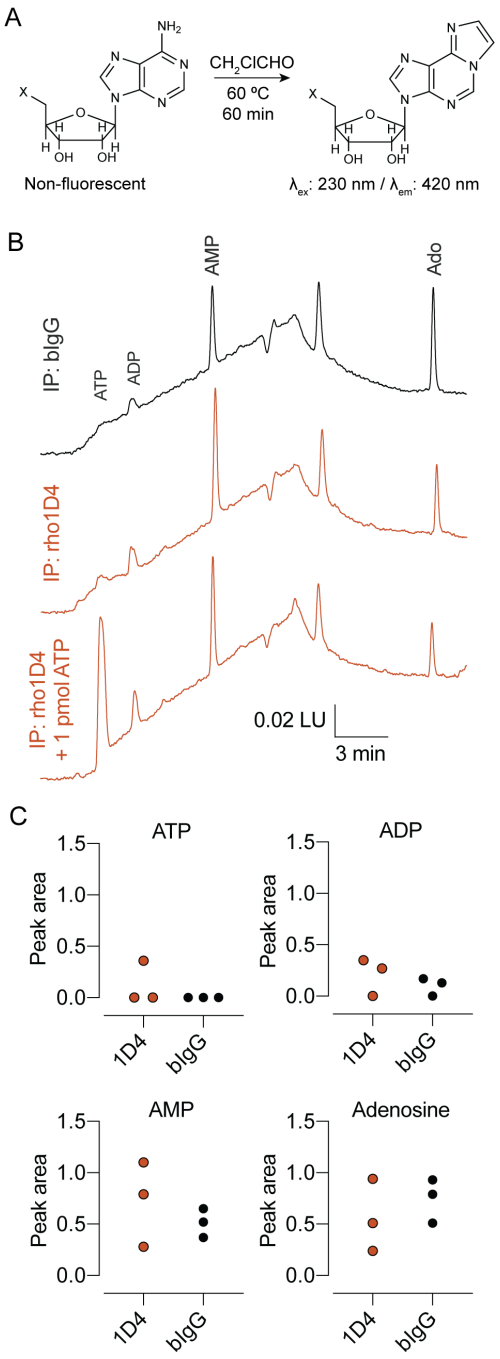


**Fig. 3**: Adenine nucleotides are not highly concentrated in SVs. (A) Scheme for derivatization of adenine compounds. Reaction with chloroacetaldehyde generates fluorescent etheno-adenine products that can be separated by HPLC. (B) Example HPLC fluorescence traces of samples prepared from bIgG and rho1D4-bearing magnetic beads. The bottom trace shows the same eluate spiked with 1 pmol ATP (50 fmol on column), corresponding to ~50-100 molecules of ATP per vesicle (~15 mM inside the vesicle). Peak identities were established using authentic standards. (C) The peaks for each adenine compound were integrated and plotted ($n$ = 3 biological replicates using two batches of beads). While a trend toward greater nucleotide content was observed for rho1D4 immunoprecipitates, this value was either near the limit of detection (ATP, ADP) or close to the background observed with negative control bIgG beads (AMP, adenosine).

| Fraction | Volume, ul | [protein], ng/ul | [synaptophysin], ng/ul | Enrichment factor | Percentage of input synaptophysin | Preparation time, hours |
|---|---|---|---|---|---|---|
| Input (1/2 mouse brain) | 2000 | 3500 | 0.6 | 1 | 100% | < 0.5 |
| Bead-bound material | 50 | 100 | 3.1 | 181 | 13% | < 1.5 |
| 1D4 peptide eluate | 50 | 20 | 1.4 | 408 | 6% | < 2 |
| SV fraction via classical methods (Ahmed et al. 2013) | *50* | *1200* | *4* | *19* | *20%* | *> 24* |

**Table 1** Quantitative comparison of 1D4-IP with classical methods. Enrichment factor is calculated as the ratio of synaptophysin to total protein by mass. The yields described in Ahmed et al. (2013) were derived using their stated enrichment factors and scaled to the amount and fraction of starting material used here (see Methods for details). Data shown represent the result of a typical experiment using 3 mg of rho1D4 coated beads.

**Methods**

***Animals*** C57B/6J mice of both sexes between 12 and 20 days of age were used for all experiments. All work was conducted according to protocols approved by the University of Wisconsin Institutional Animal Care and Use Committee.

***Antibodies for immunoprecipitation*** Mouse monoclonal anti-syt1 (mAb 48) and anti-SV2 antibodies were purified by protein G chromatography from stocks of ascites generated prior to 2010. Rho1D4 mAb was purchased from the University of British Columbia. Bovine IgG was purchased from Sigma. All antibodies were dialyzed extensively against PBS (140 mM NaCl, 10 mM sodium phosphate buffer, pH 7.4) aliquoted, and stored frozen at -20 ºC prior to bead coupling.

***Bead preparation*** Dynabeads M-270 epoxy (300 mg, Thermo Fisher 14302D) were stored as a 30 mg/ml suspension in anhydrous, amine-free DMF for up to 18 months prior to coupling. For each coupling reaction, 10 mg beads were transferred to a fresh 1.7 ml microcentrifuge tube and the DMF was removed after collecting the beads with a magnetic stand (Promega). A 250-ug aliquot of each antibody was brought up to 200 ul with borate buffer (100 mM sodium borate pH 8.5) and this was used to resuspend the beads. An additional 200 ul borate buffer was added to each tube and mixed by pipetting up and down, followed by the addition of 200 ul 3 M ammonium sulfate in borate buffer and further mixing by pipetting up and down. The reaction mixture was incubated with rotation at 37 ºC overnight. After removal of the supernatant, the beads were washed with 3 cycles of 1 ml 500 mM NaCl, 50 mM ammonium acetate pH 4.5 followed by 500 mM NaCl, 50 mM Tris-HCl pH 8.0 (6 x 1 ml washes total). The Ab-Dynabeads beads were then washed (1 x 1 ml) and resuspended at 30 mg/ml in 150 mM KCl, 50 mM Tris-HCl pH 8.0 and stored at 0-4 ºC until use. For experiments shown in Fig. 2 and Fig. 3, 150 mM KCl, 10 mM potassium phosphate buffer, pH 7.2 was used as the final wash and storage buffer, with no discernable change in performance.

***SV immunoisolation*** All buffers and equipment were cooled to 0-1 ºC prior to beginning experiments, and all operations from homogenization until bead elution were carried out in a cold room. 1-2 C57B6/J

mice were euthanized with carbon dioxide and the brains, including cerebellum and brain stem, were rapidly removed. Each brain was homogenized in 4.2 ml of homogenization buffer (125 mM KCl, 20 mM potassium phosphate buffer, 5 mM EGTA, protease inhibitors [cOmplete Mini EDTA-free, 1 tablet / 10 ml], pH 7.3 at 0 ºC) using 10 strokes in a Teflon-glass Dounce homogenizer with rotation at 850-900 RPM. The homogenate was then centrifuged (20 minutes, 35,000 x g, 1 ºC). During centrifugation, 3 mg of Ab-Dynabeads were transferred to a fresh 2 ml microcentrifuge tube, washed with 1 x 1 ml wash buffer (150 mM KCl, 10 mM potassium phosphate buffer, pH 7.2 at 0 ºC) and resuspended with 100 ul homogenization buffer. Following centrifugation, the supernatants (~3.5-4 mg/ml protein) were pooled, and 1.9 ml was added to each tube containing Ab-Dynabeads. The tubes were incubated with rotation for 25 minutes, with the temperature maintained at 0 ºC by placing the tubes inside 50-ml conical tubes packed with ice. The beads were then collected via magnetic stand, the supernatant was discarded, and the beads were washed 4 times by resuspending in 1 ml ice-cold wash buffer. In all cases, the final wash was used to transfer the beads to fresh 1.5-ml microcentrifuge tubes for elution. For Fig. 1, the beads were split into two equal portions (1.5 mg each). For protein analysis, one portion was eluted by adding 30 ul 2% SDS, 25 mM Tris pH 8.0 and heating to 50 ºC for five minutes. For polar amine analysis, the other portion was eluted by adding 30 ul of 50:50 MeOH:borate buffer and incubating on ice for 5 minutes. In Fig. 1, immunoprecipitations using all 4 Ab-Dynabead conjugates were carried out in parallel for each experiment.

***SDS-PAGE and immunoblot*** Following elution with peptide or SDS, 1/3 volume of 4x SDS sample buffer containing β-mercaptoethanol was added to the eluate, and the input fraction was prepared by mixing 30 ul brain supernatant with 60 ul 4X SDS sample buffer. Samples were reduced and denatured by heating to 50 ºC for 15 minutes and subjected to SDS-PAGE on 4-20% polyacrylamide gradient gels (Bio-Rad). For total protein analysis, 15 ul of each sample was loaded, and the gel was fixed and stained with Lumitein One-Step fluorescent protein stain (Biotium). For immunoblot, the same amount of input was run, but the IP samples were diluted 10-fold in 4X sample buffer prior to SDS-PAGE. Proteins were transferred to PVDF membranes, blocked in 5% nonfat dry milk in 150 mM NaCl, 10 mM Tris, pH 7.4

plus 0.1% Tween-20 (TBS-T), and incubated overnight with primary antibody in TBS-T containing 1% nonfat dry milk. The primary antibodies used were: mouse anti-synaptobrevin monoclonal (clone 69.1, Synaptic Systems 104 211, 1:1000 dilution of an 0.1 mg/ml stock); guinea pig anti-synaptophysin polyclonal (Synaptic Systems 101 004, 1:1000 dilution of a 0.5 mg/ml stock); mouse anti-synaptotagmin monoclonal (mAb 48, available at the Developmental Studies Hybridoma Bank, 1:1000 dilution of a 3.7 mg/ml stock purified from ascites fluid); mouse anti-syntaxin monoclonal (clone HPC-1, 1:1000 dilution of a 3 mg/ml stock concentrated from Abcam ab3265); rabbit polyclonal anti-VDAC (Millipore AB10527, 1:1000 dilution of the supplied solution). HRP-labeled secondary antibodies were used for detection. Synaptophysin band intensity was determined in ImageJ using blank adjacent lanes for background subtraction. For the protein quantification shown in Table 1, BSA standards were used to determine a ratio of fluorescence units to protein mass, and lanes containing protein material were quantified after background subtraction using an adjacent blank lane.

**Amine analysis** For experiments in Fig. 1, 8 ul of bead eluate (50:50 MeOH:borate buffer) was combined with 4 ul of derivatization solution (5 mg/ml NBD-Cl in MeOH) and heated to 60 ºC for 70 minutes on a PCR block. Samples were diluted 100-fold in 95:5 H2O:MeCN containing 10 mM ammonium acetate prior to analysis. NBD-derivatized amines were analyzed on an HPLC system (Agilent Infinity 1260 Bio-Inert) with a reversed-phase C18 column (Agilent Peptide Mapping, 2.1 x 150 mm, 2.7 um particle size) and fluorescence detector (Agilent 1260 FLD Spectra, 470 nm excitation, 530 nm emission). The instrument was operated using a manual injector, the column was kept at 40 ºC, and samples were applied to overfill a 5-ul sample loop. Mobile phase A was 95:5 $H_2O$:MeCN containing 10 mM ammonium acetate, mobile phase B was 95:5 MeCN:$H_2O$ containing 5 mM ammonium acetate. For Fig. 1, GABA and glutamate were separated using an optimized gradient as follows: 0-20 minutes, 10%-100% B; 20-25 minutes, 100% B; 25-30 minutes, 100%-10% B. Peak identities were confirmed by running authentic standards, and areas were determined by integration in Agilent Chemstation software.

**Adenine nucleotide analysis** Beads (1-3 mg from a total of 3 mg used for IP) were eluted by incubation with 50% methanol on ice for 5 minutes (20 ul/mg beads). 10 ul of eluate was combined with 2 ul 1 M ammonium acetate buffer pH 4.0, 1 ul of 50% aqueous chloroacetaldehyde solution, and for some samples, 1 ul of ATP standard containing 1 pmol ATP. Concentrated chloroacetaldehyde was kept in a fume hood during all handling steps. The reaction mixture was heated to 60 ºC for 60 minutes on a PCR block, then diluted tenfold with water containing 100 mM potassium phosphate buffer, pH 6.1. This mixture was analyzed by fluorescence HPLC with the same manual injector, sample loop, and C18 column (Agilent Peptide Mapping, 2.1 x 150 mm, 2.7 um particle size, thermostatted at 40 ºC) used for NBD-amine analysis. Mobile phase A was water containing 100 mM potassium phosphate buffer, pH 6.0-6.1, prepared by mixing concentrated potassium phosphate buffer stocks. Mobile phase B was 65% mobile phase A, 35% methanol by volume. Adenine nucleotides and adenosine were separated using an optimized gradient as follows: 0-35 minutes, 0%-60% B. This was followed by a wash gradient using pure $H_2O$ and MeOH prior to re-equilibration with 100% A. Peak identities were confirmed by running authentic standards for ATP, ADP and adenosine, and the peak identity of AMP was inferred by presence in ADP standard and elution time. Peak areas were determined by automatic integration in Agilent Chemstation software.

***Dynamic light scattering*** 3 ul of 1D4 peptide eluate was analyzed in a micro-cuvette on a dynamic light scattering instrument (Wyatt). For each sample, 10 acquisitions were performed, and data from those acquisitions showing good autocorrelation functions (>90% of scans) were averaged to produce a single replicate. Data corresponding to the distribution of particle sizes were exported and plotted in Prism.

**Appendix**

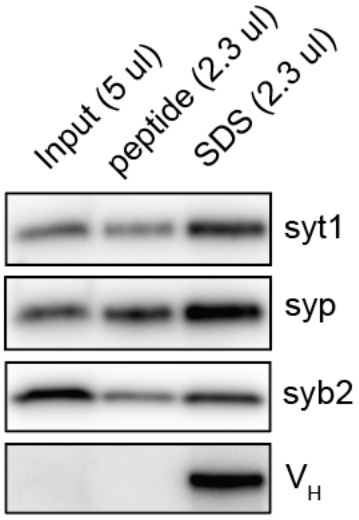


**Fig. S1:** Immunoblot of synaptic markers and the IgG heavy chain from peptide- and SDS-eluted vesicles. Rho1D4-Dynabeads were eluted sequentially with the 1D4 peptide (200 µM, 30 minutes on ice) followed by 2% SDS for 5 minutes at 50 ºC.

## Chapter 6: Future directions

The remainder of my time in Dr. Chapman's lab will be spent developing further methods for SV analysis and applying these methods to characterize the SV2A KO phenotype.

The work in Chapter 5 will be submitted in a manuscript for publication pending a few additional studies. At the very least, additional replicates are required to shore up the quantitative analysis of SV material for 1D4-IP. More excitingly, plans have been made for a mass spectrometric analysis of the immunoprecipitated material at the Human Proteomics Program at UW SMPH. This study should allow for a deeper characterization of the material and, ideally, identification of 1D4-enriched bands, giving important clues into the nature of the 1D4 binding site. Depending on the protein(s) identified, these studies may yield new insights into SV biology, as well as additional applications for the 1D4 antibody.

The primary clues towards SV2A's mechanism of action come from biochemical studies hinting at a role in glycobiological processes. SV2A has been shown to allow galactose uptake in yeast (Madeo et al., 2014) and to bind a specialized disaccharide motif, fucose-α(1,2)-galactose, presented on synthetic polymers (Wibowo et al., 2014). Another study suggested that SV2A binds adenine nucleotides and nucleosides (Yao and Bajjalieh, 2008). Unfortunately, nucleotide sugars, the primary "activated" sugars used for glycan biosynthesis, were not examined in this study. Glycobiological processes at the nerve terminal are largely uncharacterized, though they are likely dynamic (Boll et al., 2020), and classical work indicates the presence of enzymes for glycan modification in nerve terminals (Bosmann, 1973, 1972; Goodrum et al., 1979).

The provocative finding that SV2A allows yeast to survive on galactose (Madeo et al., 2014) and the identification of SV2A on a screen of fucose-α(1,2)-galactosyl binding proteins (Wibowo et al., 2014) both suggest a role in presynaptic glycobiology. Because glycosylation dynamics are key to protein synthesis, quality control, and export in the secretory pathway, it is likely that glycosylation is important for synaptic vesicle recycling. SV2A and synaptophysin, another SV glycoprotein, both require intact glycosylation sites for normal trafficking to nerve terminals (Kwon and Chapman, 2012). However, sugar dynamics at the nerve terminal itself remain under-characterized. While a recent study has shown that

sialylation in synaptosomes changes with depolarization (Boll et al., 2020), the glycosylation patterns of synaptic vesicle proteins themselves has not been rigorously established. Determining SV protein glycosylation in SV2A WT and KO neurons will thus help establish an understanding of glycan dynamics at the nerve terminal and a role for SV2A in these processes. Likewise, more in-depth chemical analysis of synaptic vesicles from SV2A WT and KO neurons may allow for an investigation into potential roles for SV2A in lipid or glycolipid metabolism. Several possible mechanistic links may exist between glycosylation and synaptic vesicle fusion, including proper sorting or assembly of vesicular proteins and, potentially, the properties of the intravesicular space (Reigada et al., 2003).

The other immediate analysis goal for purified SV's is to identify their *N*-linked glycans. As described in Chapter 4, little is known about glycobiology at the nerve terminal, and several clues suggest that SV2 may play a role in sugar-dependent processes. Because glycan modification is a dynamic process, glycosylation of synaptic vesicle proteins may reflect important aspects of presynaptic biology. In general, I plan to establish methods for SV glycan analysis and include this work with the 1D4-IP manuscript, then apply these methods to SV2 WT and KO vesicles. These analysis methods involve enzymatic cleavage of N-linked sugars and subsequent fluorescence derivatization by reductive amination at the reducing end of the free oligosaccharide. Analysis is carried out by fluorescence HPLC, with the identifies of the sugars established using standards and successive enzymatic cleavage of terminal saccharides.

Another potential approach to SV glycomics involves the purification of SV glycoproteins from detergent extracts in higher quantities than possible in SV pulldowns. The SV2 monoclonal antibody (see Chapter 3) is capable of precipitating large quantities of SV2 from brain detergent extracts, and I plan to determine the glycosylation of this material in the coming months. More sophisticated approaches may be possible in cultured neurons, e.g. with exogenous expression of the SV glycoprotein synaptophysin as an affinity-tagged construct, followed by immunoprecipitation and glycan analysis. I have established a highly robust method for small-scale affinity purification using the GFP nanobody that may be applied for this purpose.

Work to establish a glycan analysis method is ongoing. At the time of this writing, I have successfully cleaved, labeled, and detected synaptic vesicle glycans. Preliminary analyses using specific enzymatic cleavage approaches suggest that SVs bear a striking number of hybrid and high-mannose glycans, which are typically associated with early processing in the secretory pathway.

To further both the analysis of synaptic vesicles, I have made tentative arrangements to work collaboratively with Dr. Josh Coon in the Chemistry Department to perform analyses of 1D4-immunoprecipitated SV's. While these plans are still being formed, my goal is to perform mass spectrometric analyses of the proteome and lipidome of 1D4-isolated SVs, as well as of the purified and labeled vesicular N-glycans. I intend also to perform glycoproteomic analysis of purified SV2; as SV2 is a major SV glycoprotein, this analysis will shed light on the nature of synaptic vesicle glycosylation. This will also provide an opportunity for more hands-on experience with mass spectrometry and training in analytical chemistry, both of which I hope to use during my next phase of research work.

My work in the Chapman lab will probably come to a close sometime in winter 2021-22. May and June of 2021 will be occupied with clinical duties, and 2021 will be busy with psychiatry residency interviews come October. This leaves only a few months left to accomplish these goals. While the 1D4-IP project will certainly be completed in a few months, the timeline for the SV2 project is less certain. I am confident that others in the Chapman lab will be willing to collaborate on the project if needed. In any case, the role of SV2A remains one of the brain's mysteries, and I look forward to continuing work on it in the coming months and years.

**References**


Abrams, F.S., London, E., 1993. Extension of the Parallax Analysis of Membrane Penetration Depth to the Polar Region of Model Membranes: Use of Fluorescence Quenching by a Spin-Label Attached to the Phospholipid Polar Headgroup. Biochemistry 32, 10826–10831. https://doi.org/10.1021/bi00091a038

Abu-Remaileh, M., Wyant, G.A., Kim, C., Laqtom, N.N., Abbasi, M., Chan, S.H., Freinkman, E., Sabatini, D.M., 2017. Lysosomal metabolomics reveals V-ATPase- and mTOR-dependent regulation of amino acid efflux from lysosomes. Science 358, 807–813. https://doi.org/10.1126/science.aan6298

Adams, P.D., Afonine, P.V., Bunkóczi, G., Chen, V.B., Davis, I.W., Echols, N., Headd, J.J., Hung, L.-W., Kapral, G.J., Grosse-Kunstleve, R.W., McCoy, A.J., Moriarty, N.W., Oeffner, R., Read, R.J., Richardson, D.C., Richardson, J.S., Terwilliger, T.C., Zwart, P.H., 2010. *PHENIX* : a comprehensive Python-based system for macromolecular structure solution. Acta Crystallogr. D Biol. Crystallogr. 66, 213–221. https://doi.org/10.1107/S0907444909052925

Ahmed, S., Holt, M., Riedel, D., Jahn, R., 2013. Small-scale isolation of synaptic vesicles from mammalian brain. Nat. Protoc. 8, 998–1009. https://doi.org/10.1038/nprot.2013.053

Alle, H., Kubota, H., Geiger, J.R.P., 2011. Sparse But Highly Efficient Kv3 Outpace BKCa Channels in Action Potential Repolarization at Hippocampal Mossy Fiber Boutons. J. Neurosci. 31, 8001–8012. https://doi.org/10.1523/JNEUROSCI.0972-11.2011

Bai, H., Xue, R., Bao, H., Zhang, L., Yethiraj, A., Cui, Q., Chapman, E.R., 2016a. Different states of synaptotagmin regulate evoked versus spontaneous release. Nat. Commun. 7, 1–9. https://doi.org/10.1038/ncomms10971

Bai, H., Xue, R., Bao, H., Zhang, L., Yethiraj, A., Cui, Q., Chapman, E.R., 2016b. Different states of synaptotagmin regulate evoked versus spontaneous release. Nat. Commun. 7, 10971. https://doi.org/10.1038/ncomms10971

Bai, J, Tucker, W.C., Chapman, E.R., 2004. PIP2 increases the speed of response of synaptotagmin and steers its membrane-penetration activity toward the plasma membrane. Nat Struct Mol Biol 11, 36–44. https://doi.org/10.1038/nsmb709

Bai, Jihong, Tucker, W.C., Chapman, E.R., 2004. PIP2 increases the speed of response of synaptotagmin and steers its membrane-penetration activity toward the plasma membrane. Nat. Struct. Mol. Biol. 11, 36–44. https://doi.org/10.1038/nsmb709

Bai, J., Wang, P., Chapman, E.R., 2002. C2A activates a cryptic Ca2+-triggered membrane penetration activity within the C2B domain of synaptotagmin I. Proc. Natl. Acad. Sci. 99, 1665–1670. https://doi.org/10.1073/pnas.032541099

Bajjalieh, S.M., Peterson, K., Shinghal, R., Scheller, R.H., 1992. SV2, a Brain Synaptic Vesicle Protein Homologous to Bacterial Transporters. Sci. New Ser. 257, 1271–1273.

Baker, K., Gordon, S.L., Grozeva, D., van Kogelenberg, M., Roberts, N.Y., Pike, M., Blair, E., Hurles, M.E., Chong, W.K., Baldeweg, T., Kurian, M.A., Boyd, S.G., Cousin, M.A., Raymond, F.L., 2015. Identification of a human synaptotagmin-1 mutation that perturbs synaptic vesicle cycling. J. Clin. Invest. JCI79765. https://doi.org/10.1172/JCI79765

Baker, K., Gordon, S.L., Melland, H., Bumbak, F., Scott, D.J., Jiang, T.J., Owen, D., Turner, B.J., Boyd, S.G., Rossi, M., Al-Raqad, M., Elpeleg, O., Peck, D., Mancini, G.M.S., Wilke, M., Zollino, M., Marangi, G., Weigand, H., Borggraefe, I., Haack, T., Stark, Z., Sadedin, S., Broad Center for Mendelian Genomics, Tan, T.Y., Jiang, Y., Gibbs, R.A., Ellingwood, S., Amaral, M., Kelley, W., Kurian, M.A., Cousin, M.A., Raymond, F.L., 2018. SYT1-associated neurodevelopmental disorder: a case series. Brain. https://doi.org/10.1093/brain/awy209

Bers, D.M., Patton, C.W., Nuccitelli, R., 2010. A Practical Guide to the Preparation of Ca2+ Buffers, in: Methods in Cell Biology. Elsevier, pp. 1–26. https://doi.org/10.1016/B978-0-12-374841-6.00001-3

Bever, C.T., Young, D., Anderson, P.A., Krumholz, A., Conway, K., Leslie, J., Eddington, N., Plaisance, K.I., Panitch, H.S., Dhib-Jalbut, S., Fossler, M.J., Devane, J., Johnson, K.P., 1994. The effects of 4-aminopyridine in multiple sclerosis patients: Results of a randomized, placebo-controlled, double-blind, concentration-controlled, crossover trial. Neurology 44, 1054–1054. https://doi.org/10.1212/WNL.44.6.1054

Bhalla, A., Chicka, M.C., Chapman, E.R., 2008. Analysis of the synaptotagmin family during reconstituted membrane fusion: Uncovering a class of inhibitory isoforms. J. Biol. Chem. 283, 21799–21807. https://doi.org/10.1074/jbc.M709628200

Bhalla, A., Chicka, M.C., Tucker, W.C., Chapman, E.R., 2006. Ca2+–synaptotagmin directly regulates t-SNARE function during reconstituted membrane fusion. Nat. Struct. Mol. Biol. 13, 323–330. https://doi.org/10.1038/nsmb1076

Bodzęta, A., Kahms, M., Klingauf, J., 2017. The Presynaptic v-ATPase Reversibly Disassembles and Thereby Modulates Exocytosis but Is Not Part of the Fusion Machinery. Cell Rep. 20, 1348–1359. https://doi.org/10.1016/j.celrep.2017.07.040

Boll, I., Jensen, P., Schwämmle, V., Larsen, M.R., 2020. Depolarization-dependent Induction of Site-specific Changes in Sialylation on N-linked Glycoproteins in Rat Nerve Terminals. Mol. Cell. Proteomics 19, 1418–1435. https://doi.org/10.1074/mcp.RA119.001896

Bosmann, H.B., 1973. SYNTHESIS OF GLYCOPROTEINS IN BRAIN: IDENTIFICATION, PURIFICATION AND PROPERTIES OF A SYNAPTOSOMAL SIALYL TRANSFERASE UTILIZING ENDOGENOUS AND EXOGENOUS ACCEPTORS. J. Neurochem. 20, 1037–1049. https://doi.org/10.1111/j.1471-4159.1973.tb00075.x

Bosmann, H.B., 1972. SYNTHESIS OF GLYCOPROTEINS IN BRAIN: IDENTIFICATION, PURIFICATION AND PROPERTIES OF GLYCOSYL TRANSFERASES FROM PURIFIED SYNAPTOSOMES OF GUINEA PIG CEREBRAL CORTEX. J. Neurochem. 19, 763–778. https://doi.org/10.1111/j.1471-4159.1972.tb01391.x

Bradberry, M.M., Bao, H., Lou, X., Chapman, E.R., 2019. Phosphatidylinositol 4,5-bisphosphate drives $Ca^{2+}$ -independent membrane penetration by the tandem C2 domain proteins synaptotagmin-1 and Doc2β. J. Biol. Chem. 294, 10942–10953. https://doi.org/10.1074/jbc.RA119.007929

Bradberry, M.M., Courtney, N.A., Dominguez, M.J., Lofquist, S.M., Knox, A.T., Sutton, R.B., Chapman, E.R., 2020. Molecular Basis for Synaptotagmin-1-Associated Neurodevelopmental Disorder. Neuron 107, 52-64.e7. https://doi.org/10.1016/j.neuron.2020.04.003

Brose, N., Brunger, A., Cafiso, D., Chapman, E.R., Diao, J., Hughson, F.M., Jackson, M.B., Jahn, R., Lindau, M., Ma, C., Rizo, J., Shin, Y.-K., Söllner, T.H., Tamm, L., Yoon, T.-Y., Zhang, Y., 2019. Synaptic vesicle fusion: today and beyond. Nat. Struct. Mol. Biol. 26, 663–668. https://doi.org/10.1038/s41594-019-0277-z

Brose, N., Petrenko, A.G., Sudhof, T.C., Jahn, R., 1992a. Synaptotagmin : A Calcium Sensor on the Synaptic Vesicle Surface. Science 256, 1021–1025.

Brose, N., Petrenko, A.G., Südhof, T.C., Jahn, R., 1992b. Synaptotagmin: A Calcium Sensor on the Synaptic Vesicle Surface. Sci. New Ser. 256, 1021–1025.

Buckley, K., Kelly, R.B., 1985. Identification of a transmembrane glycoprotein specific for secretory vesicles of neural and endocrine cells. J. Cell Biol. 100, 1284–1294. https://doi.org/10.1083/jcb.100.4.1284

Burgalossi, A., Jung, S., Meyer, G., Jockusch, W.J., Jahn, O., Taschenberger, H., O'Connor, V.M., Nishiki, T., Takahashi, M., Brose, N., Rhee, J.-S., 2010. SNARE Protein Recycling by αSNAP and βSNAP Supports Synaptic Vesicle Priming. Neuron 68, 473–487. https://doi.org/10.1016/j.neuron.2010.09.019

Burger, P.M., Hell, J., Mehl, E., Krasel, C., Lottspeich, F., Jahn, R., 1991. GABA and glycine in synaptic vesicles: storage and transport characteristics. Neuron 7, 287–293.

Burger, P.M., Mehl, E., Cameron, P.L., Maycox, P.R., Baumert, M., Lottspeich, F., De Camilli, P., Jahn, R., 1989. Synaptic vesicles immunoisolated from rat cerebral cortex contain high levels of glutamate. Neuron 3, 715–720. https://doi.org/10.1016/0896-6273(89)90240-7

Chang, S., Trimbuch, T., Rosenmund, C., 2018. Synaptotagmin-1 drives synchronous Ca2+-triggered fusion by C2B-domain-mediated synaptic-vesicle-membrane attachment. Nat. Neurosci. 21, 33–40. https://doi.org/10.1038/s41593-017-0037-5

Chang, W.-P., Sudhof, T.C., 2009. SV2 Renders Primed Synaptic Vesicles Competent for Ca2+-Induced Exocytosis. J. Neurosci. 29, 883–897. https://doi.org/10.1523/JNEUROSCI.4521-08.2009

Chantranupong, L., Saulnier, J.L., Wang, W., Jones, D.R., Pacold, M.E., Sabatini, B.L., 2020. Rapid purification and metabolomic profiling of synaptic vesicles from mammalian brain. eLife 9, e59699. https://doi.org/10.7554/eLife.59699

Chapman, Edwin R, 2008. How does synaptotagmin trigger neurotransmitter release? Annu. Rev. Biochem. 77, 615–641. https://doi.org/10.1146/annurev.biochem.77.062005.101135

Chapman, Edwin R., 2008. How Does Synaptotagmin Trigger Neurotransmitter Release? Annu. Rev. Biochem. 77, 615–641. https://doi.org/10.1146/annurev.biochem.77.062005.101135

Chapman, E.R., Davis, A.F., 1998. Direct Interaction of a Ca2+-binding Loop of Synaptotagmin with Lipid Bilayers. J. Biol. Chem. 273, 13995–14001. https://doi.org/10.1074/jbc.273.22.13995

Chen, W.W., Freinkman, E., Wang, T., Birsoy, K., Sabatini, D.M., 2016. Absolute Quantification of Matrix Metabolites Reveals the Dynamics of Mitochondrial Metabolism. Cell 166, 1324-1337.e11. https://doi.org/10.1016/j.cell.2016.07.040

Cotman, C., Blank, M.L., Moehl, A., Snyder, F., 1969. Lipid Composition of Synaptic Plasma Membranes Isolated from Rat Brain by Zonal Centrifugation. Biochemistry 8, 4606–4612. https://doi.org/10.1021/bi00839a056

Courtney, N.A., Bao, H., Briguglio, J.S., Chapman, E.R., 2019. Synaptotagmin 1 clamps synaptic vesicle fusion in mammalian neurons independent of complexin. Nat. Commun. 10, 4076. https://doi.org/10.1038/s41467-019-12015-w

Courtney, N.A., Briguglio, J.S., Bradberry, M.M., Greer, C., Chapman, E.R., 2018a. Excitatory and Inhibitory Neurons Utilize Different Ca2+Sensors and Sources to Regulate Spontaneous Release. Neuron 98, 977–991. https://doi.org/10.1016/j.neuron.2018.04.022

Courtney, N.A., Briguglio, J.S., Bradberry, M.M., Greer, C., Chapman, E.R., 2018b. Excitatory and Inhibitory Neurons Utilize Different Ca2+ Sensors and Sources to Regulate Spontaneous Release. Neuron 98, 977-991.e5. https://doi.org/10.1016/j.neuron.2018.04.022

Crowder, K.M., Gunther, J.M., Jones, T.A., Hale, B.D., Zhang, H.Z., Peterson, M.R., Scheller, R.H., Chavkin, C., Bajjalieh, S.M., 1999. Abnormal neurotransmission in mice lacking synaptic vesicle protein 2A (SV2A). Proc. Natl. Acad. Sci. 96, 15268–15273. https://doi.org/10.1073/pnas.96.26.15268

Custer, K.L., 2006. Synaptic Vesicle Protein 2 Enhances Release Probability at Quiescent Synapses. J. Neurosci. 26, 1303–1313. https://doi.org/10.1523/JNEUROSCI.2699-05.2006

Dana, H., Mohar, B., Sun, Y., Narayan, S., Gordus, A., Hasseman, J.P., Tsegaye, G., Holt, G.T., Hu, A., Walpita, D., Patel, R., Macklin, J.J., Bargmann, C.I., Ahrens, M.B., Schreiter, E.R., Jayaraman, V., Looger, L.L., Svoboda, K., Kim, D.S., 2016. Sensitive red protein calcium indicators for imaging neural activity. eLife 5.

de Juan-Sanz, J., Holt, G.T., Schreiter, E.R., de Juan, F., Kim, D.S., Ryan, T.A., 2017. Axonal Endoplasmic Reticulum Ca2+ Content Controls Release Probability in CNS Nerve Terminals. Neuron 93, 867-881.e6. https://doi.org/10.1016/j.neuron.2017.01.010

Denisov, I.G., Grinkova, Y. V., Lazarides, A.A., Sligar, S.G., 2004. Directed Self-Assembly of Monodisperse Phospholipid Bilayer Nanodiscs with Controlled Size. J. Am. Chem. Soc. 126, 3477–3487. https://doi.org/10.1021/ja0393574

Deo, C., Sheu, S.-H., Seo, J., Clapham, D.E., Lavis, L.D., 2019. Isomeric Tuning Yields Bright and Targetable Red $Ca^{2+}$ Indicators. J. Am. Chem. Soc. 141, 13734–13738. https://doi.org/10.1021/jacs.9b06092

Di Paolo, G., Moskowitz, H.S., Gipson, K., Wenk, M.R., Voronov, S., Obayashi, M., Flavell, R., Fitzsimonds, R.M., Ryan, T. a, De Camilli, P., 2004. Impaired PtdIns(4,5)P2 synthesis in nerve

terminals produces defects in synaptic vesicle trafficking. Nature 431, 415–422. https://doi.org/10.1038/nature02896

Dodge, F.A., Rahamimoff, R., 1967. Co-operative action of calcium ions in transmitter release at the neuromuscular junction. J. Physiol. 193, 419–432. https://doi.org/10.1113/jphysiol.1967.sp008367

Douglas, W.W., Poisner, A.M., 1966. Evidence that the secreting adrenal chromaffin cell releases catecholamines directly from ATP-rich granules. J. Physiol. 183, 236–248. https://doi.org/10.1113/jphysiol.1966.sp007863

Eberhard, D.A., Cooper, C.L., Low, M.G., Holz, R.W., 1990a. Evidence that the inositol phospholipids are necessary for exocytosis. Biochem. J. 268, 15–25. https://doi.org/10.1042/bj2680015

Eberhard, D.A., Cooper, C.L., Low, M.G., Holz, R.W., 1990b. Evidence that the inositol phospholipids are necessary for exocytosis. Loss of inositol phospholipids and inhibition of secretion in permeabilized cells caused by a bacterial phospholipase C and removal of ATP. Biochem. J. 268, 15–25. https://doi.org/10.1042/bj2680015

Edelstein, A., Amodaj, N., Hoover, K., Vale, R., Stuurman, N., 2010. Computer Control of Microscopes Using μManager, in: Ausubel, F.M., Brent, R., Kingston, R.E., Moore, D.D., Seidman, J.G., Smith, J.A., Struhl, K. (Eds.), Current Protocols in Molecular Biology. John Wiley & Sons, Inc., Hoboken, NJ, USA, p. mb1420s92. https://doi.org/10.1002/0471142727.mb1420s92

Eriksen, J., Chang, R., McGregor, M., Silm, K., Suzuki, T., Edwards, R.H., 2016. Protons Regulate Vesicular Glutamate Transporters through an Allosteric Mechanism. Neuron 90, 768–780. https://doi.org/10.1016/j.neuron.2016.03.026

Estévez-Herrera, J., Domínguez, N., Pardo, M.R., González-Santana, A., Westhead, E.W., Borges, R., Machado, J.D., 2016. ATP: The crucial component of secretory vesicles. Proc. Natl. Acad. Sci. 113, E4098–E4106. https://doi.org/10.1073/pnas.1600690113

Evans, C.S., He, Z., Bai, H., Lou, X., Jeggle, P., Sutton, R.B., Edwardson, J.M., Chapman, E.R., 2016. Functional analysis of the interface between the tandem C2 domains of synaptotagmin-1. Mol. Biol. Cell 27, 979–989. https://doi.org/10.1091/mbc.E15-07-0503

Evans, C.S., Ruhl, D. a., Chapman, E.R., 2015a. An Engineered Metal Sensor Tunes the Kinetics of Synaptic Transmission. J. Neurosci. 35, 11769–11779. https://doi.org/10.1523/JNEUROSCI.1694-15.2015

Evans, C.S., Ruhl, D.A., Chapman, E.R., 2015b. An Engineered Metal Sensor Tunes the Kinetics of Synaptic Transmission. J. Neurosci. 35, 11769–11779. https://doi.org/10.1523/JNEUROSCI.1694-15.2015

Evans, P., 2006. Scaling and assessment of data quality. Acta Crystallogr. D Biol. Crystallogr. 62, 72–82. https://doi.org/10.1107/S0907444905036693

Feany, M.B., Lee, S., Edwards, R.H., Buckley, K.M., 1992. The synaptic vesicle protein SV2 is a novel type of transmembrane transporter. Cell 70, 861–867. https://doi.org/10.1016/0092-8674(92)90319-8

Fernandez, I., Araç, D., Ubach, J., Gerber, S.H., Shin, O.-H., Gao, Y., Anderson, R.G., Südhof, T.C., Rizo, J., 2001. Three-dimensional structure of the synaptotagmin 1 C2B-domain: synaptotagmin 1 as a phospholipid binding machine. Neuron 32, 1057–1069.

Fernández-Alfonso, T., Kwan, R., Ryan, T.A., 2006. Synaptic Vesicles Interchange Their Membrane Proteins with a Large Surface Reservoir during Recycling. Neuron 51, 179–186. https://doi.org/10.1016/j.neuron.2006.06.008

Gaffaney, J.D., Dunning, F.M., Wang, Z., Hui, E., Chapman, E.R., 2008. Synaptotagmin C2B Domain Regulates $Ca^{2+}$-triggered Fusion *in Vitro*: CRITICAL RESIDUES REVEALED BY SCANNING ALANINE MUTAGENESIS. J. Biol. Chem. 283, 31763–31775. https://doi.org/10.1074/jbc.M803355200

García-Pérez, E., Mahfooz, K., Covita, J., Zandueta, A., Wesseling, J.F., 2015. Levetiracetam accelerates the onset of supply rate depression in synaptic vesicle trafficking. Epilepsia 56, 535–545. https://doi.org/10.1111/epi.12930

Geppert, M., Goda, Y., Hammer, R.E., Li, C., Rosahl, T.W., Stevens, C.F., Südhof, T.C., 1994. Synaptotagmin I: A major Ca2+ sensor for transmitter release at a central synapse. Cell 79, 717–727. https://doi.org/10.1016/0092-8674(94)90556-8

Giladi, M., Michaeli, L., Almagor, L., Bar-On, D., Buki, T., Ashery, U., Khananshvili, D., Hirsch, J.A., 2013. The C2B domain is the primary Ca2 + sensor in DOC2B: A structural and functional analysis. J. Mol. Biol. 425, 4629–4641. https://doi.org/10.1016/j.jmb.2013.08.017

Goodrum, J.F., Bosmann, H.B., Tanaka, R., 1979. Glycoprotein galactosyltransferase activity in synaptic junctional complexes isolated from rat forebrain. Neurochem. Res. 4, 331–337. https://doi.org/10.1007/BF00963803

Grishanin, R.N., Kowalchyk, J.A., Klenchin, V.A., Ann, K., Earles, C.A., Chapman, E.R., Gerona, R.R.L., Martin, T.F.J., 2004. CAPS acts at a prefusion step in dense-core vesicle exocytosis as a PIP2 binding protein. Neuron 43, 551–562. https://doi.org/10.1016/j.neuron.2004.07.028

Groffen, A.J., Martens, S., Arazola, R.D., Cornelisse, L.N., Lozovaya, N., de Jong, A.P.H., Goriounova, N.A., Habets, R.L.P., Takai, Y., Borst, J.G., Brose, N., McMahon, H.T., Verhage, M., 2010. Doc2b Is a High-Affinity Ca2+ Sensor for Spontaneous Neurotransmitter Release. Science 327, 1614–1618. https://doi.org/10.1126/science.1183765

Groffen, A.J.A., Friedrich, R., Brian, E.C., Ashery, U., Verhage, M., 2006. DOC2A and DOC2B are sensors for neuronal activity with unique calcium-dependent and kinetic properties. J. Neurochem. 97, 818–833. https://doi.org/10.1111/j.1471-4159.2006.03755.x

Grynkiewicz, G., Poenie, M., Tsien, R.Y., 1985. A new generation of Ca2+ indicators with greatly improved fluorescence properties. J. Biol. Chem. 260, 3440–3450. https://doi.org/3838314

Hay, J.C., Fisette, P.L., Jenkins, G.H., Fukami, K., Takenawa, T., Anderson, R.A., Martin, T.F.J., 1995. ATP-dependent inositide phosphorylation required for Ca2+-activated secretion. Nature. https://doi.org/10.1038/374173a0

Herrick, D.Z., Sterbling, S., Rasch, K.A., Hinderliter, A., Cafiso, D.S., 2006. Position of Synaptotagmin I at the Membrane Interface: Cooperative Interactions of Tandem C2 Domains †. Biochemistry 45, 9668–9674. https://doi.org/10.1021/bi060874j

Hille, B., Billiard, J., Babcock, D.F., Nguyen, T., Koh, D.S., 1999. Stimulation of exocytosis without a calcium signal. J. Physiol. 520, 23–31. https://doi.org/10.1111/j.1469-7793.1999.00023.x

Holmes, S.E., Scheinost, D., Finnema, S.J., Naganawa, M., Davis, M.T., DellaGioia, N., Nabulsi, N., Matuskey, D., Angarita, G.A., Pietrzak, R.H., Duman, R.S., Sanacora, G., Krystal, J.H., Carson, R.E., Esterlis, I., 2019. Lower synaptic density is associated with depression severity and network alterations. Nat. Commun. 10, 1529. https://doi.org/10.1038/s41467-019-09562-7

Hoppa, M.B., Lana, B., Margas, W., Dolphin, A.C., Ryan, T.A., 2012. α2δ expression sets presynaptic calcium channel abundance and release probability. Nature 486, 122–125. https://doi.org/10.1038/nature11033

Houy, S., Groffen, A.J., Ziomkiewicz, I., Verhage, M., Pinheiro, P.S., Sørensen, J.B., 2017. Doc2B acts as a calcium sensor for vesicle priming requiring synaptotagmin-1, munc13-2 and SNAREs. eLife 6, 1–29. https://doi.org/10.7554/eLife.27000

Hove-Madsen, L., Baudet, S., Bers, D.M., 2010. Making and Using Calcium-Selective Mini- and Microelectrodes, in: Methods in Cell Biology. Elsevier, pp. 67–89. https://doi.org/10.1016/B978-0-12-374841-6.00003-7

Hua, Y., Sinha, R., Thiel, C.S., Schmidt, R., Hüve, J., Martens, H., Hell, S.W., Egner, A., Klingauf, J., 2011. A readily retrievable pool of synaptic vesicles. Nat. Neurosci. 14, 833–839. https://doi.org/10.1038/nn.2838

Hui, E., Bai, J., Chapman, E.R., 2006. Ca2+-triggered simultaneous membrane penetration of the tandem C2-domains of synaptotagmin I. Biophys J 91, 1767–1777. https://doi.org/S0006-3495(06)71889-6 [pii]\r10.1529/biophysj.105.080325

Hui, E., Bai, J., Wang, P., Sugimori, M., Llinas, R.R., Chapman, E.R., 2005. Three distinct kinetic groupings of the synaptotagmin family: candidate sensors for rapid and delayed exocytosis. Proc. Natl. Acad. Sci. 102, 5210–4. https://doi.org/10.1073/pnas.0500941102

Hui, E., Gaffaney, J.D., Wang, Z., Johnson, C.P., Evans, C.S., Chapman, E.R., 2011. Mechanism and function of synaptotagmin-mediated membrane apposition. Nat Struct Mol Biol 18, 813–821. https://doi.org/10.1038/nsmb.2075

Hui, E., Johnson, C.P., Yao, J., Dunning, F.M., Chapman, E.R., 2009a. Synaptotagmin-Mediated Bending of the Target Membrane Is a Critical Step in Ca2+-Regulated Fusion. Cell 138, 709–721. https://doi.org/10.1016/j.cell.2009.05.049

Hui, E., Johnson, C.P., Yao, J., Dunning, F.M., Chapman, E.R., 2009b. Synaptotagmin-Mediated Bending of the Target Membrane Is a Critical Step in Ca2+-Regulated Fusion. Cell 138, 709–721. https://doi.org/10.1016/j.cell.2009.05.049

Jahn, R., Schiebler, W., Ouimet, C., Greengard, P., 1985. A 38,000-dalton membrane protein (p38) present in synaptic vesicles. Proc. Natl. Acad. Sci. 82, 4137–4141. https://doi.org/10.1073/pnas.82.12.4137

James, D.J., Khodthong, C., Kowalchyk, J.A., Martin, T.F.J., 2008. Phosphatidylinositol 4,5-bisphosphate regulates SNARE-dependent membrane fusion. J. Cell Biol. 182, 355–366. https://doi.org/10.1083/jcb.200801056

Janz, R., Goda, Y., Geppert, M., Missler, M., Südhof, T.C., 1999. SV2A and SV2B Function as Redundant Ca2+ Regulators in Neurotransmitter Release. Neuron 24, 1003–1016. https://doi.org/10.1016/S0896-6273(00)81046-6

Kabsch, W., 2010. *XDS*. Acta Crystallogr. D Biol. Crystallogr. 66, 125–132. https://doi.org/10.1107/S0907444909047337

Kaminski, R.M., Gillard, M., Leclercq, K., Hanon, E., Lorent, G., Dassesse, D., Matagne, A., Klitgaard, H., 2009. Proepileptic phenotype of SV2A-deficient mice is associated with reduced anticonvulsant efficacy of levetiracetam. Epilepsia 50, 1729–1740. https://doi.org/10.1111/j.1528-1167.2009.02089.x

Kaminski, R.M., Matagne, A., Leclercq, K., Gillard, M., Michel, P., Kenda, B., Talaga, P., Klitgaard, H., 2008. SV2A protein is a broad-spectrum anticonvulsant target: Functional correlation between protein binding and seizure protection in models of both partial and generalized epilepsy. Neuropharmacology 54, 715–720. https://doi.org/10.1016/j.neuropharm.2007.11.021

Kane, P.M., 1995. Disassembly and Reassembly of the Yeast Vacuolar H+-ATPase in Vivo. J. Biol. Chem. 270, 17025–17032. https://doi.org/10.1016/S0021-9258(17)46944-4

Kartal, A., 2017. Can High-Dose Levetiracetam Be Safe? A Case Report of Prolonged Accidental High-Dose Levetiracetam Administration and Review of the Literature. Clin. Neuropharmacol. 40, 217–218. https://doi.org/10.1097/WNF.0000000000000229

Katz, B, Miledi, R., 1967. The Timing of Calcium Action During Neuromuscular Transmission. J. Physiol. 189, 535–544. https://doi.org/10.1113/jphysiol.1967.sp008183

Katz, B., Miledi, R., 1967. The timing of calcium action during neuromuscular transmission. J. Physiol. 189, 535–544. https://doi.org/10.1113/jphysiol.1967.sp008183

Kiessling, V., Kreutzberger, A.J.B., Liang, B., Nyenhuis, S.B., Seelheim, P., Castle, J.D., Cafiso, D.S., Tamm, L.K., 2018. A molecular mechanism for calcium-mediated synaptotagmin-triggered exocytosis. Nat. Struct. Mol. Biol. 25, 911–917. https://doi.org/10.1038/s41594-018-0130-9

Klitgaard, H., Matagne, A., Nicolas, J.-M., Gillard, M., Lamberty, Y., De Ryck, M., Kaminski, R.M., Leclercq, K., Niespodziany, I., Wolff, C., Wood, M., Hannestad, J., Kervyn, S., Kenda, B., 2016. Brivaracetam: Rationale for discovery and preclinical profile of a selective SV2A ligand for epilepsy treatment. Epilepsia 57, 538–548. https://doi.org/10.1111/epi.13340

Klowak, J.A., Hewitt, M., Catenacci, V., Duffett, M., Rochwerg, B., Jones, K., Choong, K., 2021. Levetiracetam Versus Phenytoin or Fosphenytoin for Second-Line Treatment of Pediatric Status Epilepticus: A Meta-Analysis. Pediatr. Crit. Care Med. Publish Ahead of Print. https://doi.org/10.1097/PCC.0000000000002703

Kochubey, O., Schneggenburger, R., 2011a. Synaptotagmin Increases the Dynamic Range of Synapses by Driving Ca2+-Evoked Release and by Clamping a Near-Linear Remaining Ca2+Sensor. Neuron 69, 736–748. https://doi.org/10.1016/j.neuron.2011.01.013

Kochubey, O., Schneggenburger, R., 2011b. Synaptotagmin Increases the Dynamic Range of Synapses by Driving Ca2+-Evoked Release and by Clamping a Near-Linear Remaining Ca2+ Sensor. Neuron 69, 736–748. https://doi.org/10.1016/j.neuron.2011.01.013

Kutner, R.H., Zhang, X.-Y., Reiser, J., 2009. Production, concentration and titration of pseudotyped HIV-1-based lentiviral vectors. Nat. Protoc. 4, 495–505. https://doi.org/10.1038/nprot.2009.22

Kwon, S.E., Chapman, E.R., 2012. Glycosylation Is Dispensable for Sorting of Synaptotagmin 1 but Is Critical for Targeting of SV2 and Synaptophysin to Recycling Synaptic Vesicles. J. Biol. Chem. 287, 35658–35668. https://doi.org/10.1074/jbc.M112.398883

Kyrychenko, A., Ladokhin, A.S., 2013. Molecular dynamics simulations of depth distribution of spin-labeled phospholipids within lipid bilayer. J. Phys. Chem. B 117, 5875–5885. https://doi.org/10.1021/jp4026706

Lalo, U., Palygin, O., Rasooli-Nejad, S., Andrew, J., Haydon, P.G., Pankratov, Y., 2014. Exocytosis of ATP From Astrocytes Modulates Phasic and Tonic Inhibition in the Neocortex. PLoS Biol. 12, e1001747. https://doi.org/10.1371/journal.pbio.1001747

Larsson, M., Sawada, K., Morland, C., Hiasa, M., Ormel, L., Moriyama, Y., Gundersen, V., 2012. Functional and Anatomical Identification of a Vesicular Transporter Mediating Neuronal ATP Release. Cereb. Cortex 22, 1203–1214. https://doi.org/10.1093/cercor/bhr203

Lee, J., Guan, Z., Akbergenova, Y., Littleton, J.T., 2013. Genetic Analysis of Synaptotagmin C2 Domain Specificity in Regulating Spontaneous and Evoked Neurotransmitter Release. J. Neurosci. 33, 187–200. https://doi.org/10.1523/JNEUROSCI.3214-12.2013

Leussink, V.I., Montalban, X., Hartung, H.-P., 2018. Restoring Axonal Function with 4-Aminopyridine: Clinical Efficacy in Multiple Sclerosis and Beyond. CNS Drugs 32, 637–651. https://doi.org/10.1007/s40263-018-0536-2

Levitt, B., Head, R.J., Westfall, D.P., 1984. Detection of Adenosine and Adenine Nucleotides: Application to Endogenous Content and Electrically Induced Release of Adenyl Purines in Guinea Pig Vas Deferens. Anal. Biochem. 137, 93–100.

Li, J., Cantley, J., Burchfield, J.G., Meoli, C.C., Stöckli, J., Whitworth, P.T., Pant, H., Chaudhuri, R., Groffen, A.J.A., Verhage, M., James, D.E., 2014. Doc2 isoforms play dual roles in insulin secretion and insulin-stimulated glucose uptake. Diabetologia 57, 2173–2182. https://doi.org/10.1007/s00125-014-3312-y

Li, L., Shin, O.-H., Rhee, J.-S., Araç, D., Rah, J.-C., Rizo, J., Südhof, T., Rosenmund, C., 2006. Phosphatidylinositol Phosphates as Co-activators of $Ca^{2+}$ Binding to $C_2$ Domains of Synaptotagmin 1. J. Biol. Chem. 281, 15845–15852. https://doi.org/10.1074/jbc.M600888200

Littleton, J.T., Stern, M., Schulze, K., Perin, M., Bellen, H.J., 1993. Mutational analysis of Drosophila synaptotagmin demonstrates its essential role in Ca2+-activated neurotransmitter release. Cell 74, 1125–1134. https://doi.org/10.1016/0092-8674(93)90733-7

Liu, H., Bai, H., Xue, R., Takahashi, H., Edwardson, J.M., Chapman, E.R., 2014. Linker mutations reveal the complexity of synaptotagmin 1 action during synaptic transmission. Nat. Neurosci. 17, 670–677. https://doi.org/10.1038/nn.3681

Liu, H., Dean, C., Arthur, C.P., Dong, M., Chapman, E.R., 2009. Autapses and Networks of Hippocampal Neurons Exhibit Distinct Synaptic Transmission Phenotypes in the Absence of Synaptotagmin I. J. Neurosci. 29, 7395–7403. https://doi.org/10.1523/JNEUROSCI.1341-09.2009

London, E., Chattopadhyay, A., 1987. Parallax Method for Direct Measurement of Membrane Penetration Depth Utilizing Fluorescence Quenching by Spin-Labeled Phospholipids. Biochemistry 26, 39–45. https://doi.org/10.1021/bi00375a006

Los, G.V., Encell, L.P., McDougall, M.G., Hartzell, D.D., Karassina, N., Zimprich, C., Wood, M.G., Learish, R., Ohana, R.F., Urh, M., Simpson, D., Mendez, J., Zimmerman, K., Otto, P., Vidugiris, G., Zhu, J., Darzins, A., Klaubert, D.H., Bulleit, R.F., Wood, K.V., 2008. HaloTag: A Novel Protein Labeling Technology for Cell Imaging and Protein Analysis. ACS Chem. Biol. 3, 373–382. https://doi.org/10.1021/cb800025k

Löscher, W., Gillard, M., Sands, Z.A., Kaminski, R.M., Klitgaard, H., 2016. Synaptic Vesicle Glycoprotein 2A Ligands in the Treatment of Epilepsy and Beyond. CNS Drugs 30, 1055–1077. https://doi.org/10.1007/s40263-016-0384-x

Lynch, B.A., Lambeng, N., Nocka, K., Kensel-Hammes, P., Bajjalieh, S.M., Matagne, A., Fuks, B., 2004. The synaptic vesicle protein SV2A is the binding site for the antiepileptic drug levetiracetam. Proc. Natl. Acad. Sci. 101, 9861–9866. https://doi.org/10.1073/pnas.0308208101

MacKenzie, D., Arendt, A., Hargrave, P., McDowell, J.H., Molday, R.S., 1984. Localization of binding sites for carboxyl terminal specific anti-rhodopsin monoclonal antibodies using synthetic peptides. Biochemistry 23, 6544–6549. https://doi.org/10.1021/bi00321a041

Mackler, J.M., Drummond, J.A., Loewen, C.A., Robinson, I.M., Reist, N.E., 2002. The C2B Ca2+-binding motif of synaptotagmin is required for synaptic transmission in vivo. Nature 418, 340–344. https://doi.org/10.1038/nature00846

Madeo, M., Kovács, A.D., Pearce, D.A., 2014. The Human Synaptic Vesicle Protein, SV2A, Functions as a Galactose Transporter in *Saccharomyces cerevisiae*. J. Biol. Chem. 289, 33066–33071. https://doi.org/10.1074/jbc.C114.584516

Maravall, M., Mainen, Z.F., Sabatini, B.L., Svoboda, K., 2000. Estimating Intracellular Calcium Concentrations and Buffering without Wavelength Ratioing. Biophys. J. 78, 2655–2667. https://doi.org/10.1016/S0006-3495(00)76809-3

Martens, S., Kozlov, M.M., McMahon, H.T., 2007. How Synaptotagmin Promotes Membrane Fusion. Science 316, 1205–1209.

Marvin, J.S., Borghuis, B.G., Tian, L., Cichon, J., Harnett, M.T., Akerboom, J., Gordus, A., Renninger, S.L., Chen, T.-W., Bargmann, C.I., Orger, M.B., Schreiter, E.R., Demb, J.B., Gan, W.-B., Hires, S.A., Looger, L.L., 2013. An optimized fluorescent probe for visualizing glutamate neurotransmission. Nat. Methods 10, 162–170. https://doi.org/10.1038/nmeth.2333

Marvin, J.S., Scholl, B., Wilson, D.E., Podgorski, K., Kazemipour, A., Müller, J.A., Schoch, S., Quiroz, F.J.U., Rebola, N., Bao, H., Little, J.P., Tkachuk, A.N., Cai, E., Hantman, A.W., Wang, S.S.-H., DePiero, V.J., Borghuis, B.G., Chapman, E.R., Dietrich, D., DiGregorio, D.A., Fitzpatrick, D., Looger, L.L., 2018. Stability, affinity, and chromatic variants of the glutamate sensor iGluSnFR. Nat. Methods 15, 936–939. https://doi.org/10.1038/s41592-018-0171-3

Matthew, W.D., Tsavaler, L.T., Reichardt, L.F., 1981. Identification of a synaptic vesicle-specific membrane protein with a wide distribution in neuronal and neurosecretory tissue. J. Cell Biol. 91, 257–269. https://doi.org/10.1083/jcb.91.1.257

McCoy, A.J., Grosse-Kunstleve, R.W., Adams, P.D., Winn, M.D., Storoni, L.C., Read, R.J., 2007. *Phaser* crystallographic software. J. Appl. Crystallogr. 40, 658–674. https://doi.org/10.1107/S0021889807021206

Michaeli, L., Gottfried, I., Bykhovskaia, M., Ashery, U., 2017. Phosphatidylinositol (4, 5)-bisphosphate targets double C2 domain protein B to the plasma membrane. Traffic 18, 825–839. https://doi.org/10.1111/tra.12528

Micheva, K.D., Holz, R.W., Smith, S.J., 2001a. Regulation of presynaptic phosphatidylinositol 4,5-biphosphate by neuronal activity. J. Cell Biol. 154, 355–368. https://doi.org/10.1083/jcb.200102098

Micheva, K.D., Holz, R.W., Smith, S.J., 2001b. Regulation of presynaptic phosphatidylinositol 4,5-biphosphate by neuronal activity. J. Cell Biol. 154, 355–368. https://doi.org/10.1083/jcb.200102098

Molday, R.S., MacKenzie, D., 1983. Monoclonal antibodies to rhodopsin: characterization, cross-reactivity, and application as structural probes. Biochemistry 22, 653–660. https://doi.org/10.1021/bi00272a020

Nagy, A., Baker, R.R., Morris, S.J., Whittaker, V.P., 1976. The preparation and characterization of synaptic vesicles of high purity. Brain Res. 109, 285–309. https://doi.org/10.1016/0006-8993(76)90531-X

Nalefski, E.A., Wisner, M.A., Chen, J.Z., Sprang, S.R., Fukuda, M., Mikoshiba, K., Falke, J.J., 2001. C2 Domains from Different Ca $^{2+}$ Signaling Pathways Display Functional and Mechanistic Diversity $^{\dagger}$. Biochemistry 40, 3089–3100. https://doi.org/10.1021/bi001968a

Neher, E., Sakaba, T., 2008. Multiple Roles of Calcium Ions in the Regulation of Neurotransmitter Release. Neuron 59, 861–872. https://doi.org/10.1016/j.neuron.2008.08.019

Nishiki, T. -i., Augustine, G.J., 2004. Dual Roles of the C2B Domain of Synaptotagmin I in Synchronizing Ca2+-Dependent Neurotransmitter Release. J. Neurosci. 24, 8542–8550. https://doi.org/10.1523/JNEUROSCI.2545-04.2004

Nowack, A., Malarkey, E.B., Yao, J., Bleckert, A., Hill, J., Bajjalieh, S.M., 2011. Levetiracetam Reverses Synaptic Deficits Produced by Overexpression of SV2A. PLoS ONE 6, e29560. https://doi.org/10.1371/journal.pone.0029560

Nowack, A., Yao, J., Custer, K.L., Bajjalieh, S.M., 2010. SV2 regulates neurotransmitter release via multiple mechanisms. Am. J. Physiol.-Cell Physiol. 299, C960–C967. https://doi.org/10.1152/ajpcell.00259.2010

Orita, S., Naito, A., Sakaguchi, G., Maeda, M., Igarashi, H., Sasaki, T., Takai, Y., 1997. Physical and Functional Interactions of Doc2 and Munc13 in Ca2+-dependent Exocytotic Machinery. J. Biol. Chem. 272, 16081–16084. https://doi.org/10.1016/j.ecolmodel.2010.11.030

Orita, S., Sasaki, T., Naito, A., Komuro, R., Ohtsuka, T., Maeda, M., Suzuki, H., Igarashi, H., Takai, Y., 1995. Doc2: a novel brain protein having two repeated C2-like domains. Biochem. Biophys. Res. Commun. 206, 439–48. https://doi.org/10.1006/bbrc.1995.1062

Pankratov, Y., Lalo, U., Verkhratsky, A., North, R.A., 2006. Vesicular release of ATP at central synapses. Pflüg. Arch. - Eur. J. Physiol. 452, 589–597. https://doi.org/10.1007/s00424-006-0061-x

Park, D., Wu, Y., Lee, S.-E., Kim, G., Jeong, S., Milovanovic, D., Camilli, P.D., Chang, S., 2021. Cooperative function of synaptophysin and synapsin in the generation of synaptic vesicle-like clusters in non-neuronal cells. Nat. Commun. 12, 263. https://doi.org/10.1038/s41467-020-20462-z

Park, Y., Seo, J.B., Fraind, A., Pérez-Lara, A., Yavuz, H., Han, K., Jung, S.-R., Kattan, I., Walla, P.J., Choi, M., Cafiso, D.S., Koh, D.-S., Jahn, R., 2015. Synaptotagmin-1 binds to PIP2-containing membrane but not to SNAREs at physiological ionic strength. Nat. Struct. Mol. Biol. 22, 815–823. https://doi.org/10.1038/nsmb.3097

Parmar, H.B., Barry, C., Kai, F., Duncan, R., 2014. Golgi complex–plasma membrane trafficking directed by an autonomous, tribasic Golgi export signal. Mol. Biol. Cell 25, 866–878. https://doi.org/10.1091/mbc.e13-07-0364

Pérez-Lara, Á., Thapa, A., Nyenhuis, S.B., Nyenhuis, D.A., Halder, P., Tietzel, M., Tittmann, K., Cafiso, D.S., Jahn, R., 2016. PtdInsP2 and PtdSer cooperate to trap synaptotagmin-1 to the plasma membrane in the presence of calcium. eLife 5, 1–22. https://doi.org/10.7554/elife.15886

Pinheiro, P.S., de Wit, H., Walter, A.M., Groffen, A.J., Verhage, M., Sorensen, J.B., 2013. Doc2b Synchronizes Secretion from Chromaffin Cells by Stimulating Fast and Inhibiting Sustained Release. J. Neurosci. 33, 16459–16470. https://doi.org/Doi 10.1523/Jneurosci.2656-13.2013

Pougnet, J.-T., Toulme, E., Martinez, A., Choquet, D., Hosy, E., Boué-Grabot, E., 2014. ATP P2X Receptors Downregulate AMPA Receptor Trafficking and Postsynaptic Efficacy in Hippocampal Neurons. Neuron 83, 417–430. https://doi.org/10.1016/j.neuron.2014.06.005

Quadros, R.M., Miura, H., Harms, D.W., Akatsuka, H., Sato, T., Aida, T., Redder, R., Richardson, G.P., Inagaki, Y., Sakai, D., Buckley, S.M., Seshacharyulu, P., Batra, S.K., Behlke, M.A., Zeiner, S.A., Jacobi, A.M., Izu, Y., Thoreson, W.B., Urness, L.D., Mansour, S.L., Ohtsuka, M., Gurumurthy, C.B., 2017. Easi-CRISPR: a robust method for one-step generation of mice carrying conditional and insertion alleles using long ssDNA donors and CRISPR ribonucleoproteins. Genome Biol. 18, 92. https://doi.org/10.1186/s13059-017-1220-4

Rangaraju, V., Calloway, N., Ryan, T.A., 2014. Activity-Driven Local ATP Synthesis Is Required for Synaptic Function. Cell 156, 825–835. https://doi.org/10.1016/j.cell.2013.12.042

Reigada, D., Diez-Perez, I., Gorostiza, P., Verdaguer, A., Gomez de Aranda, I., Pineda, O., Vilarrasa, J., Marsal, J., Blasi, J., Aleu, J., Solsona, C., 2003. Control of neurotransmitter release by an internal gel matrix in synaptic vesicles. Proc. Natl. Acad. Sci. 100, 3485–3490. https://doi.org/10.1073/pnas.0336914100

Reim, K., Mansour, M., Varoqueaux, F., McMahon, H.T., Südhof, T.C., Brose, N., Rosenmund, C., 2001. Complexins Regulate a Late Step in Ca2+-Dependent Neurotransmitter Release. Cell 104, 71–81. https://doi.org/10.1016/S0092-8674(01)00192-1

Reist, N.E., Buchanan, J., Li, J., DiAntonio, A., Buxton, E.M., Schwarz, T.L., 1998. Morphologically Docked Synaptic Vesicles Are Reduced in *synaptotagmin* Mutants of *Drosophila*. J. Neurosci. 18, 7662–7673. https://doi.org/10.1523/JNEUROSCI.18-19-07662.1998

Ren, J., Bian, X., DeVries, M., Schnegelsberg, B., Cockayne, D.A., Ford, A.P.D.W., Galligan, J.J., 2003. P2X $_2$ subunits contribute to fast synaptic excitation in myenteric neurons of the mouse small intestine. J. Physiol. 552, 809–821. https://doi.org/10.1113/jphysiol.2003.047944

Renganathan, M., Sidach, S., Blight, A.R., 2009. Effects of 4-Aminopyridine on Cloned hERG Channels Expressed in Mammalian Cells. Arch. Drug Inf. 2, 51–57. https://doi.org/10.1111/j.1753-5174.2009.00021.x

Rizalar, F.S., Roosen, D.A., Haucke, V., 2021. A Presynaptic Perspective on Transport and Assembly Mechanisms for Synapse Formation. Neuron 109, 27–41. https://doi.org/10.1016/j.neuron.2020.09.038

Robertson, S.J., Edwards, F.A., 1998. ATP and glutamate are released from separate neurones in the rat medial habenula nucleus: frequency dependence and adenosine-mediated inhibition of release. J. Physiol. 508, 691–701. https://doi.org/10.1111/j.1469-7793.1998.691bp.x

Sabatini, B.L., Regehr, W.G., 1998. Optical Measurement of Presynaptic Calcium Currents. Biophys. J. 74, 1549–1563. https://doi.org/10.1016/S0006-3495(98)77867-1

Sawada, K., Echigo, N., Juge, N., Miyaji, T., Otsuka, M., Omote, H., Yamamoto, A., Moriyama, Y., 2008. Identification of a vesicular nucleotide transporter. Proc. Natl. Acad. Sci. 105, 5683–5686. https://doi.org/10.1073/pnas.0800141105

Schivell, A.E., Batchelor, R.H., Bajjalieh, S.M., 1996. Isoform-specific, Calcium-regulated Interaction of the Synaptic Vesicle Proteins SV2 and Synaptotagmin. J. Biol. Chem. 271, 27770–27775. https://doi.org/10.1074/jbc.271.44.27770

Shao, X., Davletov, B.A., Sutton, R.B., S dhof, T.C., Rizo, J., 1996. Bipartite Ca2+-Binding Motif in C2 Domains of Synaptotagmin and Protein Kinase C. Science 273, 248–251. https://doi.org/10.1126/science.273.5272.248

Shao, X., Fernandez, I., Südhof, T.C., Rizo, J., 1998. Solution Structures of the Ca $^{2+}$ -free and Ca $^{2+}$ -bound C $_2$ A Domain of Synaptotagmin I: Does Ca $^{2+}$ Induce a Conformational Change? $^{\dagger}$. Biochemistry 37, 16106–16115. https://doi.org/10.1021/bi981789h

Shin, O.-H., Xu, J., Rizo, J., Sudhof, T.C., 2009. Differential but convergent functions of Ca2+ binding to synaptotagmin-1 C2 domains mediate neurotransmitter release. Proc. Natl. Acad. Sci. 106, 16469–16474. https://doi.org/10.1073/pnas.0908798106

Stevens, C.F., Sullivan, J.M., 2003. The Synaptotagmin C2A Domain Is Part of the Calcium Sensor Controlling Fast Synaptic Transmission. Neuron 39, 299–308. https://doi.org/10.1016/S0896-6273(03)00432-X

Stockklausner, C., Ludwig, J., Ruppersberg, J.P., Klöcker, N., 2001. A sequence motif responsible for ER export and surface expression of Kir2.0 inward rectifier K $^+$ channels. FEBS Lett. 493, 129–133. https://doi.org/10.1016/S0014-5793(01)02286-4

Sudhof, T.C., Rothman, J.E., 2009. Membrane Fusion: Grappling with SNARE and SM Proteins. Science 323, 474–477. https://doi.org/10.1126/science.1161748

Sutton, R.B., Davletov, B.A., Berghuis, A.M., Sudhof, T.C., Sprang, S.R., 1995. Structure of the first C2 domain of synaptotagmin I: A novel Ca2+/phospholipid-binding fold. Cell 80, 929–938. https://doi.org/10.1016/0092-8674(95)90296-1

Takamori, S., Holt, M., Stenius, K., Lemke, E.A., Grønborg, M., Riedel, D., Urlaub, H., Schenck, S., Brügger, B., Ringler, P., Müller, S.A., Rammner, B., Gräter, F., Hub, J.S., De Groot, B.L., Mieskes, G., Moriyama, Y., Klingauf, J., Grubmüller, H., Heuser, J., Wieland, F., Jahn, R., 2006. Molecular Anatomy of a Trafficking Organelle. Cell 127, 831–846. https://doi.org/10.1016/j.cell.2006.10.030

Takamori, S., Rhee, J.S., Rosenmund, C., Jahn, R., 2000a. Identification of a vesicular glutamate transporter that de®nes a glutamatergic phenotype in neurons 407, 6.

Takamori, S., Riedel, D., Jahn, R., 2000b. Immunoisolation of GABA-Specific Synaptic Vesicles Defines a Functionally Distinct Subset of Synaptic Vesicles. J. Neurosci. 20, 4904–4911. https://doi.org/10.1523/JNEUROSCI.20-13-04904.2000

Taoufiq, Z., Ninov, M., Villar-Briones, A., Wang, H.-Y., Sasaki, T., Roy, M.C., Beauchain, F., Mori, Y., Yoshida, T., Takamori, S., Jahn, R., Takahashi, T., 2020. Hidden proteome of synaptic vesicles in the mammalian brain. Proc. Natl. Acad. Sci. 117, 33586–33596. https://doi.org/10.1073/pnas.2011870117

Tran, H.T., Anderson, L.H., Knight, J.D., 2019. Membrane-Binding Cooperativity and Coinsertion by C2AB Tandem Domains of Synaptotagmins 1 and 7. Biophys. J. 116, 1025–1036. https://doi.org/10.1016/j.bpj.2019.01.035

Tucker, W.C., 2004. Reconstitution of Ca2+-Regulated Membrane Fusion by Synaptotagmin and SNAREs. Science 304, 435–438. https://doi.org/10.1126/science.1097196

Tucker, W.C., Edwardson, J.M., Bai, J., Kim, H.J., Martin, T.F.J., Chapman, E.R., 2003. Identification of synaptotagmin effectors via acute inhibition of secretion from cracked PC12 cells. J. Cell Biol. 162, 199–209. https://doi.org/10.1083/jcb.200302060

Tucker, W.C., Weber, T., Chapman, E.R., 2004. Reconstitution of Ca2+-regulated membrane fusion by synaptotagmin and SNAREs. Science 304, 435–438. https://doi.org/10.1126/science.1097196\r1097196 [pii]

Van den Bogaart, G., Meyenberg, K., Diederichsen, U., Jahn, R., 2012. Phosphatidylinositol 4,5-bisphosphate increases Ca2+ affinity of synaptotagmin-1 by 40-fold. J. Biol. Chem. 287, 16447–16453. https://doi.org/10.1074/jbc.M112.343418

van den Bogaart, G., Meyenberg, K., Diederichsen, U., Jahn, R., 2012. Phosphatidylinositol 4,5-Bisphosphate Increases $Ca^{2+}$ Affinity of Synaptotagmin-1 by 40-fold. J. Biol. Chem. 287, 16447–16453. https://doi.org/10.1074/jbc.M112.343418

van den Bogaart, G., Meyenberg, K., Risselada, H.J., Amin, H., Willig, K.I., Hubrich, B.E., Dier, M., Hell, S.W., Grubmüller, H., Diederichsen, U., Jahn, R., 2011. Membrane protein sequestering by ionic protein–lipid interactions. Nature 479, 552–555. https://doi.org/10.1038/nature10545

Vyleta, N.P., Smith, S.M., 2011. Spontaneous Glutamate Release Is Independent of Calcium Influx and Tonically Activated by the Calcium-Sensing Receptor. J. Neurosci. 31, 4593–4606. https://doi.org/10.1523/JNEUROSCI.6398-10.2011

Walter, A.M., Müller, R., Tawfik, B., Wierda, K.D.B., Pinheiro, P.S., Nadler, A., McCarthy, A.W., Ziomkiewicz, I., Kruse, M., Reither, G., Rettig, J., Lehmann, M., Haucke, V., Hille, B., Schultz, C., Sørensen, J.B., 2017. PIP2 optical uncaging potentiates exocytosis. eLife 6, e30203. https://doi.org/10.7554/eLife.30203

Wan, Q.-F., Zhou, Z.-Y., Thakur, P., Vila, A., Sherry, D.M., Janz, R., Heidelberger, R., 2010. SV2 Acts via Presynaptic Calcium to Regulate Neurotransmitter Release. Neuron 66, 884–895. https://doi.org/10.1016/j.neuron.2010.05.010

Wang, P., Chicka, M.C., Bhalla, A., Richards, D.A., Chapman, E.R., 2005. Synaptotagmin VII Is Targeted to Secretory Organelles in PC12 Cells, Where It Functions as a High-Affinity Calcium Sensor. Mol. Cell. Biol. 25, 8693–8702. https://doi.org/10.1128/MCB.25.19.8693-8702.2005

Wang, Z., Liu, H., Gu, Y., Chapman, E.R., 2011a. Reconstituted synaptotagmin I mediates vesicle docking, priming, and fusion. J. Cell Biol. 195, 1159–1170. https://doi.org/10.1083/jcb.201104079

Wang, Z., Liu, H., Gu, Y., Chapman, E.R., 2011b. Reconstituted synaptotagmin I mediates vesicle docking, priming, and fusion. J. Cell Biol. 195, 1159–1170. https://doi.org/10.1083/jcb.201104079

Weber, T., Zemelman, B.V., McNew, J.A., Westermann, B., Gmachl, M., Parlati, F., Söllner, T.H., Rothman, J.E., 1998. SNAREpins: Minimal Machinery for Membrane Fusion. Cell 92, 759–772. https://doi.org/10.1016/S0092-8674(00)81404-X

Wenk, M.R., Lucast, L., Di Paolo, G., Romanelli, A.J., Suchy, S.F., Nussbaum, R.L., Cline, G.W., Shulman, G.I., McMurray, W., De Camilli, P., 2003. Phosphoinositide profiling in complex lipid mixtures using electrospray ionization mass spectrometry. Nat Biotechnol 21, 813–817. https://doi.org/10.1038/nbt837

Whittaker, V., Michaelson, I., Kirkland, R., 1964. The separation of synaptic vesicles from nerve-ending particles ('synaptosomes'). Biochem. J. 90, 293–303. https://doi.org/10.1042/bj0900293

Wibowo, A., Peters, E.C., Hsieh-Wilson, L.C., 2014. Photoactivatable Glycopolymers for the Proteome-Wide Identification of Fucose-α(1-2)-Galactose Binding Proteins. J. Am. Chem. Soc. 136, 9528–9531. https://doi.org/10.1021/ja502482a

Winn, M.D., Ballard, C.C., Cowtan, K.D., Dodson, E.J., Emsley, P., Evans, P.R., Keegan, R.M., Krissinel, E.B., Leslie, A.G.W., McCoy, A., McNicholas, S.J., Murshudov, G.N., Pannu, N.S., Potterton, E.A., Powell, H.R., Read, R.J., Vagin, A., Wilson, K.S., 2011. Overview of the *CCP* 4 suite and current developments. Acta Crystallogr. D Biol. Crystallogr. 67, 235–242. https://doi.org/10.1107/S0907444910045749

Winter, G., 2010. *xia2* : an expert system for macromolecular crystallography data reduction. J. Appl. Crystallogr. 43, 186–190. https://doi.org/10.1107/S0021889809045701

Winter, G., Waterman, D.G., Parkhurst, J.M., Brewster, A.S., Gildea, R.J., Gerstel, M., Fuentes-Montero, L., Vollmar, M., Michels-Clark, T., Young, I.D., Sauter, N.K., Evans, G., 2018. *DIALS* : implementation and evaluation of a new integration package. Acta Crystallogr. Sect. Struct. Biol. 74, 85–97. https://doi.org/10.1107/S2059798317017235

Wong, J.P., Reboul, E., Molday, R.S., Kast, J., 2009. A Carboxy-Terminal Affinity Tag for the Purification and Mass Spectrometric Characterization of Integral Membrane Proteins. J. Proteome Res. 8, 2388–2396. https://doi.org/10.1021/pr801008c

Wu, D., Bacaj, T., Morishita, W., Goswami, D., Arendt, K.L., Xu, W., Chen, L., Malenka, R.C., Südhof, T.C., 2017. Postsynaptic synaptotagmins mediate AMPA receptor exocytosis during LTP. Nature 544, 316–321. https://doi.org/10.1038/nature21720

Xue, R., Ruhl, D.A., Briguglio, J.S., Figueroa, A.G., Pearce, R.A., Chapman, E.R., 2018. Doc2-mediated superpriming supports synaptic augmentation. Proc. Natl. Acad. Sci. 115, E5605–E5613. https://doi.org/10.1073/pnas.1802104115

Yan, N., 2015. Structural Biology of the Major Facilitator Superfamily Transporters. Annu. Rev. Biophys. 44, 257–283. https://doi.org/10.1146/annurev-biophys-060414-033901

Yang, X., Bognar, J., He, T., Mohammed, M., Niespodziany, I., Wolff, C., Esguerra, M., Rothman, S.M., Dubinsky, J.M., 2015. Brivaracetam augments short-term depression and slows vesicle recycling. Epilepsia 56, 1899–1909. https://doi.org/10.1111/epi.13223

Yao, J., Bajjalieh, S.M., 2008. Synaptic Vesicle Protein 2 Binds Adenine Nucleotides. J. Biol. Chem. 283, 20628–20634. https://doi.org/10.1074/jbc.M800738200

Yao, J., Gaffaney, J.D., Kwon, S.E., Chapman, E.R., 2011. Doc2 is a Ca2+ sensor required for asynchronous neurotransmitter release. Cell 147, 666–677. https://doi.org/10.1016/j.cell.2011.09.046

Yao, J., Nowack, A., Kensel-Hammes, P., Gardner, R.G., Bajjalieh, S.M., 2010. Cotrafficking of SV2 and Synaptotagmin at the Synapse. J. Neurosci. 30, 5569–5578. https://doi.org/10.1523/JNEUROSCI.4781-09.2010

Zhang, N., Gordon, S.L., Fritsch, M.J., Esoof, N., Campbell, D.G., Gourlay, R., Velupillai, S., Macartney, T., Peggie, M., van Aalten, D.M.F., Cousin, M.A., Alessi, D.R., 2015. Phosphorylation of Synaptic Vesicle Protein 2A at Thr84 by Casein Kinase 1 Family Kinases Controls the Specific

Retrieval of Synaptotagmin-1. J. Neurosci. 35, 2492–2507. https://doi.org/10.1523/JNEUROSCI.4248-14.2015

Zhang, Q., Liu, Bin, Wu, Q., Liu, Bing, Li, Y., Sun, S., Wang, Yuan, Wu, X., Chai, Z., Jiang, X., Liu, X., Hu, M., Wang, Yeshi, Yang, Y., Wang, L., Kang, X., Xiong, Y., Zhou, Y., Chen, X., Zheng, L., Zhang, B., Wang, C., Zhu, F., Zhou, Z., 2019. Differential Co-release of Two Neurotransmitters from a Vesicle Fusion Pore in Mammalian Adrenal Chromaffin Cells. Neuron 102, 173-183.e4. https://doi.org/10.1016/j.neuron.2019.01.031

Zhou, Q., Lai, Y., Bacaj, T., Zhao, M., Lyubimov, A.Y., Uervirojnangkoorn, M., Zeldin, O.B., Brewster, A.S., Sauter, N.K., Cohen, A.E., Soltis, S.M., Alonso-Mori, R., Chollet, M., Lemke, H.T., Pfuetzner, R.A., Choi, U.B., Weis, W.I., Diao, J., Südhof, T.C., Brunger, A.T., 2015. Architecture of the synaptotagmin–SNARE machinery for neuronal exocytosis. Nature 525, 62–67. https://doi.org/10.1038/nature14975